

**NANOSCALE THERMAL PROCESSING USING A HEATED
ATOMIC FORCE MICROSCOPE TIP**

A Dissertation
Presented to
The Academic Faculty

by

Brent A. Nelson

In Partial Fulfillment
of the Requirements for the Degree
Doctor of Philosophy in the
Woodruff School of Mechanical Engineering

Georgia Institute of Technology
May 2007

Copyright 2007 by Brent A. Nelson

**NANOSCALE THERMAL PROCESSING USING A HEATED
ATOMIC FORCE MICROSCOPE TIP**

Approved by:

Dr. William P. King, Advisor
Woodruff School of Mechanical
Engineering
Georgia Institute of Technology

Dr. Yogendra Joshi
Woodruff School of Mechanical
Engineering
Georgia Institute of Technology

Dr. F. Levent Degertekin
Woodruff School of Mechanical
Engineering
Georgia Institute of Technology

Dr. Alexei Marchenkov
School of Physics
Georgia Institute of Technology

Dr. William J. Koros
School of Chemical and Biomolecular
Engineering
Georgia Institute of Technology

Date Approved: 03/28/2007

To all the people who made me the man I am

ACKNOWLEDGEMENTS

Standing now at the end of what has been a long journey, I am almost overwhelmed at the number of people whom I now gladly have the opportunity to thank.

First, I would like to thank my advisor, Bill King and the rest of my PhD committee. Bill took a bit of a chance on me in taking me on as a student, and I am grateful for the opportunity I have had to learn across broad disciplines, to develop as a scientist and a teacher, and to discover my passions. Bill challenged me to be better and pushed me to utilize my academic gifts and begin to realize my potential. Levent Degertekin was always encouraging, knowledgeable and helpful. Yogendra Joshi provided welcome guidance in helping me to focus on the right questions for my analytical heat transfer model. Alexei Marchenkov was one of the most impressive teachers from whom I have ever had the opportunity to take a class, challenging himself to dig into the material and prepare his lectures as much as he challenged the students to learn. Bill Koros gave me great feedback and kept me focused on the right questions for the applications I developed.

Many other faculty at GeorgiaTech have played a role in this journey as well. Andrei Fedorov has been a constant encouragement for the past several years, both professionally and personally. Sam Graham provided technical and professional advice, often with a friendly smile. Farrokh Mistree provided a sterling example of how to boldly and uncompromisingly live out one's principles and values. Zhoumin Zhang displayed enthusiasm and a thirst for knowledge that was infectious and inspiring. Mostafa Ghiaasiaan gave me tremendous encouragement to pursue teaching. Paul

Sheehan of the Naval Research Lab, and Larry Bottomley of the chemistry department were instrumental in their chemistry help over the years.

The staff at GeorgiaTech has been sensational as well. Terri Keita always had a smile, a laugh, and a word of truth, and interactions with her were always a joy. Glenda Johnson and Trudy Allen were also always helpful and friendly. The Love building custodians were also a blessing. Sarah's warmth was always an encouragement during long sessions in the lab and the daily smile and brief conversations with Liz and Sheila were always a welcome respite from work.

The graduate student community has been simply sensational. The King and Graham research groups have been great – and I am thankful especially for the challenges and encouragement from Jay, Fabian, Marcus, Shubham, Keunhan, Andrew, and Tom Beechem. Other graduate students who deserve a special note of thanks for their laughs, words, and actions inside and outside of the building are Logan Mcleod, David Damm, Kasi David, and Phil Jones. Mark Poggi taught me how to do research and how to be a scientist with his thirst for knowledge and desire to do quality work. Will Hughes is an inspiration on many levels, professional and personal, and I thank him for his friendship and advice over the years. Thanks also to Jonathan Waddell, and the whole Waddell family, for their hospitality and treating me like family when my own family was across the country. Special words of gratitude go to Joe Charest, Harry Rowland, and Tänya Wright, who became like family, sharing laughs, houses, beds, struggles, frustrations, encouragement, cantilever SEMs, lowered bars, and malaises, and I cannot imagine a better group of folks to spend so much time with in our windowless cave of an office.

The same can be said about our honorary office members, Eileen Moss and Mike Schmittziel.

And many more thanks go to those whose friendship and encouragement brought me to grad school and supported me through it. I cannot understate the thankfulness I have for the brotherhood and sisterhood of Jeremy Ware, Seth Kelly, Dave Cameron, Chris Mooney, Ben Fairfield, Dan Carlson, Doug Bunnell, Paul Wickersham, Davis Butler, Ajay Nayak, Christy Norwood, Danny Martyn, Lisa Slavovsky, Kristin Schou, Jessica Lee, and Claire Thomas, whose prayers, teaching, encouragement, humor, and example have sustained me. I would also like to say a special thanks to Andrew Wilhelms, who has a lot to do with who I have become, and from whom I learned and was challenged more than I can express. Thanks to my family, who have in large part made me who I am. I thank my parents for their support and encouragement, and I thank my sister and brothers for their humor and the laughter all our family has shared.

And finally, all praise be to the Father, from whom all blessings flow.

TABLE OF CONTENTS

ACKNOWLEDGEMENTS	iv
LIST OF TABLES	ix
LIST OF FIGURES	x
SUMMARY	xiii
<u>CHAPTER</u>	
1. Introduction	1
1.1 Heated Atomic Force Microscopy	1
1.2 Motivation for Using Silicon Heated AFM Cantilevers	3
1.3 Previous Work and Current Needs	4
1.4 Dissertation Overview	5
1.5 References	7
2. Review of Applications of Heated Atomic Force Microscope Cantilevers	12
2.1 Fabrication of Cantilevers With Integrated Heaters	13
2.2 Thermal Actuation of AFM Cantilevers	15
2.3 Local Heat Flow Measurements	20
2.4 Material Processing	24
2.5 Summary and Conclusions	33
2.6 References	34
3. Temperature Calibration of Heated Silicon Atomic Force Microscope Cantilevers	44
3.1 Introduction	44
3.2 Background	46
3.3 Raman Thermometry Calibration Methodology	48
3.4 Evaluation of Previous Calibration Methodologies	52
3.5 Validity of Calibration Methodology	57
3.6 Conclusions	64
3.7 References	65

4.	Direct Deposition of Continuous Metal Nanostructures by Thermal Dip-Pen Nanolithography	71
	4.1 Introduction	71
	4.2 Experimental Results and Analysis	74
	4.3 Conclusions	79
	4.4 References	79
5.	Measuring Material Softening with Nanoscale Spatial Resolution Using Heated Silicon AFM Probes	83
	5.1 Introduction	83
	5.2 Instrumentation	86
	5.3 Experiment and Results	90
	5.4 Discussion	101
	5.5 Conclusions	105
	5.6 References	105
6.	Modeling and simulation of the interface temperature between a heated silicon cantilever tip and a substrate	110
	6.1 Introduction	111
	6.2 Theory and Analytical Model	114
	6.3 Results and Discussion	125
	6.4 Conclusions	131
	6.5 References	132
7.	Summary and Recommendations	137
	7.1 Summary	137
	7.2 Recommendations and Future Research	138
	7.3 Long-Range Implications	142
	7.4 References	142
	APPENDIX A: Practicalities of Using Heated Silicon Atomic Force Microscope Cantilevers	144
	APPENDIX B: A Method for Calibrating the Spring Constant of Heated Silicon Cantilevers at Elevated Temperatures	152

LIST OF TABLES

Table 2.1. Uses and applications of heated cantilevers	13
Table 3.1 Organic melting standards and their bulk and measured transition temperatures.	55
Table 6.1. Standard values used for non-dimensional parameters, unless otherwise noted.	125

LIST OF FIGURES

Figure 1.1	Principle of AFM operation.	2
Figure 1.2	Scanning electron microscope and infrared microscope images of silicon heated AFM cantilevers.	3
Figure 2.1	AFM images taken at high speed using thermal actuation for vertical control.	17
Figure 2.2	Thermomechanical writing and thermal reading in a thin polymer layer with a heated AFM cantilever tip.	27
Figure 2.3	Thermally-read image of nanometer-scale indentations written into a thin polymer film.	27
Figure 2.4	Photo of the 32 x 32 “Millipede” arrays of heater-cantilevers.	29
Figure 3.1	Typical variation in cantilever resistance as a function of the temperature at the heater end of the cantilever.	47
Figure 3.2	Drift in Raman calculated temperature from Stokes peak width and peak position.	50
Figure 3.3	Raman-measured heater temperature as a function of total power dissipated on a thermal cantilever.	51
Figure 3.4	Comparison between hotplate and Raman temperature calibrations for a heated cantilever.	53
Figure 3.5	The transition temperatures of organic crystals measured by the thermal cantilever.	55
Figure 3.6	Simulated heater temperature for various cantilever powers.	58
Figure 3.7	Raman-measured heater temperature of a thermal cantilever before and after calibrating on a hotplate.	60
Figure 3.8	Left: comparison of thermal cantilever electrical response after various numbers of electrical cycles.	61
Figure 3.9	Measurements of required heating power as a function of cantilever heater temperature with the cantilever in contact with various substrates.	63

Figure 3.10 Simulated heater temperature as a function of resistance with the cantilever in air and in contact with a substrate.	64
Figure 4.1. Schematic of the operation of tDPN.	73
Figure 4.2. Topographical AFM image of a continuous structure deposited with In.	76
Figure 4.3. Auger electron nanoprobe spectra.	77
Figure 4.4. Electrical transport through the nanowire structure.	78
Figure 5.1 Principle of Local Thermal Analysis.	84
Figure 5.2 Thermal circuit for heat flow through the tip of a heated AFM probe.	89
Figure 5.3 Inverted topography and measured depth of indentations made with a heated probe.	91
Figure 5.4 Amplitude of lateral tip motion as a function of probe temperature.	93
Figure 5.5 Experimental setup for performing thermal analysis with Method 3.	94
Figure 5.6 Total and differential dissipated power and differential AC Phase and amplitude of the probe during a temperature ramp on polystyrene.	96
Figure 5.7 ΔR and deflection as a function of probe temperature.	98
Figure 5.8 ΔR_{indent} as a function of indentation temperature.	100
Figure 5.9 Typical tip crater left behind in the PS substrate by a heated silicon probe.	101
Figure 6.1 Thermal circuit for heat flow through the tip of a heated AFM probe.	112
Figure 6.2 Relative conduction thermal resistance of a conical pin as a function of the normalized distance from a flattened apex.	116
Figure 6.3 Thin film-bulk substrate thermal resistance ratio as a function of the film thickness to contact diameter ratio.	124
Figure 6.4 Normalized interface temperature as a function of the ratio between the tip and substrate thermal conductivities for different values of $R_b k_{tip,r} / r$.	126
Figure 6.5 Normalized interface temperature as a function of the ratio between the tip and substrate thermal conductivities for a soft polymer substrate with different values of b/r and for a hard silicon substrate with different values of a/r assuming Hertzian contact.	129

Figure 6.6 Nondimensional interface temperature as a function of the ratio between
the tip and substrate thermal conductivities for different values of $\frac{k_{gap}}{k_{tip,r}}$. 130

Figure 7.1 Overview of future research directions. 139

SUMMARY

This dissertation aims to advance the current state of use of silicon atomic force microscope (AFM) cantilevers with integrated heaters. To this end, the research consists of two primary thrusts - demonstrating new applications for the cantilevers, and advancing the current state of understanding of their thermal and mechanical behavior to enable further applications. Among new applications, two are described. In the first application, the cantilevers are used for nanoscale material deposition, using heat to modulate the delivery of material from the nanoscale tip. In the second application, the cantilever performs thermal analysis with nanoscale spatial resolution, enabling thermal characterization of near surface and composite interphase regions that cannot be measured with bulk analysis techniques. The second thrust of the research seeks to address fundamental questions concerning the precision use of heated cantilevers. Efforts to this end include characterizing the mechanical, electrical, and thermal behavior of the cantilevers, and optimizing calibration methodology. A technique is developed for calibrating the cantilever spring constant while operating at elevated temperature. Finally, an analytical model is developed for the heat flow in the cantilever tip and relevant dimensionless numbers that govern the relative importance of the various components of the thermal environment are identified. The dimensionless numbers permit exploration of the sensitivity of the tip-substrate interface temperature to the environmental conditions.

CHAPTER 1

INTRODUCTION

Many applications have been developed for the atomic force microscope (AFM) that capitalize on its nanoscale spatial resolution and sensitive force detection. The integration of a heater onto a silicon AFM cantilever gives the cantilevers added functionality for modifying and characterizing materials in contact with the cantilever tip, thus enabling new applications and opportunities. For new applications of heated silicon cantilevers to utilize this functionality, improved understanding is required of the electrical and thermal characteristics of the cantilever.

1.1 Heated Atomic Force Microscopy

The AFM couples a nanoscopically sharp tip at the end of a soft cantilevered spring with sensitive displacement detection to enable sensitive force measurements with high spatial localization [1]. Figure 1.1 shows the basic principle of AFM. In the most common configuration, a microfabricated cantilevered beam with a sharp tip is used as a probe to ‘feel’ the surface of a substrate being scanned beneath the tip while a position-sensitive photodiode monitors deflections of the cantilever induced by topographical variation of the substrate or other interaction forces. Finely controlled piezoelectric actuators control motion of the cantilever tip relative to the substrate of interest. Integration of feedback and data acquisition allows high-resolution topographical mapping of substrates and highly sensitive force detection. The capabilities of AFM for

high spatial localization and sensitive force measurement have spawned numerous applications including localized domain imaging [2, 3], lithography [4-7], material characterization [8], and thermodynamic measurements of chemical and biomolecular interactions [9-11].

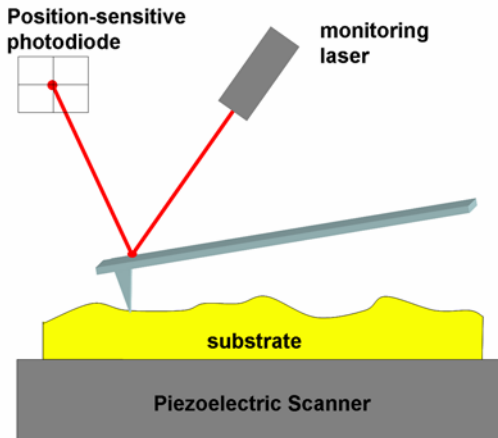


Figure 1.1 Principle of AFM operation. A microfabricated cantilever with a sharp tip is deflected by surface topography and a sample is scanned beneath it. Deflections of the cantilever cause motion of a reflected laser beam which is detected by a photodiode.

Some of the most significant advancements in AFM have occurred in probe design. Sensors, coatings, microfabricated structures, and actuators have all been incorporated into probes to enhance probe functionality [3, 4, 9, 11-19]. Among actuated probes, several applications for thermal actuation have developed, which can broadly be divided into 2 categories. In the first category, heat enables mechanical actuation of the probe through the thermal bimorph effect [18, 20]. In the second category, heating raises the temperature of the AFM tip, allowing the tip to act as a localized heat delivery source for performing lithography [4, 7, 21] and measuring calorimetric [22-24], thermal [23], and topographical [4] substrate properties.

1.2 Motivation for Using Silicon Heated AFM Cantilevers

Three primary probe designs have emerged for heated AFM applications in which the tip is used as a localized heat delivery source. The first 2 probe designs utilize microscale metal heaters and require individual assembly and have limited tip sharpness [17, 25], while in the third design the probe is fabricated from doped silicon using standard batch microfabrication methods, and is shown in Figure 1.2 [26]. The use of standard silicon micromachining processes enables parallelization [27], low cost, and tip sharpness equivalent to the current state of the art through oxidation sharpening, none of which are possible with the previous types of heated probes.

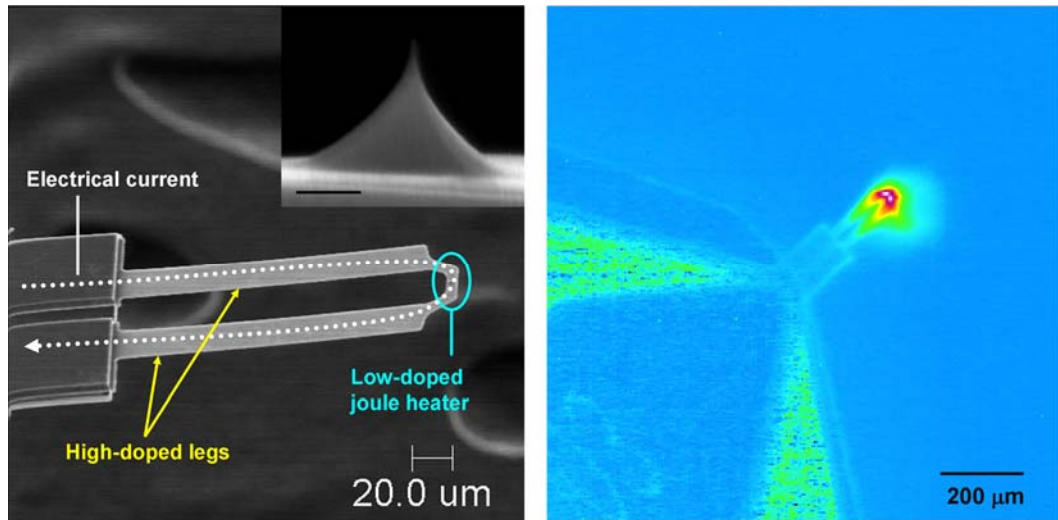


Figure 1.2 Scanning electron microscope (left) and infrared microscope (right) images of silicon heated AFM cantilevers. The highly-doped legs of the cantilever are conductive, while the low-doped bridge at the end creates a resistive heating element. The IR image confirms the localized heating at the end of the cantilever. The SEM inset shows a cantilever tip with radius of curvature below 20 nm. The scale bar in the inset corresponds to 300 nm.

The development of batch-fabricated heated cantilevers was crucial for several reasons. Since AFM is an inherently serial process, the throughput of any application using AFM tips as processing tools can only be increased and made commercially viable by operating the tips in parallel [4, 28-30], which is impractical or impossible for

individually fabricated probes. Furthermore, many applications for standard AFM cantilevers inherently require the nanoscale resolution offered by the sharp AFM tip [6, 9], so a thermal cantilever must retain the tip sharpness and lateral resolution of a standard tip in order to offer enhanced functionality. Retaining optimal tip sharpness requires bulk micromachining techniques such as oxide sharpening.

1.3 Previous Work and Current Needs

Although initially developed for data storage [4, 28], heated silicon cantilevers have now also been used to examine effects of wear on polymer substrates [31], map thermal properties of biological samples [32], detect topography thermally [33], and measure gas thermophysical properties [34, 35]. Heated silicon cantilevers add the functionality of temperature control to any existing application with standard AFM cantilevers and add the lateral resolution of standard AFM tips to any existing application with heated cantilevers, so potential still exists for many more applications. For example, AFM-based nanolithography techniques could benefit from thermal modulation of patterning [6, 36-38] and temperature control could be utilized in measuring intermolecular interaction energies [10]. Metal heater-based AFM probes have been used for spatially-resolved calorimetry, but gave insufficient lateral resolution to interrogate narrow regions of interest, such as those near to a surface and in interphase regions of composites [39-41].

Realizing the full capability of heated silicon cantilevers in any new application requires improved understanding of the electrical and thermal behavior of the cantilevers. For data storage, rough estimates of the cantilever temperature were sufficiently accurate

since the cantilever was used as a processing tool rather than as a measurement instrument, whereas precise thermal calibration is required for quantitative thermal measurements with the cantilevers. Furthermore, the temperature that governs substrate phenomena in thermal processing applications is the temperature at the tip-substrate interface, which is not generally the same as the calibrated cantilever heater temperature. Needs therefore exist for evaluating and optimizing the thermal calibration of silicon heated cantilevers as well as for further elucidating the dependence of the tip-substrate interface temperature on the physical parameters of the tip and substrate.

1.4 Dissertation Overview

This dissertation aims to advance the current state of use of silicon heated AFM cantilevers through two thrusts. The first thrust aims to improve the experimental and theoretical characterization of the cantilever behavior to improve the accuracy and precision of temperature-dependent measurements. The second thrust aims to develop new applications for the cantilevers that capitalize on their advantages in cost, lateral resolution, and parallelizability.

Chapter 2 reviews the previously reported applications of all types of heated AFM cantilevers. The applications range from mechanical actuation to lithography to chemical sensing. Chapter 3 then presents an analysis and optimization of the electrical and thermal calibration of heated silicon AFM cantilevers, identifying accuracy limits for each of the thermal calibration techniques. A full calibration methodology for precision use of the cantilevers is proposed and verified through measurements of calibration stability and finite difference heat transfer simulations.

Chapters 4 and 5 both demonstrate new applications utilizing heated silicon cantilevers. Chapter 4 describes controllable and localized deposition of metal from the AFM tip. The thermally modulated deposition process allows the cantilever tip to maintain its full functionality as a metrology tool. In the first electrical test of an AFM-deposited structure, the electrical continuity of the metal is measured to assess its functionality. Chapter 5 describes several techniques for characterizing substrate softening temperatures with nanoscale spatial resolution by using the heated AFM tip to induce softening. The described techniques are parallelizable and so can be utilized with cantilever array operation. The sampling resolution of the silicon cantilevers yields several orders of magnitude of improvement in sampling resolution over previous results with metallic heater cantilevers, enabling measurements in regions that were previously too small to be examined.

Chapter 6 describes an analytical model for heat transfer through the cantilever tip, incorporating arbitrary tip and substrate materials and geometries. The model identifies a number of dimensionless parameters and key properties that govern the heat transport through the tip and control the tip-substrate interface temperature. The sensitivity of the tip-substrate interface temperature to experimental parameters is explored, which is important for comparing temperature-dependent measurements in heterogeneous environments. Chapter 7 concludes the dissertation by listing the summary and conclusions of the work. Future applications for the cantilevers aided and identified by the work described herein are suggested. Necessary refinements of the experimental and theoretical cantilever characterization are also identified.

1.5 References

- [1] G. Binnig and C. Quate, Atomic force microscope, *Physical Review Letters*, 56 (1986) 930-933.
- [2] A. Karim, T. M. Slawecki, S. K. Kumar, J. F. Douglas, S. K. Satija, C. C. Han, T. P. Russell, Y. Liu, R. Overney, O. Sokolov and M. H. Rafailovich, Phase-separation-induced surface patterns in thin polymer blend films, *Macromolecules*, 31 (1998) 857-862.
- [3] J. Saenz, N. Garcia, P. Grutter, E. Meyer, H. Heinzelmann, R. Weisendanger, L. Rosenthaler, H. Hidber and H.-J. Guntherodt, Observation of magnetic forces by atomic force microscopy, *Journal of Applied Physics*, 62 (1987) 4293-4295.
- [4] G. Binnig, M. Despont, U. Drechsler, W. Haberle, M. Lutwyche, P. Vettiger, H. J. Mamin, B. W. Chui and T. W. Kenny, Ultrahigh-density atomic force microscopy data storage with erase capability, *Applied Physics Letters*, 74 (1999) 1329-1331.
- [5] R. Garcia and M. Calleja, Patterning of silicon surfaces with noncontact atomic force microscopy: Field-induced formation of nanometer-size water bridges, *Journal of Applied Physics*, 86 (1999) 1898-1903.
- [6] R. D. Piner, J. Zhu, F. Xu, S. Hong and C. A. Mirkin, "Dip-Pen" Nanolithography, *Science*, 283 (1999) 661-663.
- [7] P. E. Sheehan, L. J. Whitman, W. P. King and B. A. Nelson, Nanoscale deposition of solid inks via thermal dip pen nanolithography, *Appl. Phys. Lett.*, 85 (2004) 1589-1591.
- [8] C. Mate, M. Lorenz and V. Novotny, Atomic Force Microscopy of Polymeric Liquid Films, *J. Chem. Phys.*, 12 (1989) 7550-7555.
- [9] E. Florin, V. Moy and H. Gaub, Adhesion forces between individual ligand-receptor pairs, *Science*, 264 (1994)
- [10] T. A. Sulchek, R. W. Friddle, K. Langry, E. Y. Lau, H. Albrecht, T. V. Ratto, S. J. DeNardo, M. E. Colvin and A. Noy, Dynamic force spectroscopy of parallel individual Mucin1-antibody bonds, *Proceedings of the National Academy of Sciences of the United States of America*, 102 (2005) 16638-16643.

- [11] M. A. Poggi, P. T. Lillehei and L. A. Bottomley, Chemical force microscopy on single-walled carbon nanotube paper, *Chemistry of Materials*, 17 (2005) 4289-4295.
- [12] L. Shi, S. Plyasunov, A. Bachtold, P. McEuen and A. Majumdar, Scanning thermal microscopy of carbon nanotubes using batch-fabricated probes, *Applied Physics Letters*, 77 (2000) 4295-4297.
- [13] N. Moldovan, K. H. Kim and H. D. Espinosa, Design and fabrication of a novel microfluidic nanoprobe, *Journal of Microelectromechanical Systems*, 15 (2006) 204-213.
- [14] T. Akiyama, U. Stauffer and N. F. de Rooij, Fast driving technique for integrated thermal bimorph actuator toward high-throughput atomic-force microscopy, *Review of Scientific Instruments*, 73 (2002) 2643-2646.
- [15] A. G. Onaran, M. Balantekin, W. Lee, W. L. Hughes, B. A. Buchine, R. O. Guldiken, Z. Parlak, C. F. Quate and F. L. Degertekin, A new atomic force microscope probe with force sensing integrated readout and active tip, *Review of Scientific Instruments*, 77 (2006) 023501.
- [16] R. Pedrak, T. Ivanov, K. Ivanova, T. Gotszalk, N. Abedinov, I. W. Rangelow, K. Edinger, E. Tomerov, T. Schenkel and P. Hudek, Micromachined atomic force microscopy sensor with integrated piezoresistive sensor and thermal bimorph actuator for high-speed tapping-mode atomic force microscopy phase-imaging in higher eigenmodes, *Journal of Vacuum Science and Technology B*, 21 (2003) 3102-3107.
- [17] R. J. Pylkki, P. J. Moyer and P. E. West, Scanning near-field optical microscopy and scanning thermal microscopy, *Japanese Journal of Applied Physics*, 33 (1994) 3785-3790.
- [18] T. Sulchek, S. C. Minne, J. D. Adams, D. A. Fletcher, A. Atalar, C. F. Quate and D. M. Adderton, Dual integrated actuators for extended range high speed atomic force microscopy, *Appl. Phys. Lett.*, 75 (1999) 1637-1639.
- [19] X. Wang, D. A. Bullen, J. Zou, C. Liu and C. Mirkin, Thermally actuated probe array for parallel dip-pen nanolithography, *Journal of Vacuum Science and Technology B*, 22 (2004) 2563-2567.
- [20] A. Hierlemann, D. Lange, C. Hagleitner, N. Kerness, A. Koll, O. Brand and H. Baltes, Application-specific sensor systems based on CMOS chemical microsensors, *Sensors and Actuators B*, 70 (2000) 2-11.

- [21] B. A. Nelson, W. P. King, A. R. Laracuate, P. E. Sheehan and L. J. Whitman, Direct deposition of continuous metal nanostructures by thermal dip-pen nanolithography, *Appl. Phys. Lett.*, 88 (2006) 033104.
- [22] R. Berger, H. Lang, C. Gerber, J. Gimzewski, J. Fabian, L. Scandella, E. Meyer and H. Guntherodt, Micromechanical thermogravimetry, *Chem. Phys. Lett.*, 294 (1998) 363-369.
- [23] A. Hammiche, D. J. Hourston, H. M. Pollock, M. Reading and M. Song, Scanning thermal microscopy: subsurface imaging, thermal mapping of polymer blends, and localized calorimetry, *Journal of Vacuum Science and Technology B*, 14 (1996) 1486-1491.
- [24] L. A. Pinnaduwege, A. Wig, D. L. Hedden, A. Gehl, D. Yi, T. Thundat and R. T. Lareau, Detection of trinitrotoluene via deflagration on a microcantilever, *J. Appl. Phys.*, 95 (2004) 5871-5875.
- [25] M. H. Li and Y. B. Gianchandani, Microcalorimetry applications of a surface micromachined bolometer-type thermal probe, *Journal of Vacuum Science & Technology B*, 18 (2000) 3600-3603.
- [26] B. W. Chui, T. D. Stowe, Y. S. Ju, K. E. Goodson, T. W. Kenny, H. J. Mamin, B. D. Terris, R. P. Ried and D. Rugar, Low-stiffness silicon cantilevers with integrated heaters and piezoresistive sensors for high-density AFM thermomechanical data storage, *Journal of Microelectromechanical Systems*, 7 (1998) 69-78.
- [27] M. Lutwyche, C. Andreoli, G. Binnig, J. Brugger, U. Drechsler, W. Haberle, H. Rohrer, H. Rothuizen, P. Vettiger, G. Yaralioglu and C. Quate, 5X5 2D AFM cantilever arrays a first step towards a Terabit storage device, *Sensors and Actuators a-Physical*, 73 (1999) 89-94.
- [28] P. Vettiger, G. Cross, M. Despont, U. Drechsler, U. Durig, B. Gotsman, W. Haberle, M. Lantz, H. Rothuizen, R. Stutz and G. Binnig, The "millipede" - nanotechnology entering data storage, *IEEE Transactions on Nanotechnology*, 1 (2002) 39-55.
- [29] D. Bullen, X. F. Wang, J. Zou, S. W. Chung, C. A. Mirkin and C. Liu, Design, fabrication, and characterization of thermally actuated probe Arrays for dip pen nanolithography, *Journal of Microelectromechanical Systems*, 13 (2004) 594-602.

- [30] K. Salaita, Y. H. Wang, J. Fragala, R. A. Vega, C. Liu and C. A. Mirkin, Massively parallel dip-pen nanolithography with 55000-pen two-dimensional arrays, *Angewandte Chemie-International Edition*, 45 (2006) 7220-7223.
- [31] B. Gotsmann and U. Durig, Thermally activated nanowear modes of a polymer surface induced by a heated tip, *Langmuir*, 20 (2004) 1495-1500.
- [32] W. Haeberle, M. Pantea and J. K. H. Hoerber, Nanometer-scale heat-conductivity measurements on biological samples, *Ultramicroscopy*, 106 (2006) 678-686.
- [33] W. P. King, T. W. Kenny and K. E. Goodson, Comparison of thermal and piezoresistive sensing approaches for atomic force microscopy topography measurements, *Applied Physics Letters*, 85 (2004) 2086-2088.
- [34] B. Gotsmann and U. Durig, Experimental observation of attractive and repulsive thermal forces on microcantilevers, *Appl. Phys. Lett.*, 87 (2005) 194102.
- [35] J. Lee, T. L. Wright, M. R. Abel, E. O. Sunden, A. Marchenkov, S. Graham and W. P. King, Thermal conduction from microcantilever heaters in partial vacuum, *Journal of Applied Physics*, 101 (2007) 014906.
- [36] S. Rozhok, R. Piner and C. Mirkin, Dip-pen nanolithography: What controls ink transport?, *Journal of Physical Chemistry B*, 107 (2003) 751-757.
- [37] S. Bakbak, P. J. Leech, B. E. Carson, S. Saxena, W. P. King and U. H. F. Bunz, 1,3-dipolar cycloaddition for the generation of nanostructured semiconductors by heated probe tips, *Macromolecules*, 39 (2006) 6793-6795.
- [38] B. Gotsmann, U. Duerig, J. Frommer and C. J. Hawker, Exploiting chemical switching in a Diels-Alder polymer for nanoscale probe lithography and data storage, *Adv. Func. Mat.*, 16 (2006) 1499-1505.
- [39] T. Grossetete, L. Gonon and V. Verney, Submicrometric characterization of the heterogeneous photooxidation of polypropylene by microthermal analysis, *Polymer Degradation and Stability*, 78 (2002) 203-210.
- [40] D. Q. M. Craig, V. L. Kett, C. S. Andrews and P. G. Royall, Pharmaceutical applications of micro-thermal analysis, *Journal of Pharmaceutical Sciences*, 91 (2002) 1201-1213.

[41] T. T. Moore and W. J. Koros, Non-ideal effects in organic-inorganic materials for gas separation membranes, *Journal of Molecular Structure*, 739 (2005) 87-98.

CHAPTER 2

REVIEW OF APPLICATIONS OF HEATED ATOMIC FORCE MICROSCOPE CANTILEVERS

In atomic force microscope (AFM) cantilevers, the application of heat can be used to provide mechanical actuation, allow local heat flow measurements, and process materials locally through directed heating. Mechanical actuation by temperature-induced bending has been used for sensing temperature, inducing oscillation, and controlling individual cantilevers in arrays. Local measurement of heat flow can yield information about the thermal properties or topography of a substrate, enabling discrimination between heterogeneous materials. Thermal processing of materials on the cantilever itself has been used for calorimetry and explosives detection, while thermal processing of substrates beneath the AFM tip has been used for lithography, surface characterization, and data storage. Table 2.1 shows a summary of the applications of heated AFM cantilevers.

Heat sources for AFM cantilevers can be either internal or external to the cantilever. Internal heat sources have been electrically-resistive heaters made from metal or doped silicon. External heat sources have included focused lasers as well as global heating from furnaces or proximal heaters.

The transduction mechanisms for heated AFM cantilever applications have been either mechanical or electrical. Mechanical responses have included shifts in cantilever resonance due to mass changes, used during mass and chemical sensing, and cantilever

deflections due to temperature-induced bending, used during calorimetry of on-cantilever samples. Electrical responses utilized the temperature-sensitive resistance of on-cantilever resistors for thermometry, and have been important in lithography and in heat flow measurements [1].

Table 2.1. Uses and applications of heated cantilevers

Use	Applications
Actuation	High-speed imaging Controlling cantilever functionality Resonant Detection
Heat Flow Sensing	Thermal property measurement Subsurface imaging Topographical imaging
Substrate Thermal Processing	Data storage Lithography Local Thermal Analysis
On-cantilever Thermal Processing	Calorimetry Explosives detection Thermogravimetry Oxidative tip sharpening

2.1 Fabrication of Cantilevers With Integrated Heaters

Many designs for integrating heaters into AFM cantilevers have emerged. The heaters have been formed either from thin metal leads or doped silicon, and have been made both by hand and by utilizing batch fabrication techniques. The probes described below are the most prevalently used, although there have been some other probe designs as well [2-4].

2.1.1 Wollaston Wire Probe

The first probe with an integrated resistive heater designed for simultaneous topographical and thermal imaging was made from a Wollaston process wire consisting of a 75 μm Ag sheath and a 5 μm Pt core [5]. The wire was bent at a sharp angle and the silver was etched away at the apex of the bend, yielding a 200 μm section of exposed Pt wire to form the tip. The temperature-dependence of the resistivity of Pt allowed the exposed piece of wire to act both as a thermometer and as a resistive heater. A mirror affixed across the wire legs allowed probe deflection to be monitored with standard AFM optics for topographical measurements.

Although an effective localized heat source, the Wollaston probe had two primary drawbacks. First, Wollaston wire probes yielded poor lateral resolution, near 1.5 μm [6], which is much larger than the lateral resolution limits of standard silicon AFM probes, which is on the order of 10 nm. Second, the wire probes require individual assembly, resulting in high cost.

2.1.2 Polyimide Probe

The Wollaston and other electrically-active probes were not well-suited for use in aqueous and biological environments because of limited thermal isolation, exposed electrical connections, and relatively high spring constants. To address these limitations, cantilevers were developed with a thin film Ni/W resistor sandwiched between layers of polyimide [7, 8]. The polyimide cantilever material provided low thermal conductivity for thermal isolation from the ambient medium, low stiffness for imaging soft biological

samples, and low electrical conductivity for electrical isolation of the heater from the ambient medium.

2.1.3 Silicon Heated Cantilevers

To batch fabricate heated AFM cantilevers with lateral resolution equivalent to state-of-the-art silicon probes, doped-silicon resistive heaters had to be incorporated into the cantilever. Although not designed specifically for such uses, piezoresistive cantilevers could be used for heating applications by overbiasing the piezoresistor [9-12]. Silicon heater cantilevers have been fabricated with integrated doped-silicon resistors specifically designed for resistive heating [13-15]. The cantilevers were originally developed for the data storage application described in section 2.4.1.1, but have been fabricated within our own group at GeorgiaTech. Figure 1.2 showed one of the probes made by our group, which consist of a U-shaped single crystal silicon cantilever, where the legs of the ‘U’ are highly doped and electrically conductive and the bridge of the U is low-doped, creating a resistive heater within the current path. When current flows through the probe, resistive heating near the cantilever tip can raise the cantilever tip temperature to over 1000 °C. The silicon probe is batch-fabricated, which enables parallelization [16], low cost, and tip sharpness equivalent to the current state of the art by utilizing oxide-sharpening.

2.2 Thermal Actuation of AFM Cantilevers

The application of heat can induce mechanical actuation of cantilevers through mismatch in thermal expansion across the cantilever. The mismatch in expansion can be

achieved either through variation in materials or through temperature gradients within the cantilever. Mechanical actuation of cantilevers is required for i) fast mechanical response times, which has applications in high speed AFM imaging; ii) for individual cantilever control, which has applications in lithography and chemical sensing; and iii) for measuring changes in cantilever resonant frequency, which has applications in chemical sensing.

2.2.1 AFM Imaging

A limitation in conventional atomic force microscopy is the image acquisition speed, which is primarily limited by the ~600 Hz bandwidth of the vertical piezotube scanner. Cantilever arrays can increase throughput but require deflection sensing and actuation for each cantilever. To address these challenges, piezoelectric and thermal bimorph vertical actuators have been fabricated directly onto individual cantilevers, enabling faster response times due to the smaller actuated masses and allowing individual cantilever actuation [17-22].

On-cantilever piezoelectric actuation has demonstrated a bandwidth of 33 kHz, which is a significant improvement over piezotube vertical actuation [23]. However a tradeoff exists between improving the bandwidth and limiting the total vertical range since the cantilever resonant frequency scales linearly with the cantilever thickness while the maximum vertical range scales with the inverse of the thickness [20]. To achieve both wide bandwidth and large vertical range, cantilevers were fabricated with both piezoelectric actuators for responding to small amplitude, high spatial frequency topographical variation, and thermal actuators for large amplitude, low spatial frequency variation, achieving a 15 kHz imaging bandwidth with a vertical range of a few microns

[20]. Constant force images were taken with one such cantilever at 2 mm/s tip velocity with 2.5 μm peak to valley height, which Figure 2.1 shows [20].

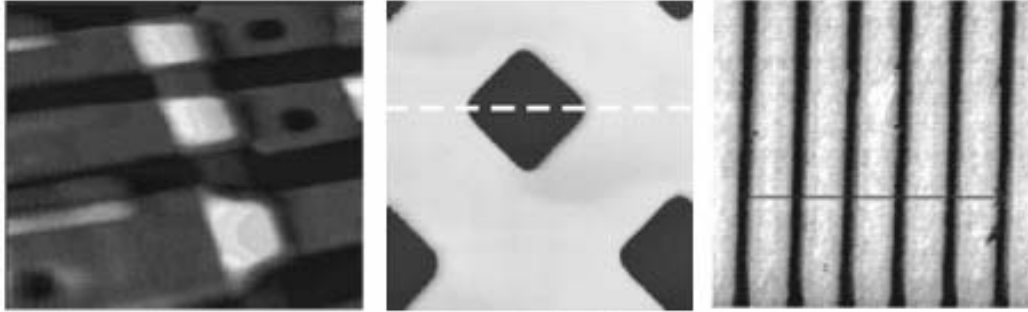


Figure 2.1 AFM images taken at high speed using thermal actuation for vertical control. *Left:* AFM image of metal lines and contact holes with over 2 μm variation, taken at 2 mms^{-1} using parallel thermal and piezoelectric vertical actuation [20]. *Middle:* AFM image of 5 μm square pits with 180 nm step height taken at .62 mms^{-1} using a tuned boost filter and purely thermal actuation [18]. *Right:* Alternate-contact mode AFM image of a 40 nm tall chromium pattern with 1 μm period imaged at .1 mms^{-1} tip velocity [22].

The cantilevers with integrated piezoelectric and thermal actuators were not well suited for array operation due to the complexity required to address electrical connections for multiple actuators on each cantilever and the need for external deflection sensing to control the contact force. On-cantilever sensing and actuation was achieved using CMOS processing to fabricate a cantilever with integrated thermal actuation and piezoresistive deflection sensing [17]. Later efforts to improve the dynamic performance of thermal actuation added an active boost filter [18]. Because the thermomechanical response of the cantilever occurred over a finite time period, higher heating voltages could be initially applied to the actuator to rapidly induce deflection, and then the voltage could be decreased to maintain that deflection. The initially high voltage caused the cantilever to deflect more quickly compared to if the lower voltage were held constant the whole time, yielding a 5 kHz imaging bandwidth and .62 mm/s imaging speed, as Figure 2.1 shows [18]. To further enable improvements to AFM imaging throughput, CMOS processing was used to fabricate a cantilever array with multiplexing, thermal actuation and

piezoresistive wheatstone bridge deflection sensing all integrated on-chip, demonstrating scan speeds of .6 mm/s with a custom analog controller [21].

To minimize contact forces while still achieving on-cantilever actuation for maximum imaging bandwidth, alternate-contact (tapping) mode imaging with integrated thermal actuation was also demonstrated at scan speeds of .1 mm/s, which Figure 2.1 shows [22]. An AC current matched to the resonant frequency of the cantilever excited oscillation while a DC current actuated the cantilever for tracking topography.

2.2.2 Individual Cantilever Control

On-cantilever thermal actuation can be used to control the functionality of individual cantilevers by physically bringing the cantilever tip into or out of contact with a device or substance. The ability to control the functionality of individual cantilevers is especially important when cantilevers are operated in parallel arrays, such as those that have been developed for dip pen nanolithography (DPN). In DPN, a chemically-coated AFM cantilever tip locally transfers chemicals ‘inks’ from an inked probe tip to a substrate, producing features as small as 10 nm [24]. One challenge for DPN is that chemicals will transfer from the tip to the surface whenever the chemically-coated tip is in contact with the surface [25-27]. The uncontrolled chemical transfer can lead to contamination when performing post-deposition metrology with chemical-coated tips and when performing lithography using arrays of tips with different chemical tip-coatings.

Thermal bimorph cantilevers have been developed to modulate DPN writing by actuating the AFM tip into and out of contact with a surface [28-30]. In the thermal bimorph actuation approach, silicon nitride cantilevers were coated with a chrome/gold heater. When cold, the cantilevers were relatively flat and appropriate positioning of the

cantilever could bring the tips into contact with the substrate. Applying heat to a cantilever caused the cantilever to bend such that the actuated tips broke contact with the substrate, thereby modulating chemical deposition from the tip to the substrate. A nominal single-cantilever heating power of 2 mW produced a tip deflection of 10 μm in ~ 1 ms. Controlled deposition of ODT from an array of ten individually addressable cantilevers was demonstrated, meeting the requirement for control of tip-substrate contact [28].

Another application utilizing thermal actuation to control the functionality of an AFM probe integrated a time-of-flight mass spectrometer (TOF-MS) with AFM for combined topographical and chemical analysis [31]. The integration of mass spectrometry with AFM enabled determining chemical compositions of surfaces during AFM. The cantilever was mounted onto a custom microstage and was thermally actuated between two positions. In the imaging position, the cantilever was pointed downwards to image the surface and adsorb chemical species off the substrate. In the extraction position, the thermal bimorph switched the cantilever up to the extraction electrode where chemical compounds on the tip were ionized and accelerated towards the TOF-MS to determine the chemical species picked up during imaging. The proximity between the tip and extraction electrode in this system significantly reduced the required voltage for desorption and ionization over standard TOF-MS [32].

2.2.3 Resonant Detection

Adsorption of ambient chemicals onto functionalized cantilevers can induce measurable cantilever bending or resonant frequency shifts, making cantilevers highly sensitive chemical sensors [33]. One study used thermal actuation to measure changes in

the resonant frequency of a cantilever under different concentrations of ethanol, *n*-octane, ethyl acetate, and toluene [34]. The cantilever was coated with poly(etherurethane) to make it chemically sensitive to the chosen organic analytes, and adsorption of the analytes from the air caused an increase in mass of the cantilever, inducing a resonance frequency shift that was linearly dependant on the analyte concentration.

2.3 Local Heat Flow Measurements

The high lateral resolution of AFM tips enables highly local measurements of heat flow from heated AFM cantilevers. The localization of the heat flow enables generating maps of the thermal and topographical characteristics of the substrates below the tip.

2.3.1 Mapping Thermal Conductivity

When two or more materials are blended together within a substrate, the contrast in the thermal properties of the various phases can be used to differentiate between the otherwise smoothly-blended materials. Local heat flow measurement from a heated AFM probe can be used to qualitatively map the thermal conductivity of the substrate material beneath the probe tip since the substrate thermal conductivity constitutes a proportion of the total thermal conductance from the probe heater [6, 35-38]. The heat flow from a probe can be related to its temperature by

$$Q = G(T_{probe} - T_{\infty}) \quad (2.1)$$

where Q is the heat flow from the probe, T_{probe} is the probe temperature, T_{∞} is the ambient temperature, and G is the thermal conductance from the heater. Variation in the thermal conductance stems both from variation in the thermal conductivity of the

substrate as well as from the topography. For relatively dull tips, such as that of the Wollaston wire probe, strong thermal coupling between the tip and substrate causes the substrate thermal conductivity to constitute the dominant contribution to G . Thus, recording the required power to maintain constant cantilever temperature or recording the temperature during supply of constant power during imaging generates a qualitative map of the substrate thermal conductivity. The technique can even detect thermal conductance variation due to the presence of subsurface inhomogeneities, thus enabling imaging of buried structures. Thermal conductance maps exhibit some convolution with topographical variation, and some recent efforts have focused on developing statistical techniques to remove topographical artifacts from thermal conductivity images [39].

The first thermal conductivity map and subsurface image was generated by Nonnenmacher and Wickramasinghe in 1992 [36]. Using a laser-heated AFM cantilever and measuring the cantilever temperature from the electrical contact potential between the tip and the scanned sample resulted in detection of a SiO_2 structure buried underneath a tungsten film. The potential for subsurface imaging was more thoroughly examined by experiments with a Wollaston probe heated 20 °C above ambient to perform thermal imaging of copper particles buried at different depths [6], demonstrating a depth of vision of a few microns. The Wollaston probe also was used to characterize carbon fibers within carbon composites [37] and pharmaceuticals [39], yielding significantly improved material contrast over the corresponding topographical images.

AC cantilever heating was also used for heat flow measurements, , in which case the amplitude and phase lag of the temperature response in the cantilever yield information about the thermal diffusivity of the surface, compared to DC heating which

yields information strictly about thermal conductivity [3, 35, 40]. AC heating also permitted lock-in techniques to improve the signal-to-noise ratio over that of DC heating.

In the first use of AC heating for thermal property mapping, a chopped laser heated a thermocouple probe to illuminate grain boundaries during imaging of a topographically flat diamond surface [40]. In another study, the phase lag between heating and the thermal response of a Wollaston probe delineated between the mixed components of a polymer blend [35]. In a related method for mapping substrate thermal properties, later research optically monitored cantilever deflection while an AC heating current induced thermal expansion of the substrate during imaging [3]. This method differs from Scanning Joule Expansion Microscopy (SJEM) in that the probe was heated rather than the sample [41]. Contrast in such expansion images indicated variations in both thermal diffusivity and thermal expansion coefficient.

In spite of the advances in thermal property mapping and subsurface imaging, results have remained largely qualitative and not quantitative. One primary challenge is for Wollaston probes, where theoretical estimates show that a significant portion of the supplied power is lost through the silver sheath to the surrounding air, resulting in nonlinearity between substrate thermal conductivity and the required heating power to maintain constant probe temperature [42, 43]. One study attempted to develop a semi-empirical correlation relating substrate thermal conductivity to the ratio of the power required to maintain constant probe temperature in contact with the substrate to the power required when out of contact with the substrate [44]. Although the empirically-fit model matched the general trend of power ratio variation with substrate thermal conductivity, the model could not give accurate determination of thermal conductivity from a given

power ratio. Another approach for quantifying substrate response to heated probes developed an approximate analytical model for the temperature distribution in the substrate during DC and AC heating, enabling rapid results for variable experimental conditions [45]. This model, however, neglected conduction from the sides of the tip and power dissipation through the probe leads. The lack of accurate models to enable quantitative measurements is the primary shortcoming in thermal conductivity mapping.

2.3.2 Thermal Imaging

For much sharper probe tips, such as that of silicon probes, the thermal conductance G in Eq. ((2.1) is dominated by topographical effects, which control the separation distance between the substrate and the cantilever heater. When the tip of a warm cantilever follows the contours of a surface, changes in the gap between the warm cantilever and the substrate induce changes in G , and local variations in the heat flow from the probe reflect variations in the topography of the substrate. Thus, silicon heated AFM cantilevers can image topography thermally, eliminating the need for the external optics required for conventional AFM topographical measurements.

Use of thermal imaging for surface profiling was first demonstrated with a heated thermocouple tip elevated off the substrate by 100 nm or more [46]. The approach demonstrated 3 nm height resolution and 100 nm lateral resolution. A similar technique with a heated cantilever in contact with the substrate was later used to simplify the readback mechanism in a thermomechanical data storage application described in more detail in section 2.4.1.12.4.1 [14]. Since the data storage technology already used an integrated resistive heater to form data bits, relying on thermal topographical imaging eliminated the need for additional deflection-sensing elements. The integrated

topographical sensing enabled scaling to a 32x32 array [47] and simulations showed that the thermal cantilever was more sensitive than a similarly-sized piezoresistive cantilever by at least two orders of magnitude [48-50].

2.4 Material Processing

Heated AFM cantilevers can be used to induce phase changes both in the substrate beneath the AFM tip as well as in any substances adsorbed on the cantilever itself. The small size of the cantilevers leads to short thermal time constants and high sensitivity to changes in adsorbed mass. Additionally, the high lateral resolution of the sharp probe tip enables highly localized delivery of heat to a substrate through the tip.

2.4.1 Substrate Material Processing

2.4.1.1 Data Storage

Because of its ability to form and detect nanometer-scale structures, scanning probe microscopy has been considered a candidate technology for advanced data storage or nanolithography. The practical data density of magnetic disks will likely plateau in the range of 100-200 Gbit•in⁻² due to the superparamagnetic effect [51], and optical lithography could reach resolution limits near 50 nm [52]. Numerous scanning probe techniques have been suggested as possible alternatives to these limits [14, 24, 53-56]. AFM offers advantages over STM in that it is somewhat faster in single-probe operation, can be used on nonconducting surfaces, and is more easily parallelized.

The first demonstration of surface modification using a heated AFM cantilever tip employed a heating laser focused on a silicon nitride cantilever in contact with a thick

film of polymethyl-methacrylate (PMMA) [57]. Under a tip loading force of 0.1-1 μN , laser heating pulses of 15 mW and 0.3-100 μs heated the cantilever and cantilever tip, locally melting the polymer in contact with the tip. The tip penetrated into the polymer surface, forming a melted indentation of diameter 100 nm – 1 μm . The spatial resolution of the writing was governed by the tip sharpness, heating pulse duration, and cantilever load force. The same cantilever imaged the formed indents using standard AFM optical techniques. Reading was demonstrated at 100 kHz, with the 500 kHz upper bound on reading limited by the cantilever mechanical time constant. In general, a mechanical probe can follow surface contours at rate of three to four times its mechanical resonant frequency [58]. A related study examined thermomechanical recording using a tapered optical fiber instead of an AFM cantilever, with the goal of increasing speed and decreasing mechanical wear [59]. The fiber optical stylus produced indentations as small as 50 nm x 74 nm but was not able to read these indentations with sufficient signal-to-noise, although for bit sizes of 150 nm x 300 nm data reading was possible. For both of these studies, the instrumentation required for controlling position and performing writing and reading were more complex than was practical for data storage applications.

One simplification of the required instrumentation was to use an AFM cantilever with an integrated heating element. In a demonstration of using piezoresistive cantilevers for thermomechanical writing, short 40 mW electrical pulses delivered to a piezoresistive cantilever raised the cantilever temperature to above 700 $^{\circ}\text{C}$ [9]. The sharp silicon cantilever tip produced indents as small as 200 nm, but the 300-500 μs cantilever cooling time was quite long due to the large size of the heated region. The fabrication of heated AFM cantilevers designed specifically for data storage reduced the cantilever heating

time by fabricating a small heating element fabricated at the cantilever free end, very close to the cantilever tip [13]. Because the heater element was small and relatively isolated, 1-10 μ s heating and cooling time constants were possible. At this time, it was thought that a data storage device might use the heated AFM cantilevers for thermomechanical writing and use either additional piezoresistive cantilevers or a combination of both heating and piezoresistive sensors for reading [13]. Other groups eventually achieved this combination [60-62].

Several nearly consecutive improvements in the operation of AFM cantilevers with integrated heaters significantly improved their promise for practical use: an approach for high-density data bit writing, data reading using thermal probes, described in 2.3.2, and fabrication of two-dimensional cantilever arrays.

High-density thermomechanical writing was accomplished by writing indentations into a 40 nm thick PMMA layer prepared on top of a second layer of cross-linked epoxy [14]. Unlike previous thermomechanical data writing in polymers of thickness much greater than the tip height [9, 57, 59], this configuration limited tip penetration and thus also limited the width of the formed indent. The underlying epoxy layer minimized the wear incurred on the tip during data bit writing. Figure 2.2 shows thermomechanical data writing in a thin polymer film, and Figure 2.3 shows these indentations. In this polymer film stack, data bit spacing was as small as 40 nm, corresponding to a data density of 500 Gbit \cdot in⁻². Using the same approach, data bit indents were later written as small as 23 nm [15].

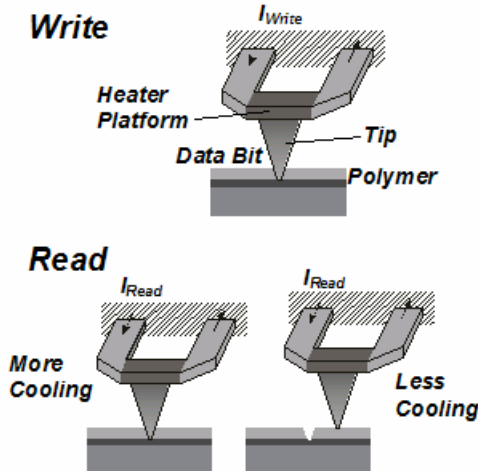


Figure 2.2 Thermomechanical writing and thermal reading in a thin polymer layer with a heated AFM cantilever tip [14]. In writing mode, the AFM cantilever is heated above the melting temperature of the polymer and indents into the polymer film. In reading mode, the cantilever detects topography by measuring thermal impedance from the cantilever

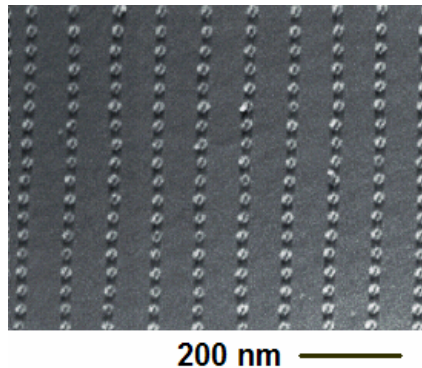


Figure 2.3 Thermally-read image of nanometer-scale indentations written into a thin polymer film [14].

The development of thermal data reading using the heated cantilevers was an essential simplification for scaling up the data storage cantilevers into arrays. In the thermal reading mode, the AFM cantilever was heated such that it was warm but not so hot that it deformed the polymer. As the warm cantilever scanned over the contours of the data-written polymer substrate, changes in thermal impedance between the cantilever and substrate induced measurable changes in the electrical resistance of the cantilever, illustrated in Figure 2.2. While not specifically designed for reading, the heated AFM cantilevers were sufficient to image the indents they formed and generated the thermal

image in Figure 2.3 [14]. Vertical displacement sensitivity was reported to be in the range of 10^{-6} - 10^{-5} nm⁻¹. Modeling and measurements later showed that heat transfer across the heater-substrate air gap rather than heat transfer down the cantilever tip governs this thermal reading mechanism [49]. However, the temperature rise in the tip allowed the thermomechanical writing. Therefore, because the heat transfer mechanisms for writing and reading were relatively independent, it was possible to optimize both writing and reading performance of the cantilever simultaneously [50]. Eventually an extremely small heater region was explored to reduce heating time [63], and the write/read operations were split into two separate heaters [64]. While it has not been studied in detail, the heated AFM cantilever could become a highly sensitive metrology tool. While AFM cantilevers with both integrated heaters and piezoresistive elements [60-62] may become valuable for other applications, the finding that the thermal cantilever is an excellent metrology tool made piezoresistor integration unnecessary for the success of this data storage technology.

Motivated by the need for high-speed data throughput, AFM cantilevers for data storage were the first type of cantilever to be fabricated in a two-dimensional array [65]. The use of an array for thermomechanical data storage was made possible through the dual read/write functionality of the heated AFM cantilever. Without the capability for integrated reading, an array of AFM cantilevers would require laser interrogation of every cantilever, optical interferometry of the entire chip, or additional electronics for individual piezoresistors on each cantilever in the array. Arrays of heated AFM cantilevers were first made in a 5 x 5 cantilever configuration [65] and eventually expanded to a 32 x 32 cantilever configuration [66, 67], known as “Millipede”. Figure

2.4 shows the Millipede cantilever and cantilever array. Operation of the cantilever array demonstrated data writing above $600 \text{ Gbit}\cdot\text{in}^{-2}$ at a single-cantilever writing rate near 100 kHz [64, 68].

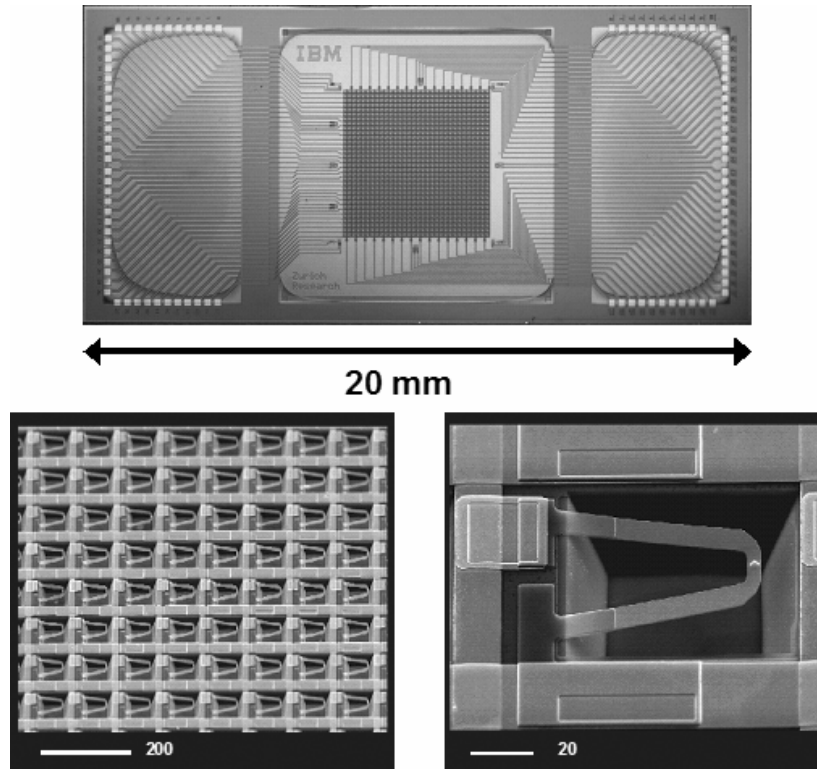


Figure 2.4 Photo of the 32×32 “Millipede” arrays of heater-cantilevers (*top*), and scanning electron microscope images of the arrayed cantilevers (*bottom left*) and a single cantilever (*bottom right*) [66, 67].

The development of AFM-based data storage using arrays of heated AFM cantilevers has made an impact on nanoscience and nanotechnology by enabling novel nanoscale thermal transport and temperature measurements, for example writing thermomechanical indentations using carbon nanotubes affixed to the cantilever tip [69] or studying nanoscale mechanical deformation and wear using highly local heating from the tip [70]. The technology developed could also have broad impact on the packaging of microelectromechanical systems [71]. An overview of lessons learned in the Millipede project is available [72].

2.4.1.2 Lithography

Several lithographic approaches have used heated AFM cantilevers. Femtosecond laser pulses were optically focused onto the tip of a cantilever to cause ablation on 25 nm thick gold films, achieving 10 nm lateral resolution [73]. The optics required in this technique make large-scale utilization difficult, however. An AFM cantilever heated by a resistively heated AFM probe holder melted crystalline nanospheres within a block copolymer [74], demonstrating the ability to melt single 24 nm crystalline domains. In an application using the ultracompliant polyimide probe described in section 2.1.2, heat supplied by the probe induced localized cross-linking in a commercial photoresist, demonstrating maskless photoresist-based lithography at a resolution of 450 nm [75]. Because of the high compliance of the probe, array operation without mechanical feedback was demonstrated with no apparent damage to the tip or deformation to the photoresist substrate.

2.4.1.3 Local Thermal Analysis

In Local Thermal Analysis (LTA), the tip of a heated probe was held stationary in contact with a polymer substrate while the probe temperature was raised until the substrate began to soften or melt. The melted region was confined to the microscale region of the substrate surrounding the tip, so specific domains identified from AFM imaging could be sampled to map spatial variations in the softening temperatures of heterogeneous substrates [76-78]. Substrate softening was indicated from discontinuities in the required heating power while the temperature was increased [79], from physical displacement of the tip into the softened substrate [3, 78], and from discontinuities in the AC amplitude and phase of the temperature response of the cantilever when a small AC

temperature dither was superimposed onto the temperature rise of the probe [80]. Discontinuities in the power, phase, and amplitude were initially attributed to changes in the heat capacity of the substrate during the softening phase transition, but was later attributed to the changing thermal conductance as the tip penetrated into the softened substrate [79, 81].

LTA has identified glass transition, recrystallization, and melting temperatures of various polymers [3, 80] and pharmaceuticals [82], and a similar experimental technique examined the softening temperature of carbon fibers to determine depth of oxidative stabilization [78].

2.4.2 On-Cantilever Material Processing

In addition to inducing phase changes on substrates beneath the AFM tip, heated AFM cantilevers can also be used to modify materials coating the cantilever. The small thermal and mechanical mass of the cantilever allows sensitive detection of energy changes during phase transitions and the corresponding mass changes.

2.4.2.1 Calorimetry

An AFM cantilever was sensitive enough to detect rotational phase transitions of a 7.8 ng $C_{21}H_{44}$ film coating the cantilever. The transitions were determined from discontinuities in the temperature variation of the $C_{21}H_{44}$ -coated cantilever during constant heating by a proximal heater [83]. The rotational transition was also detected for $C_{24}H_{50}$ and $C_{23}H_{48}$ [84]. An empirical calibration constant was suggested to attempt to quantitatively estimate the phase transition enthalpy change from the time-dependent

temperature response of the cantilever during heating, but the work was still highly qualitative.

2.4.2.2 Explosives Detection

In addition to detecting the energetics of reversible phase transitions, cantilevers can also detect the heat released by deflagration of trace quantities of explosives [12]. Using an overbiased piezoresistive cantilever as a heat source, detection of deflagration occurred only after the cantilever had been exposed to trinitrotoluene (TNT) and only at sufficiently large heating pulses. The deflagration signal was uninfluenced by common interfering substances such as water, acetone, ethanol, and gasoline [85, 86]. The heat released by the exothermic deflagration raised the cantilever temperature, inducing additional bending during heating pulses as compared to the bending response of the cantilever without TNT during identical heating pulses. After deflagration, the cantilever was clear of TNT and no further deflagration events occurred during subsequent heating. The degree of cantilever bending was linearly proportional to the mass of adsorbed TNT.

2.4.2.3 Thermogravimetry

Thermogravimetry involves the monitoring of sample weight loss as a function of temperature while heating a sample. Utilizing the mass sensitivity of the cantilever, an overbiased piezoresistive cantilever performed thermogravimetry on 420 ng of copper-sulfate-pentahydrate ($\text{CuSO}_4 \cdot 5\text{H}_2\text{O}$), detecting discrete dehydration steps during heating [11]. The resistivity of the piezoresistor was temperature-dependent, allowing use both as a heater and as a thermometer. Using a piezoelectric actuator to oscillate the cantilever, dehydration of the copper sulfate caused two discrete jumps in the cantilever resonant frequency during heating. In an effort to improve Joule-heated cantilevers for

thermogravimetry, finite element analysis modeled a cantilever design with a slit near the apex to create a thermal and electrical constriction, resulting in a more uniform temperature on the sample platform and an improved heating efficiency [87].

2.4.2.4 Oxidative Tip Sharpening

Cantilever tip sharpness and adhesive interactions determine lateral resolution in AFM. Silicon cantilever tips are sharpened by oxidizing the silicon and then removing the oxide. Oxidation is usually performed in a furnace, but oxides can also be grown on cantilever tips by localized heating [10, 88, 89]. A technique to do this used local heat from an overbiased piezoresistive cantilever under low oxygen pressure to oxidize, and then used local heat under vacuum to desorb the oxide [10]. The tip was first cleaned by Ar ion sputtering under vacuum to remove native oxide and contaminants. The tip was then heated by passing a large current through the piezoresistive cantilever under O₂ pressure of 5×10^{-5} torr to form a thin protective oxide layer, after which introduction into laboratory air for 10 min caused no adverse effects from contamination. The cantilever was then placed back under vacuum and again heated to desorb the oxide layer, resulting in a sharp, clean Si tip. Oxide desorption was later improved through stimulation with an electron beam [89]. After cleaning, the cantilevers exhibited enhanced imaging resolution and reduced noise in the resonant frequency variation with the tip-substrate separation distance, although no effort to quantify changes to the tip sharpness was reported.

2.5 Summary and Conclusions

Heated AFM cantilevers have been used for microsystems actuation, thermal property and topographical measurement, and thermal processing of various classes of

materials, but applications using these capabilities have only begun to realize their full potential. Many physical, chemical, and biological phenomena depend sensitively upon temperature, and the most interesting measurements likely are yet to be demonstrated. For example, few precision force measurements have been made with heated AFM cantilevers even though they are outstanding force transducers. Additionally, no investigations have explored the effects of heated probes as highly localized heat sources in biological or biochemical systems.

The most pressing unresolved issue in all of these applications, and for future applications, is the lack of precision quantitative measurements with well-understood uncertainty. The overall impact of heated AFM cantilever probes would be significantly enhanced by high-resolution temperature calibration, further quantitative investigation of heat flow in AFM probes, temperature determination at tip-substrate contacts, and possibly standardization of these across heated AFM cantilever probe types.

2.6 References

- [1] B. A. Nelson and W. P. King, *Applied Scanning Probe Methods IV*, Vol. 4, Springer-Verlag, Berlin, 2006.
- [2] K. Edinger, T. Gotszalk and I. W. Rangelow, Novel high resolution scanning thermal probe, *Journal of Vacuum Science and Technology B*, 19 (2001) 2856-2860.
- [3] A. Hammiche, L. Bozec, M. Conroy, H. M. Pollock, G. Mills, J. M. R. Weaver, D. M. Price, M. Reading, D. J. Hourston and M. Song, Highly localized thermal, mechanical, and spectroscopic characterization of polymers using miniaturized thermal probes, *Journal of Vacuum Science and Technology B*, 18 (2000) 1322-1332.
- [4] J. H. Bae, T. Ono and M. Esashi, Scanning probe with an integrated diamond heater element for nanolithography, *Appl. Phys. Lett.*, 82 (2003) 814.

- [5] R. J. Pylkki, P. J. Moyer and P. E. West, Scanning near-field optical microscopy and scanning thermal microscopy, *Japanese Journal of Applied Physics*, 33 (1994) 3785-3790.
- [6] A. Hammiche, H. M. Pollock, M. Song and D. J. Hourston, Sub-surface imaging by scanning thermal microscopy, *Measurement Science & Technology*, 7 (1996) 142-150.
- [7] M.-H. Li and Y. B. Gianchandani, Applications of a low contact force polyimide shank bolometer probe for chemical and biological diagnostics, *Sensors and Actuators A*, 104 (2003) 236-245.
- [8] M. H. Li and Y. B. Gianchandani, Microcalorimetry applications of a surface micromachined bolometer-type thermal probe, *Journal of Vacuum Science & Technology B*, 18 (2000) 3600-3603.
- [9] H. J. Mamin, Thermal Writing Using a Heated Atomic Force Microscope Tip, *Applied Physics Letters*, 69 (1996) 433-435.
- [10] T. Arai and M. Tomitori, Removal of contamination and oxide layers from UHV-AFM tips, *Applied Physics A*, 66 (1998) S319-S323.
- [11] R. Berger, H. Lang, C. Gerber, J. Gimzewski, J. Fabian, L. Scandella, E. Meyer and H. Guntherodt, Micromechanical thermogravimetry, *Chemical Physics Letters*, 294 (1998) 363-369.
- [12] L. A. Pinnaduwege, A. Gehl, D. L. Hedden, G. Muralidharan, T. Thundat, R. T. Lareau, T. Sulchek, L. Manning, B. Rogers, M. Jones and J. D. Adams, A microsensor for trinitrotoluene vapour, *Nature*, 425 (2003) 474.
- [13] B. W. Chui, T. D. Stowe, Y. S. Ju, K. E. Goodson, T. W. Kenny, H. J. Mamin, B. D. Terris and R. P. Ried, Low-Stiffness Silicon Cantilever with Integrated Heaters and Piezoresistive Sensors for High-Density Data Storage, *Journal of Microelectromechanical Systems*, 7 (1998) 69-78.
- [14] G. Binnig, M. Despont, U. Drechsler, W. Haberle, M. Lutwyche, P. Vettiger, H. J. Mamin, B. W. Chui and T. W. Kenny, Ultrahigh-density atomic force microscopy data storage with erase capability, *Applied Physics Letters*, 74 (1999) 1329-1331.

- [15] P. Vettiger, G. Cross, M. Despont, U. Drechsler, U. Durig, B. Gotsmann, W. Haberle, M. A. Lantz, H. E. Rothuizen, R. Stutz and G. K. Binnig, The "millipede" - Nanotechnology entering data storage, *Ieee Transactions on Nanotechnology*, 1 (2002) 39-55.
- [16] M. Lutwyche, C. Andreoli, G. Binnig, J. Brugger, U. Drechsler, W. Haberle, H. Rohrer, H. Rothuizen, P. Vettiger, G. Yaralioglu and C. Quate, 5X5 2D AFM cantilever arrays a first step towards a Terabit storage device, *Sens. Actuators, A*, 73 (1999) 89-94.
- [17] T. Akiyama, U. Staufer, N. F. de Rooij, D. Lange, C. Hagleitner, O. Brand, H. Baltes, A. Tonin and H. R. Hidber, Integrated atomic force microscopy array probe with metal-oxide-semiconductor field effect transistor stress sensor, thermal bimorph actuator, and on-chip complementary metal-oxide-semiconductor electronics, *Journal of Vacuum Science and Technology B*, 18 (2000) 2669-2675.
- [18] T. Akiyama, U. Staufer and N. F. de Rooij, Fast driving technique for integrated thermal bimorph actuator toward high-throughput atomic-force microscopy, *Review of Scientific Instruments*, 73 (2002) 2643-2646.
- [19] W. Franks, D. Lange, S. Lee, A. Hierlemann, N. Spencer and H. Baltes, Nanochemical surface analyzer in CMOS technology, *Ultramicroscopy*, 91 (2002) 21-27.
- [20] T. Sulchek, S. C. Minne, J. D. Adams, D. A. Fletcher, A. Atalar, C. F. Quate and D. M. Adderton, Dual integrated actuators for extended range high speed atomic force microscopy, *Applied Physics Letters*, 75 (1999) 1637-1639.
- [21] T. Volden, M. Zimmermann, D. Lange, O. Brand and H. Baltes, Dynamics of CMOS-based thermally actuated cantilever arrays for force microscopy, *Sensors and Actuators A*, 115 (2004) 516-522.
- [22] R. Pedrak, T. Ivanov, K. Ivanova, T. Gotszalk, N. Abedinov, I. W. Rangelow, K. Edinger, E. Tomerov, T. Schenkel and P. Hudek, Micromachined atomic force microscopy sensor with integrated piezoresistive sensor and thermal bimorph actuator for high-speed tapping-mode atomic force microscopy phase-imaging in higher eigenmodes, *Journal of Vacuum Science and Technology B*, 21 (2003) 3102-3107.
- [23] S. R. Manalis, S. C. Minne, A. Atalar and C. F. Quate, High-speed atomic force microscopy using an integrated actuator and optical lever detection, *Review of Scientific Instruments*, 67 (1996) 3294-3297.

- [24] R. D. Piner, J. Zhu, F. Xu, S. Hong and C. A. Mirkin, "Dip-Pen" Nanolithography, *Science*, 283 (1999) 661-663.
- [25] P. V. Schwartz, Molecular transport from an atomic force microscope tip: A comparative study of dip-pen nanolithography, *Langmuir*, 18 (2002) 4041-4046.
- [26] P. E. Sheehan and L. J. Whitman, Thiol diffusion and the role of humidity in "dip pen nanolithography", *Physical Review Letters*, 88 (2002)
- [27] S. Rozhok, R. Piner and C. A. Mirkin, Dip-pen nanolithography: What controls ink transport?, *Journal of Physical Chemistry B*, 107 (2003) 751-757.
- [28] D. Bullen, X. F. Wang, J. Zou, S. W. Chung, C. A. Mirkin and C. Liu, Design, fabrication, and characterization of thermally actuated probe Arrays for dip pen nanolithography, *Journal of Microelectromechanical Systems*, 13 (2004) 594-602.
- [29] D. Bullen, S. W. Chung, X. F. Wang, J. Zou, C. A. Mirkin and C. Liu, Parallel dip-pen nanolithography with arrays of individually addressable cantilevers, *Applied Physics Letters*, 84 (2004) 789-791.
- [30] M. Zhang, D. Bullen, S. W. Chung, S. Hong, K. S. Ryu, Z. F. Fan, C. A. Mirkin and C. Liu, A MEMS nanoplotter with high-density parallel dip-pen nanolithography probe arrays, *Nanotechnology*, 13 (2002) 212-217.
- [31] D. W. Lee, M. Despont, U. Drechsler, C. Gerber, P. Vettiger, A. Wetzel, R. Bennewitz and E. Meyer, Switchable cantilever fabrication for a novel time-of-flight scanning force microscope, *Microelectronic Engineering*, 67-68 (2003) 635-643.
- [32] D. Lee, A. Wetzel, R. Bennewitz, E. Meyer, M. Despont, P. Vettiger and C. Gerber, Switchable cantilever for a time-of-flight scanning force microscope, *Applied Physics Letters*, 84 (2004) 1558-1560.
- [33] N. V. Lavrik, M. J. Sepaniak and P. G. Datskos, Cantilever transducers as a platform for chemical and biological sensors, *Review of Scientific Instruments*, 75 (2004) 2229-2253.
- [34] A. Hierlemann, D. Lange, C. Hagleitner, N. Kerness, A. Koll, O. Brand and H. Baltes, Application-specific sensor systems based on CMOS chemical microsensors, *Sensors and Actuators B*, 70 (2000) 2-11.

- [35] A. Hammiche, D. J. Hourston, H. M. Pollock, M. Reading and M. Song, Scanning thermal microscopy: subsurface imaging, thermal mapping of polymer blends, and localized calorimetry, *Journal of Vacuum Science and Technology B*, 14 (1996) 1486-1491.
- [36] M. Nonnenmacher and H. K. Wickramasinghe, Scanning probe microscopy of thermal conductivity and subsurface properties, *Applied Physics Letters*, 61 (1992) 168-170.
- [37] C. Blanco, S. P. Appleyard and B. Rand, Study of carbon fibres and carbon-carbon composites by scanning thermal microscopy, *Journal of Microscopy*, 205 (2002) 21-32.
- [38] J.-H. Lee and Y. B. Gianchandani, High-resolution scanning thermal probe with servocontrolled interface circuit for microcalorimetry and other applications, *Review of Scientific Instruments*, 75 (2004) 1222-1227.
- [39] L. Harding, J. Wood, M. Reading and D. Q. M. Craig, Two- and three-dimensional imaging of multicomponent systems using scanning thermal microscopy and localized thermomechanical analysis, *Anal. Chem.*, 79 (2007) 129-139.
- [40] E. Oesterschulze and M. Stopka, Imaging of thermal properties and topography by combined scanning thermal and scanning tunneling microscopy, *Microelectronic Engineering*, 31 (1996) 241-248.
- [41] J. Varesi and A. Majumdar, Scanning Joule expansion microscopy at nanometer scales, *Applied Physics Letters*, 72 (1998) 37-39.
- [42] A. Majumdar, Scanning thermal microscopy, *Annual Review of Materials Science*, 29 (1999) 505-585.
- [43] S. Gomes, N. Thannoy, P. Grossel, F. Depasse, C. Bainier and D. Charraut, D.C. scanning thermal microscopy: characterisation and interpretation of the measurement, *International Journal of Thermal Sciences*, 40 (2001) 949-958.
- [44] S. Lefevre, S. Volz, J.-B. Saulnier and C. Fuentes, Thermal conductivity calibration for hot wire based dc scanning thermal microscopy, *Review of Scientific Instruments*, 74 (2003) 2418-2423.

- [45] F. Depasse, P. Grossel and S. Gomes, Theoretical investigations of dc and ac heat diffusion for submicroscopies and nanoscopies, *Journal of Physics D: Applied Physics*, 36 (2003) 204-210.
- [46] C. C. Williams and H. K. Wickramasinghe, Scanning Thermal Profiler, *Applied Physics Letters*, 49 (1986) 1587-1589.
- [47] M. I. Lutwyche, M. Despont, U. Drechsler, U. Durig, W. Haberle, H. Rothuizen, R. Stutz, R. Widmer, G. K. Binnig and P. Vettiger, Highly parallel data storage system based on scanning probe arrays, *Applied Physics Letters*, 77 (2000) 3299-3301.
- [48] W. P. King, T. W. Kenny and K. E. Goodson, Comparison of thermal and piezoresistive sensing approaches for atomic force microscopy topography measurements, *Applied Physics Letters*, 85 (2004) 2086-2088.
- [49] W. P. King, T. W. Kenny, K. E. Goodson, G. Cross, M. Despont, U. Durig, H. Rothuizen, G. K. Binnig and P. Vettiger, Atomic force microscope cantilevers for combined thermomechanical data writing and reading, *Applied Physics Letters*, 78 (2001) 1300-1302.
- [50] W. P. King, T. W. Kenny, K. E. Goodson, G. L. W. Cross, M. Despont, U. T. Durig, H. Rothuizen, G. Binnig and P. Vettiger, Design of atomic force microscope cantilevers for combined thermomechanical writing and thermal reading in array operation, *Journal of Microelectromechanical Systems*, 11 (2002) 765-774.
- [51] J. J. M. Ruigrok, R. Coehoorn, S. R. Cumpson and H. W. Kesteren, Disk recording beyond 100 Gb/in.²: Hybrid Recording?, *Journal of Applied Physics*, 87 (2000) 5389-5403.
- [52] C. R. K. Marrian and D. M. Tennet, Nanofabrication, *Journal of Vacuum Science and Technology A*, 21 (2003) S207-S215.
- [53] E. S. Snow and P. M. Campbell, Afm Fabrication of Sub-10-Nanometer Metal-Oxide Devices with in-Situ Control of Electrical-Properties, *Science*, 270 (1995) 1639-1641.
- [54] E. B. Cooper, S. R. Manalis, H. Fang, H. Dai, K. Matsumoto, S. C. Minne, T. Hunt and C. F. Quate, Terabit-per-square-inch data storage with the atomic force microscope, *Applied Physics Letters*, 75 (1999) 3566-3568.

- [55] K. Wilder, C. Quate, D. Adderton, R. Bernstein and V. Elings, Noncontact nanolithography using the atomic force microscope, *Applied Physics Letters*, 73 (1998) 2527-2529.
- [56] D. M. Eigler and E. K. Schweizer, Positioning Single Atoms with a Scanning Tunneling Microscope, *Nature*, 344 (1990) 524-526.
- [57] H. J. Mamin and D. Rugar, Thermomechanical Writing with an Atomic Force Microscope Tip, *Applied Physics Letters*, 61 (1992) 1003-1005.
- [58] R. P. Ried, H. J. Mamin, B. D. Terris, L. S. Fan and D. Rugar, 6-MHz 2-N/m piezoresistive atomic-force-microscope cantilevers with INCISIVE tips, *Journal of Microelectromechanical Systems*, 6 (1997) 294-302.
- [59] S. Hoen, H. J. Mamin and D. Rugar, Thermomechanical Data-Storage Using a Fiber Optic Stylus, *Applied Physics Letters*, 64 (1994) 267-268.
- [60] N. Abedinov, P. Grabiec, T. Gotszalk, T. Ivanov, J. Voigt and I. W. Rangelow, Micromachined piezoresistive cantilever array with integrated resistive microheater for calorimetry and mass detection, *Journal of Vacuum Science & Technology a-Vacuum Surfaces and Films*, 19 (2001) 2884-2888.
- [61] C. S. Lee, H. J. Nam, Y. S. Kim, W. H. Jin, S. M. Cho and J. U. Bu, Microcantilevers integrated with heaters and piezoelectric detectors for nano data-storage application, *Applied Physics Letters*, 83 (2003) 4839-4841.
- [62] Z. X. Yang, X. X. Li, Y. L. Wang, H. F. Bao and M. Liu, Micro cantilever probe array integrated with Piezoresistive sensor, *Microelectronics Journal*, 35 (2004) 479-483.
- [63] U. Drechsler, N. Burer, M. Despont, U. Durig, B. Gotsmann, F. Robin and P. Vettiger, Cantilevers with nano-heaters for thermomechanical storage application, *Microelectronic Engineering*, 67-8 (2003) 397-404.
- [64] A. Pantazi, M. A. Lantz, G. Cherubini, H. Pozidis and E. Eleftheriou, A servomechanism for a micro-electro-mechanical-system-based scanning-probe data storage device, *Nanotechnology*, 15 (2004) S612-S621.
- [65] P. Vettiger, J. Brugger, M. Despont, U. Drechsler, U. Durig, W. Haberle, M. Lutwyche, H. Rothuizen, R. Stutz, R. Widmer and G. Binnig, Ultrahigh density, high-

data-rate NEMS-based AFM data storage system, *Microelectronic Engineering*, 46 (1999) 11-17.

[66] M. Despont, J. Brugger, U. Drechsler, U. Dürig, W. Häberle, M. Lutwyche, H. Rothuizen, R. Stutz, R. Widmer, H. Rohrer, G. K. Binnig and P. Vettiger, VLSI-NEMS Chip for Parallel AFM Data Storage, *Sensors and Actuators A*, 80 (2000) 100-107.

[67] P. Vettiger, M. Despont, U. Drechsler, U. Durig, W. Haberle, M. I. Lutwyche, H. E. Rothuizen, R. Stutz, R. Widmer and G. K. Binnig, The "Millipede" - More than one thousand tips for future AFM data storage, *Ibm Journal of Research and Development*, 44 (2000) 323-340.

[68] E. Eleftheriou, T. Antonakopoulos, G. K. Binnig, G. Cherubini, M. Despont, A. Dholakia, U. Durig, M. A. Lantz, H. Pozidis, H. E. Rothuizen and P. Vettiger, Millipede - A MEMS-based scanning-probe data-storage system, *Ieee Transactions on Magnetics*, 39 (2003) 938-945.

[69] M. A. Lantz, B. Gotsmann, U. T. Durig, P. Vettiger, Y. Nakayama, T. Shimizu and H. Tokumoto, Carbon nanotube tips for thermomechanical data storage, *Applied Physics Letters*, 83 (2003) 1266-1268.

[70] B. Gotsmann and U. Durig, Thermally activated nanowear modes of a polymer surface induced by a heated tip, *Langmuir*, 20 (2004) 1495-1500.

[71] M. Despont, U. Drechsler, R. Yu, H. B. Pogge and P. Vettiger, Wafer-scale microdevice transfer/interconnect: Its application in an AFM-based data-storage system, *Journal of Microelectromechanical Systems*, 13 (2004) 895-901.

[72] P. Vettiger and G. Binnig, The nanodrive project, *Scientific American*, 288 (2003) 46-53.

[73] A. Chimmalgi, T. Y. Choi, C. P. Grigoropoulos and K. Komvopoulos, Femtosecond laser aperturless near-field nanomachining of metals assisted by scanning probe microscopy, *Applied Physics Letters*, 82 (2003) 1146-1148.

[74] C. Vasilev, H. Heinzelmann and G. Reiter, Controlled melting of individual, nano-meter-sized, polymer crystals confined in a block copolymer mesostructure, *Journal of Polymer Science: Part B: Polymer Physics*, 42 (2004) 1312-1320.

- [75] A. S. Basu, S. McNamara and Y. B. Gianchandani, Scanning thermal lithography: Maskless, submicron thermochemical patterning of photoresist by ultracompliant probes, *Journal of Vacuum Science & Technology B*, 22 (2004) 3217-3220.
- [76] R. Hassler and E. zur Muhlen, An introduction to mu TA (TM) and its application to the study of interfaces, *Thermochim. Acta*, 361 (2000) 113-120.
- [77] M. S. Tillman, B. S. Hayes and J. C. Seferis, Examination of interphase thermal property variance in glass fiber composites, *Thermochim. Acta*, 392 (2002) 299-302.
- [78] C. Blanco, S. Lu, S. P. Appleyard and B. Rand, The stabilisation of carbon fibres studied by micro-thermal analysis, *Carbon*, 41 (2003) 165-171.
- [79] D. S. Fryer, P. F. Nealey and J. J. de Pablo, Thermal probe measurements of the glass transition temperature for ultrathin polymer films as a function of thickness, *Macromolecules*, 33 (2000) 6439-6447.
- [80] A. Hammiche, M. Reading, H. M. Pollock, M. Song and D. J. Hourston, Localized thermal analysis using a miniaturized resistive probe, *Review of Scientific Instruments*, 67 (1996) 4268-4273.
- [81] V. V. Tsukruk, V. V. Gorbunov and N. Fuchigami, Microthermal analysis of polymeric materials, *Thermochim. Acta*, 395 (2003) 151-158.
- [82] M. Galop, Study of pharmaceutical solid dispersions by microthermal analysis, *Pharm. Res.*, 22 (2005) 293-302.
- [83] R. Berger, C. Gerber, J. Gimzewski, E. Meyer and H. Guntherodt, Thermal analysis using a micromechanical calorimeter, *Applied Physics Letters*, 69 (1996) 40-42.
- [84] Y. Nakagawa, R. Schafer and H.-J. Guntherodt, Picojoule and submillisecond calorimetry with micromechanical probes, *Applied Physics Letters*, 73 (1998) 2296-2298.
- [85] L. A. Pinnaduwege, A. Wig, D. L. Hedden, A. Gehl, D. Yi, T. Thundat and R. T. Lareau, Detection of trinitrotoluene via deflagration on a microcantilever, *Journal of Applied Physics*, 95 (2004) 5871-5875.

- [86] L. A. Pinnaduwege, T. Thundat, A. Gehl, S. D. Wilson, D. L. Hedden and R. T. Lareau, Desorption characteristics of uncoated silicon microcantilever surfaces for explosive and common nonexplosive vapors, *Ultramicroscopy*, 100 (2004) 211-216.
- [87] J.-H. Fabian, L. Scandella, H. Fuhrmann, R. Berger, T. Mezzacasa, C. Musil, J. Gobrecht and E. Meyer, Finite element calculation and fabrication of cantilever sensors for nanoscale detection, *Ultramicroscopy*, 82 (2000) 69-77.
- [88] T. Arai and M. Tomitori, Interaction measurements between a tip and a sample in proximity regions controlled by tunneling current in a UHV STM-AFM, *Applied Surface Science*, 144-145 (1999) 501-504.
- [89] M. Tomitori and T. Arai, Tip cleaning and sharpening processes for noncontact atomic force microscope in ultrahigh vacuum, *Applied Surface Science*, 140 (1999) 432-438.

CHAPTER 3

TEMPERATURE CALIBRATION OF HEATED SILICON ATOMIC FORCE MICROSCOPE CANTILEVERS

This chapter presents calibration techniques for heated silicon atomic force microscope cantilevers and analyzes the accuracy of these techniques. A calibration methodology using Raman thermometry is presented and validated with heat transfer simulations and experimental measurements. Raman thermometry generates a calibration standard against which to compare other techniques. Theoretical predictions of the cantilever temperature-dependent electrical properties do not by themselves provide accurate cantilever temperature calibration. Isothermal calibration is also insufficient. The temperature calibrations are stable with storage time and number of heating cycles, although an electrical ‘burn-in’ period is required to stabilize the cantilever electrical response. These techniques for precise temperature calibration of heatable silicon cantilevers are required for applications where temperature must be carefully controlled, including surface science measurements and nano-manufacturing.

3.1 Introduction

Atomic force microscope (AFM) cantilevers with integrated heaters have been used for a number of applications, including thermomechanical actuation [1-3], spatially-resolved substrate topography and thermal property measurements [4-9], nanolithography [10-12], data storage [13], and calorimetry [14-19]. The three primary cantilever designs

that emerged for applications using the tip as a localized heat source were described in section 2.1. The first two designs use metal resistive heaters, where the probe is made of either Wollaston wire [20] or a microfabricated wire encased in polyimide [21]. The third heated probe type is made from doped single-crystal silicon [22] and can reach temperature exceeding 1000 °C [23, 24], be used in parallel [25], and have tips with radius of curvature below 20 nm [13, 22, 23, 26].

Silicon heated cantilevers were originally developed for thermomechanical data storage [13, 22, 26, 27], but have since been used in a number of additional applications that take advantage of their tip sharpness, low cost, and parallelizability. Heated silicon cantilevers were used for controllable AFM-based nanolithography where heat modulated the deposition of a meltable tip coating [11, 12]. Nanolithography was also performed using localized heat delivery to induce chemical changes in a substrate [10, 28]. Heated silicon cantilevers have been used for spatially-resolved calorimetry by characterizing phase transition temperatures on polymers and crystalline organic solids, where the spatial resolution and sampling volume was of size 10-100 nm [15, 17, 29]. Other uses of heated silicon cantilevers have included examining effects of wear on polymer substrates [30], mapping thermal properties of biological samples [7], thermal topography detection [9], and measuring gas thermophysical properties [31].

Precise calibration of the cantilever heater temperature (T_H) was not required for the original data storage application since the primary concern was forming data bits rather than measuring temperature-dependent phenomena. Consequently, rough estimates of T_H were sufficient for data storage research. Precise calibration of T_H is however required for situations in which the cantilever is used for thermal manufacturing

or for making temperature-dependent force and property measurements. For the Wollaston and polyimide heated probes, temperature calibration used a combination of isothermal heating, organic crystal melting standards, and linearity of heater resistance with temperature [32, 33]. In contrast, the silicon probe resistance (R_p) varies non-linearly with temperature and significant temperature gradients exist in the cantilever, making calibration of T_H less straightforward. This chapter presents a systematic analysis of experimental methods for calibrating T_H of heated silicon cantilevers.

3.2 Background

The heated silicon cantilevers characterized in this chapter were made of doped single crystal silicon, similar to those developed for data storage [8, 13, 27, 34]. The fabrication process has been described elsewhere [23]. The cantilevers used were similar to that shown in the microscope images of Figure 1.2. The 100 μm long legs of the ‘U’-shaped cantilevers were phosphorous doped to $1 \times 10^{20} \text{ cm}^{-3}$ and were highly conductive, while the bridge was low-doped to $1 \times 10^{17} \text{ cm}^{-3}$, creating a resistive heating element in the current path. The low-doped heater accounted for about 90% of R_p , and thus most of the heating power (P_{heat}) was dissipated in the heater. The thickness of the cantilever was measured by SEM to be 600 nm, with a tip height near 1.5 μm and radius of curvature below 20 nm.

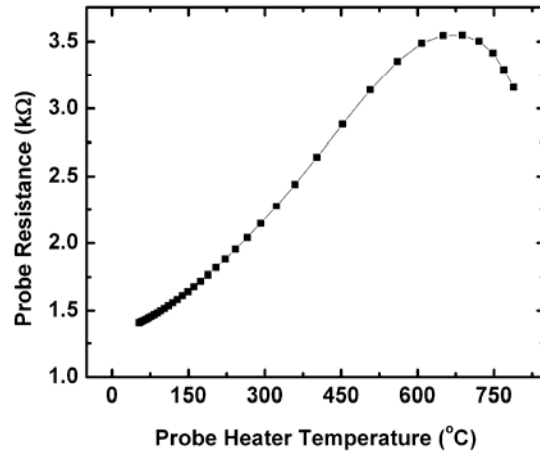


Figure 3.1 Typical variation in cantilever resistance as a function of the temperature at the heater end of the cantilever. Competition between increased electron scattering and carrier generation at elevated temperatures results in a peak in the resistance at the ‘intrinsic temperature’.

The electrical resistivity of the doped-silicon cantilever is a strong function of temperature. Figure 3.1 shows the variation of R_p with T_H . The cantilever had a room temperature resistance near 1.4 kΩ, which increased with temperature to a peak resistance near 3.5 kΩ at 3 mW of heating power and 650 °C. The increase in R_p with temperature below 650 °C was caused by decreasing electrical carrier mobility due to increased scattering of the electrical carriers off lattice vibrations in the silicon. Above 650 °C, R_p began to decrease with temperature due to thermal excitation of electrons into the conduction band of the silicon. The temperature at which R_p peaks is referred to as the intrinsic temperature (T_{int}), where thermally-generated intrinsic carriers dominate the background carriers from the dopants. The thermal runaway behavior at temperatures above T_{int} is well understood and described elsewhere [35].

Because the electrical resistivity of the cantilever is a function of temperature, T_H can be determined from R_p once the temperature-dependence of R_p has been calibrated.

Previous research used a single calibration point to calibrate R_p by estimating T_{int} theoretically and then assuming a linear relationship between P_{heat} and T_H [7, 13, 30, 36, 37]. T_H has also been calibrated by measuring R_p while externally heating the entire cantilever to an isothermal temperature [11, 22], and by using external thermometry to measure T_H while the cantilever was self-heated [16, 23].

Optical thermometry is advantageous for measuring T_H because it does not require heat to diffuse from the cantilever into an external sensor [38]. Micro-IR thermometry can measure temperature from the emitted radiation from a sample [39], but the spatial resolution of the IR microscope is diffraction-limited to $\sim 10 \mu\text{m}$, which is similar to the total size of the cantilever heater. IR thermometry is most accurate if the temperature-dependence of the sample emissivity is known over the entire temperature range of interest. Raman spectroscopy has advantages over IR thermometry since it has submicron lateral resolution and does not require calibrating the sample emissivity [40, 41].

3.3 Raman Thermometry Calibration Methodology

Raman spectroscopy can perform thermometry of heated silicon cantilevers [16, 23, 42]. In Raman spectroscopy, the temperature of the illuminated region of the sample can be determined from several aspects of the Raman optical scattering signature: the position of the Stokes peak, the width of the Stokes peak, and the ratio of the Stokes peak to the anti-Stokes peak [40, 42, 43]. The latter two provide absolute measurements of temperature but also require long accumulation times to account for statistical fluctuation

and to resolve the weak anti-Stokes peak. Additionally, the ratio of the Stokes peak to the anti-Stokes peak loses sensitivity to temperature above 500 °C for silicon [43]. The Stokes peak position can be measured quickly and accurately but is partially affected by stress within the sample [42].

The T_H of heated cantilevers was calibrated using a commercial Raman Microscope with a 488 nm laser. The Raman laser was focused on the cantilever heater near the cantilever tip. To prevent the laser from heating the cantilever, the laser was filtered such that the laser power at the sample was only $\sim 10 \mu\text{W}$, which caused a cantilever temperature rise less than 1.5 °C and was negligible in comparison to P_{heat} , which was $\sim 1 \text{ mW}$. The laser did, however, affect the electrical characteristics of the cantilever, generally changing R_p by less than 2%. In a few cases the resistance changed up to 50%, possibly due to laser-induced carrier excitation, and these cantilevers were not considered. For all Raman calibrations reported, P_{heat} refers to the heating power dissipated on the cantilever while the Raman laser was focused on the cantilever.

Raman calibration required first measuring the Raman scattering spectrum of the cantilever at room temperature in order to establish a baseline from which to determine the relative changes in the peak position and width while the cantilever was in active operation. Figure 3.2 shows drift over time in the baseline temperatures calculated from both the Stokes average peak position and average width for an unheated cantilever. The data shown in Figure 3.2 corresponds to the amount of drift that occurred in the Stokes peak before spatial drift of the cantilever was discernable in the microscope. The drift shown in Figure 3.2 occurred after already having allowed ~ 1 hour of settling time in the system, during which time significantly more drift occurred. Returning the cantilever to

its initial position caused the Stokes peak position and width to return to their initial range. The variation in the peak position along the cantilever heater was likely due to variation in internal stresses, while the variation in the peak width likely occurred because the peak width is a measurement of phonon lifetime in the substrate [44], which can be influenced by proximity to the edges of the cantilever. Precise spatial alignment was therefore required between baseline measurements and subsequent temperature measurements while the cantilever was heated in order to eliminate the effects of spatial drift on the relative changes in the Stokes peak width and position. Determining T_H from the Stokes peak width or the Stokes/anti-Stokes peak ratio was particularly impacted by spatial drift because of the long accumulation time required to reduce statistical uncertainties. The drift shown in Figure 3.2 corresponds to the minimum visually discernible misalignment under the microscope, and thus the temperature variation in Figure 3.2 represents a minimum estimate of the uncertainty due to spatial drift between the baseline measurement and subsequent Raman measurements of the heated cantilever.

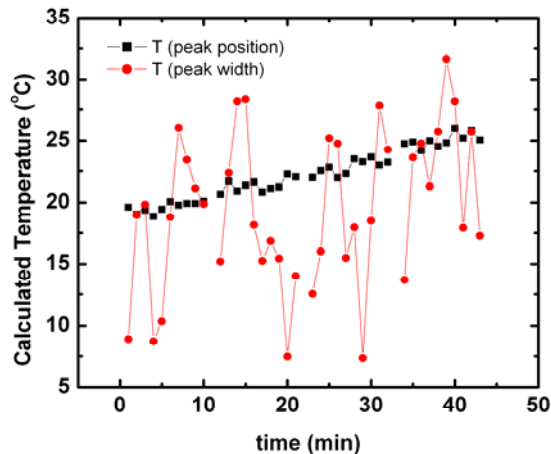


Figure 3.2 Drift in Raman calculated temperature from Stokes peak width and peak position before spatial drift of the cantilever in the microscope became noticeable. Random fluctuations are much smaller in the Stokes peak shift than the peak width.

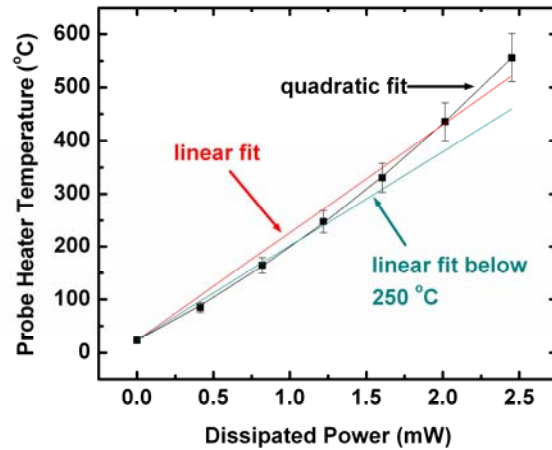


Figure 3.3 Raman-measured heater temperature as a function of total power dissipated on a thermal cantilever. A quadratic polynomial fits the calibration data much better than a linear fit. The primary contribution to the error bar at high temperatures is the effect of intrinsic stress in the cantilever.

Figure 3.3 shows the Raman-measured T_H as a function of P_{heat} , determined from the Stokes peak position. The data were insensitive to the focus position of the laser around the tip as long as the measurements were carefully aligned to the same position as that from the baseline measurement. The error bars at low temperatures are due to potential drift of the laser spot between the baseline calibration and the measurement while the cantilever was self-heated. The error bars at high temperatures are due to the internal stress in the cantilever that results from heating [23] and were less than 10% of the total temperature rise. The uncertainties could be reduced to $\sim 5\%$ of the total temperature rise by using the Stokes peak width for determining T_H , but the higher accuracy comes at the expense of increasing the time required for calibration by a factor of ~ 50 . Considering the tradeoff between experimental time and the effects of spatial drift and thermal stress on measurement accuracy, T_H was optimally calibrated from the Stokes peak position.

3.4 Evaluation of Previous Calibration Methodologies

The thermal calibration using Raman spectroscopy shown in Figure 3.3 was used as a calibration standard against which previously reported thermal calibration techniques could be compared. Quantitative comparison of the calibration techniques was possible because the uncertainty of the Raman calibration was known.

3.4.1 Single Point Calibration

Several previous reports of silicon cantilever temperature calibration assumed that T_{int} could be predicted from theory, and that T_H increased linearly with P_{heat} [7, 13, 30]. Thus calibration was possible from a single point by measuring the required P_{heat} for the cantilever to reach T_{int} . To test the validity of assuming that T_{int} could be predicted from theory, T_{int} was measured for 25 different cantilevers with identical doping concentrations using Raman spectroscopy. The measured values for T_{int} varied from 500-1300 °C, with a mean value of 810 °C and standard deviation of 160 °C. Because the cantilevers came from the same processed silicon wafer, the nearly identical doping concentrations should have yielded consistent values for T_{int} , but this was not true for the cantilevers fabricated by our group. In this particular fabrication process, the variation in cantilever thickness over a wafer can reach 50%, which was likely the cause of the observed variance. In addition to the measured variance in T_{int} , the accuracy of the single point calibration method was further challenged by the non-linear relationship between T_H and P_{heat} shown in Figure 3.3. Above 250 °C, the relationship between T_H and P_{heat} was poorly described by a linear fit, but was well-described by a second-order

fit. The combination of the variability in T_{int} and the non-linearity of the dependence of T_H on P_{heat} could result in errors over 100% in estimating T_H . The cause of non-linearity between T_H and P_{heat} is discussed below.

3.4.2 Isothermal (Hotplate) Calibration

The Raman spectroscopy temperature calibration was also used to assess the accuracy of isothermal calibrations on a hotplate [11, 22]. For this calibration method, the cantilever was placed on a hotplate and its resistance measured at fixed hotplate temperatures. The aluminum contact pads on the cantilever chip limited the maximum calibration temperature to ~ 400 °C, at which the temperature difference between the cantilever and the hotplate was estimated to be less than 5 °C.

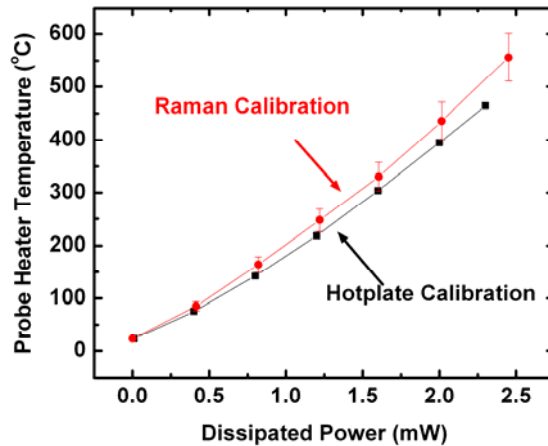


Figure 3.4 Comparison between hotplate and Raman temperature calibrations for a heated cantilever. The hotplate calibration neglects the effect of isothermal cantilever legs, and predicts a lower heater temperature for a given power, incurring an error of ~ 10 -15%.

Figure 3.4 compares the results of the hotplate calibration to the Raman calibration and demonstrates that the hotplate calibration underpredicted T_H by 10-15% for a given P_{heat} . The discrepancy between the two calibrations was caused by the

increased electrical resistance for isothermally heated legs as compared to the self-heated legs, which had a temperature gradient. A temperature drop between the hotplate thermocouple and the cantilever during calibration would overpredict T_H , and thus cannot account for the results in Figure 3.4. Without access to optical thermometry techniques, such as Raman spectroscopy, the 10-15% error of isothermal calibration may be acceptable and gives significant improvement over the potential 100% error of the single point calibration. The accuracy of isothermal calibration increases as the resistance in the cantilever heater becomes a larger portion of R_p . On the other extreme, we tested some cantilevers for which the resistance in the legs constituted $\sim 30\%$ of R_p , and in this case hotplate calibrations underpredicted T_H by $\sim 50\%$.

3.4.3 Melting Standard Calibration

Melting standards had previously been used in thermal calibration of other heated AFM probes [32, 33]. Table 3.1 lists the organic crystal melting standards used in this study, along with their bulk and AFM-measured melting temperatures (T_m). Flat films of the samples were prepared from powdered form by placing the powder on a glass slide, covering the powder with another glass slide to minimize exposure to air, then placing on a hotplate at a temperature ~ 10 °C above the melting temperature of the chemical. Once the powder melted into a film, the slides were removed from the heat and quickly cooled, and the slides were separated. AFM measurements of T_m were made by steadily increasing the temperature of a Raman-calibrated cantilever while the cantilever tip was held in contact with the organic material. Melting was identified by determining the point at which the tip began to penetrate into the melted substrate, which could be

identified both from optical detection of cantilever position and from changes in the thermal impedance between the cantilever and the substrate [14, 45].

Table 3.1 Organic melting standards and their bulk and measured transition temperatures.

Chemical	Bulk Melting Temperature (°C)	AFM Melting Temperature (°C)
Benzophenone	47-51	<23
Octadecylphosphonic Acid	99	67
Pentaerythritol Tetranitrate	144	60
Xylose	150-152	138
Benzoylbenzoic Acid	198-200	100
Sodium Formate	259-262	185

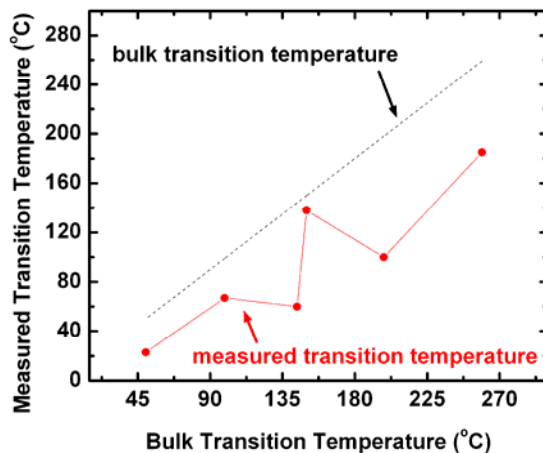


Figure 3.5 The transition temperatures of organic crystals measured by the thermal cantilever are about 30% lower than their bulk transition temperature.

Figure 3.5 shows that the AFM-measured T_m values were lower than the expected bulk T_m of the organic crystals. Depression of the AFM-measured T_m occurred with all organic crystals tested, including several not listed in Table 3.1 or shown in Figure 3.5, and was highly repeatable. The depression in T_m cannot be attributed to calibration error because similar measurements of glass transition temperatures with the same heated

cantilever on polymer samples exhibited the opposite trend, with the AFM-measured glass transition temperature being ~25% higher than the expected bulk value. In the case of polymers, the elevation of the apparent glass transition temperature was attributed to a decrease in temperature between the calibrated T_H and the temperature at the polymer surface due to constricted heat flow through the cantilever tip. The high contact pressure under the tip also cannot explain the depression in the AFM-measured melting temperatures because high pressure should favor the solid phase [46]. We hypothesize that the cause of the depression in the AFM-measured T_m of the organic crystals was nanoscale confinement due to the small contact area underneath the tip [47, 48]. Depression of T_m has already been shown in organic solids confined in nanoscale geometries and also for metal nanoparticles due to the large surface to volume ratio [15, 48, 49]. It is possible that some degradation occurred in the organic materials during film preparation, but the measured depression is also consistent with the reported depression of the AFM-measured decomposition temperature of single crystal and spun-cast pentaerythritol tetranitrate samples [15], data from which is also included in Figure 3.5. Additionally, in the case of benzophenone, which had the lowest bulk T_m at 47 °C, the film was solid to the touch but melted beneath the AFM tip at room temperature. The use of organic melting standards is thus ineffective for temperature calibration of silicon heated cantilevers.

3.5 Validity of Calibration Methodology

The general methodology for calibration of heated silicon cantilevers was to: a) calibrate the dependence of T_H on P_{heat} in air for a given cantilever; b) place the cantilever into the environment in which it would be used and align any necessary optics; c) steadily increase P_{heat} and monitor R_p while holding the cantilever at least 500 μm away from a substrate to ensure elimination of substrate effects on the heat transfer from the cantilever; d) use the calibrated T_H and P_{heat} relationship to correlate R_p to T_H ; e) assume that the relationship between R_p and T_H did not change when the cantilever was brought in contact with a substrate. The assumptions of stable thermal and electrical properties implicit to the described methodology are assessed in this section.

3.5.1 Dependence of T_H on P_{heat}

The non-linearity between P_{heat} and T_H stands in contrast to previous assumptions of linearity [7, 13, 30] but should be expected because the silicon cantilever has a temperature-dependent thermal conductivity [50] and nonzero heat generation in the cantilever legs. To examine the effect of temperature-dependent thermal conductivity, a simple one-dimensional finite difference model of heat flow in the cantilever was developed, incorporating the temperature-dependence of the thermal conductivity of silicon [8, 34, 51, 52]. The model neglected heat generation in the legs, and applied a heater temperature at the end of the legs and a thermal spreading resistance at the base as boundary conditions. The temperature-dependent air thermal conductivity [53] used in determining the heat transfer coefficient was averaged between the

temperatures at the heater and base ends of the cantilever legs. The effective heat transfer coefficient (u_{eff}) using a cylindrical conduction model and experimentally measured boundaries was $\sim 3100 \text{ W/m}^2\text{K}$. The large value for u_{eff} was caused by the small surface area of the cantilever legs and was consistent with other estimates [51, 52]. Natural convection to the air was neglected because heat transfer occurs primarily through conduction at the microscale due to the increased significance of viscous forces [54]. A constant scaling factor (k_{scale}) was used to reduce the bulk thermal conductivity of silicon to account for size and doping effects, which reduce the thermal conductivity without significantly altering the relative temperature dependence above 300 K [55, 56]. The value of k_{scale} was determined from fitting experimental data in simulations described later in this chapter, and was equal to 0.25. Radiation was included in the model, using an emissivity of 0.7 for heavily-doped silicon [57]. The model was validated by checking against analytical solutions, balancing energy, and refining the mesh without incurring changes in the solution.

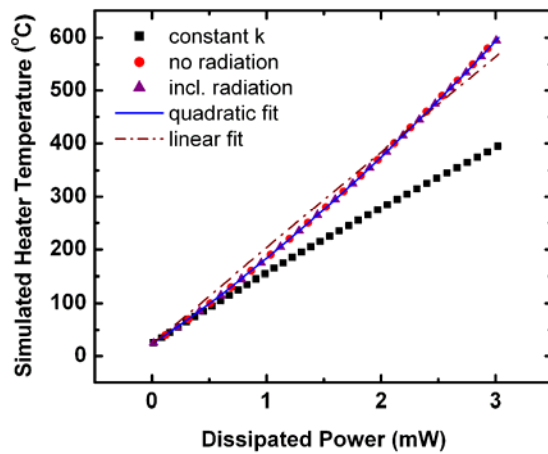


Figure 3.6 Simulated heater temperature for various cantilever powers. The temperature-dependent thermal conductivity of silicon accounts for the roughly quadratic dependence of heater temperature on cantilever power. Simulations with and without radiation demonstrate that radiation plays a negligible in the heat transfer for the temperatures considered.

Figure 3.6 shows the calculated relationship between T_H and P_{heat} . The results are well-described by a quadratic fit, but not well-described by a linear fit. The deviation from linearity increased as the thermal conductivity scaling factor was increased. Inclusion of power dissipation in the legs, where $\sim 10\%$ of P_{heat} is dissipated, would also increase the non-linearity. Less than 0.5% of P_{heat} was transferred through radiation even at 600 °C, and the amount of heat transferred through radiation did not approach 1% of P_{heat} even as T_H approached 1400 °C, the melting temperature of silicon. No attempt was made to fit the results to experimental data since the purpose of this simple model was to demonstrate the effect of temperature-dependent thermal conductivity rather than to provide an exact solution of T_H vs. P_{heat} .

3.5.2 Thermal and Electrical Stability

Repeated thermal and electrical calibrations were performed on the cantilever in order to assess their stability. Figure 3.7 shows the results of separate Raman calibrations of T_H for a cantilever before and after performing several hundred self-heating cycles above 750 °C and twice being heated over 400 °C on a hotplate. The separate calibrations nearly overlapped and were well within the range of uncertainty for the data. The error bars were removed for clarity, but were identical to those in Figure 3.3. The calibrations showed no hysteresis upon cooling and were reproducible over several months of storage and use. The stability of the relationship between T_H and P_{heat} was expected because the relationship should depend on the thermal conductivity and geometry of the cantilever and should thus remain stable even if the electrical properties of the cantilever exhibit small changes with time and use.

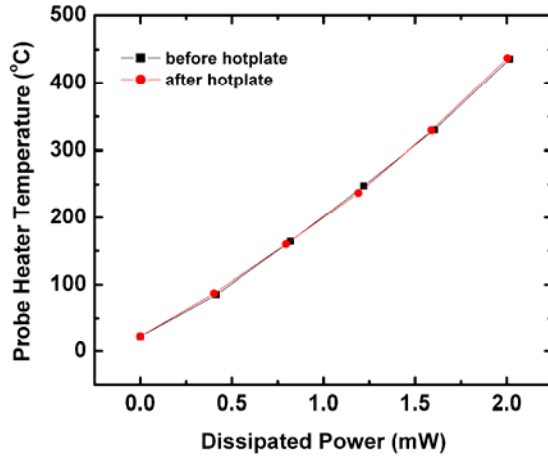


Figure 3.7 Raman-measured heater temperature of a thermal cantilever before and after calibrating on a hotplate, and after several hundred self-heating cycles. No change occurs in the relationship between heater temperature and power. Error bars are removed for clarity, but are the same as in Figure 3.3.

The resistance of heated silicon cantilevers was generally stable below ~ 400 °C, but often required a significant ‘burn-in’ time before the resistance near and above T_{int} stabilized, which generally required several hundred self-heating cycles. Additionally, R_p often changed after the first self-heating cycle when the cantilever had been stored for several days, which Figure 3.8 shows. We hypothesize that the deviation in R_p on the first self-heating cycle was related to Schottky barrier effects in the contacts between the aluminum leads on the cantilever chip and the doped silicon cantilever. The behavior could be reversed and reproduced by switching the polarity of the heating voltage. Because of the deviation in the first self-heating cycle, correlation of R_p to T_H should not be performed until the cantilever has already undergone at least 1 self-heating cycle.

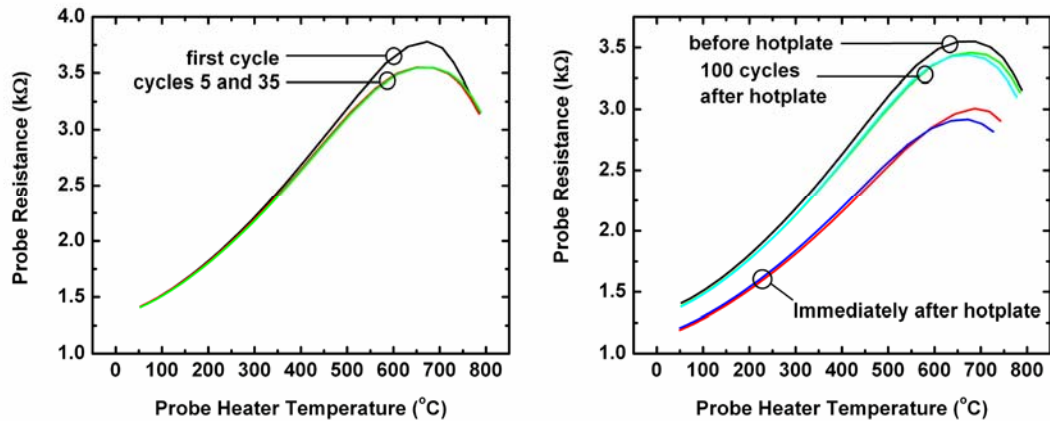


Figure 3.8 Left: comparison of thermal cantilever electrical response after various numbers of electrical cycles. After several days of storage, the first self-heating cycle usually deviates from all subsequent cycles. Negligible variation occurs in the later cycles. Right: the change in electrical behavior of the thermal cantilevers after heating on a hotplate two separate times. The decrease and recovery in resistance is similar for each hotplate calibration. Continuous cycling of the cantilever causes the electrical behavior to eventually re-stabilize to its initial behavior.

Heating the cantilever on a hotplate also induced significant instability in R_p .

Figure 3.8 shows R_p as a function of T_H for a cantilever before and after being heated to 400 °C on a hotplate two separate times. Each time, R_p was significantly reduced after removal from the hotplate, but gradually stabilized to its initial resistance after repeated self-heating cycles. The drift in R_p is likely due to redistribution of dopants after the hotplate annealed the cantilever. The instability incurred in R_p was an important drawback of isothermal temperature calibrations. When performing isothermal temperature calibrations, the relationship between P_{heat} and T_H for a given cantilever had to be determined immediately after calibrating R_p since the drift in R_p made the relationship between R_p and T_H an unreliable calibration for continued use.

3.5.3 Substrate Effect on R_p

Even if the electrical and thermal properties of a cantilever were fully stable, bringing a cantilever into contact with a substrate could induce error in the calibration of R_p vs. T_H . The difference in thermal impedance for a cantilever in contact with a substrate as compared to a cantilever in air causes different temperature distributions along the legs for a given T_H , which could affect R_p . To examine the effect, a finite difference model was developed similar to the model described in section 3.5.1. The model applied a current (I_C) through the cantilever and determined the corresponding temperature at the midpoint of the heater. The model assumed that resistivity was linear with temperature and used separate temperature coefficients of resistivity for the legs and the heater. The simulations were performed over a range of temperatures for which R_p was measured to be linear during isothermal heating. The temperature coefficient of the total cantilever resistance was experimentally determined from the hotplate calibrations, and thus the separate temperature coefficients of resistivity for the legs and heater constituted only a single unknown parameter. The simulations were fit to experimental measurements of R_p , P_{heat} , T_H , and I_C for a cantilever operated in air. The temperature coefficient of resistivity of the legs and k_{scale} were used as fitting parameters. The fitting resulted in a k_{scale} value of .25, which was lower than the expected value of $\sim .4$ [56], but was reasonable.

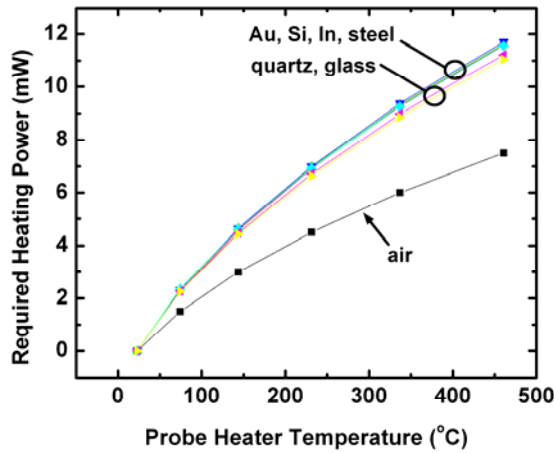


Figure 3.9 Measurements of required heating power as a function of cantilever heater temperature with the cantilever in contact with various substrates. Substrate thermal conductivity has no effect above 14 W/m²K, and only a slight effect below 6 W/m²K.

The simulation was repeated with the cantilever tip in contact with a substrate. Conduction to the substrate was accounted for by a thermal spreading resistance for an infinite rectangular channel in a semi-infinite solid. The temperature of the substrate was assumed to be equal to ambient temperature since the thermal resistance to heat conduction through the air gap was much larger than the thermal resistance to heat conduction through the substrate. Figure 3.9 shows P_{heat} plotted against T_H for several substrates spanning 2.5 orders of magnitude in thermal conductivity. The substrate thermal conductivity had no effect on the required heating power for substrate thermal conductivities over 14 W/m²K, while having only a slight effect for substrate thermal conductivities near 1 W/m²K. The weak effect of the substrate thermal properties on the required heating power implies that the temperature rise in the substrate below the cantilever legs was small or negligible, supporting the assumption in the model that the substrate temperature was equal to the ambient temperature.

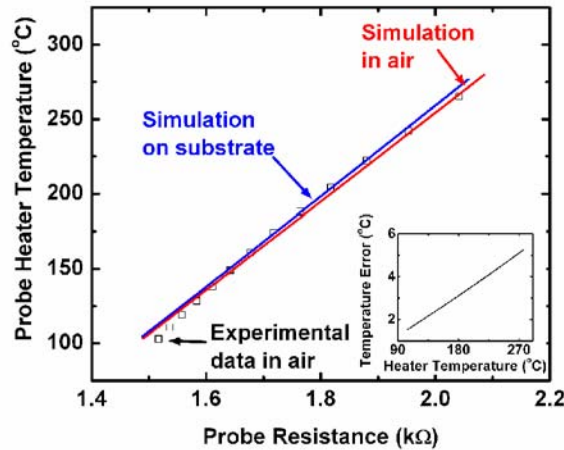


Figure 3.10 Simulated heater temperature as a function of resistance with the cantilever in air and in contact with a substrate. The inset shows the corresponding temperature error by assuming no change in the relationship between cantilever resistance and heater temperature. The temperature error is $\sim 2\%$ for heater temperatures below $300\text{ }^{\circ}\text{C}$.

Figure 3.10 shows the results of the simulated R_p variation with T_H for a cantilever in air and a cantilever on a substrate, along with experimental data for the cantilever in air. The difference in T_H for a given cantilever resistance was $\sim 2\%$, which was smaller than the uncertainty of the Raman calibration and thus made a negligible contribution to the uncertainty in determining T_H during cantilever operation with the tip in contact with a substrate.

3.6 Conclusions

This chapter analyzes several methods of calibrating heated silicon cantilevers. Thermometry of the cantilevers using Raman spectroscopy and the Stokes peak position is a fast and accurate technique for calibrating T_H , but the technique demands care to control spatial drift, and has increased uncertainty at high temperatures due to the effects of thermally-induced stress in the cantilevers. Without access to Raman spectroscopy or

other optical thermometry methods, isothermal calibration can estimate T_H within 10-15%, but re-stabilizing R_p after calibration requires repeated self-heating cycles. The thermal properties of the cantilevers are stable with time and thermal cycling, while the electrical properties require a ‘burn-in’ period and only became stable after repeated self-heating cycles. Although this chapter describes calibration methods for determining T_H , often the temperature at the tip-substrate interface is of interest and cannot generally be assumed to be equal to T_H because of constriction of heat flow through the tip and into the substrate.

3.7 References

- [1] W. Franks, D. Lange, S. Lee, A. Hierlemann, N. Spencer and H. Baltes, Nanochemical surface analyzer in CMOS technology, *Ultramicroscopy*, 91 (2002) 21-27.

- [2] T. Sulchek, S. C. Minne, J. D. Adams, D. A. Fletcher, A. Atalar, C. F. Quate and D. M. Adderton, Dual integrated actuators for extended range high speed atomic force microscopy, *Applied Physics Letters*, 75 (1999) 1637-1639.

- [3] X. Wang, D. A. Bullen, J. Zou, C. Liu and C. Mirkin, Thermally actuated probe array for parallel dip-pen nanolithography, *Journal of Vacuum Science and Technology B*, 22 (2004) 2563-2567.

- [4] A. Hammiche, D. J. Hourston, H. M. Pollock, M. Reading and M. Song, Scanning thermal microscopy: subsurface imaging, thermal mapping of polymer blends, and localized calorimetry, *J. Vac. Sci. Technol., B*, 14 (1996) 1486-1491.

- [5] M. Nonnenmacher and H. K. Wickramasinghe, Scanning probe microscopy of thermal conductivity and subsurface properties, *Appl. Phys. Lett.*, 61 (1992) 168-170.

- [6] M.-H. Li and Y. B. Gianchandani, Applications of a low contact force polyimide shank bolometer probe for chemical and biological diagnostics, *Sens. Actuators, A*, 104 (2003) 236-245.

- [7] W. Haeblerle, M. Pantea and J. K. H. Hoerber, Nanometer-scale heat-conductivity measurements on biological samples, *Ultramicroscopy*, 106 (2006) 678-686.
- [8] W. P. King, T. W. Kenny, K. E. Goodson, G. Cross, M. Despont, U. Durig, H. Rothuizen, G. K. Binnig and P. Vettiger, Atomic force microscope cantilevers for combined thermomechanical data writing and reading, *Appl. Phys. Lett.*, 78 (2001) 1300-1302.
- [9] W. P. King, T. W. Kenny and K. E. Goodson, Comparison of thermal and piezoresistive sensing approaches for atomic force microscopy topography measurements, *Appl. Phys. Lett.*, 85 (2004) 2086-2088.
- [10] S. Bakbak, P. J. Leech, B. E. Carson, S. Saxena, W. P. King and U. H. F. Bunz, 1,3-dipolar cycloaddition for the generation of nanostructured semiconductors by heated probe tips, *Macromolecules*, 39 (2006) 6793-6795.
- [11] P. E. Sheehan, L. J. Whitman, W. P. King and B. A. Nelson, Nanoscale deposition of solid inks via thermal dip pen nanolithography, *Appl. Phys. Lett.*, 85 (2004) 1589-1591.
- [12] M. Yang, P. E. Sheehan, W. P. King and L. J. Whitman, Direct writing of a conducting polymer with molecular-level control of physical dimensions and orientation, *J. Am. Chem. Soc.*, 128 (2006) 6774-6775.
- [13] P. Vettiger, G. Cross, M. Despont, U. Drechsler, U. Durig, B. Gotsman, W. Haeblerle, M. Lantz, H. Rothuizen, R. Stutz and G. Binnig, The "millipede" - nanotechnology entering data storage, *IEEE Trans. Nanotechnology*, 1 (2002) 39-55.
- [14] A. Hammiche, M. Reading, H. M. Pollock, M. Song and D. J. Hourston, Localized thermal analysis using a miniaturized resistive probe, *Rev. Sci. Inst.*, 67 (1996) 4268-4273.
- [15] W. P. King, S. Saxena, B. A. Nelson, R. Pitchimani and B. L. Weeks, Nanoscale Thermal Analysis of an Energetic Material, *Nano Lett.*, 6 (2006) 2145-2149.
- [16] B. A. Nelson and W. P. King, Measuring material softening with nanoscale spatial resolution using heated silicon probes, *Rev. Sci. Inst.*, 78 (2007) 023702.

- [17] L. A. Pinnaduwaige, A. Wig, D. L. Hedden, A. Gehl, D. Yi, T. Thundat and R. T. Lareau, Detection of trinitrotoluene via deflagration on a microcantilever, *J. Appl. Phys.*, 95 (2004) 5871-5875.
- [18] R. Berger, H. Lang, C. Gerber, J. Gimzewski, J. Fabian, L. Scandella, E. Meyer and H. Guntherodt, Micromechanical thermogravimetry, *Chem. Phys. Lett.*, 294 (1998) 363-369.
- [19] J. Lee and W. P. King, Microcantilever hotplates: design, fabrication, and characterization, *Sensors and Actuators a-Physical*, (2006 - in press)
- [20] R. J. Pylkki, P. J. Moyer and P. E. West, Scanning near-field optical microscopy and scanning thermal microscopy, *Jpn. J. Appl. Phys.*, 33 (1994) 3785-3790.
- [21] M. H. Li, J. J. Wu and Y. B. Gianchandani, Surface micromachined polyimide scanning thermocouple probes, *J. Microelectromech. Syst.*, 10 (2001) 3-9.
- [22] B. W. Chui, T. D. Stowe, Y. S. Ju, K. E. Goodson, T. W. Kenny, H. J. Mamin, B. D. Terris, R. P. Ried and D. Rugar, Low-stiffness silicon cantilevers with integrated heaters and piezoresistive sensors for high-density AFM thermomechanical data storage, *J. Microelectromech. Syst.*, 7 (1998) 69-78.
- [23] J. Lee, T. Beechem, T. L. Wright, B. A. Nelson, S. Graham and W. P. King, Electrical, Thermal, and Mechanical Characterization of Silicon Microcantilever-Heaters, *J. Microelectromech. Syst.*, 15 (2006 - in press) 1644-1655.
- [24] E. O. Sunden, T. L. Wright, J. Lee, W. P. King and S. Graham, Room-temperature chemical vapor deposition and mass detection on a heated atomic force microscope cantilever, *Appl. Phys. Lett.*, 88 (2006) 033107.
- [25] M. Lutwyche, C. Andreoli, G. Binnig, J. Brugger, U. Drechsler, W. Haberle, H. Rohrer, H. Rothuizen, P. Vettiger, G. Yaralioglu and C. Quate, 5X5 2D AFM cantilever arrays a first step towards a Terabit storage device, *Sensors and Actuators a-Physical*, 73 (1999) 89-94.
- [26] M. Despont, J. Brugger, U. Drechsler, U. Dürig, W. Häberle, M. Lutwyche, H. Rothuizen, R. Stutz, R. Widmer, H. Rohrer, G. K. Binnig and P. Vettiger, VLSI-NEMS Chip for Parallel AFM Data Storage, *Sens. Actuators, A*, 80 (2000) 100-107.

- [27] G. Binnig, M. Despont, U. Drechsler, W. Haberle, M. Lutwyche, P. Vettiger, H. J. Mamin, B. W. Chui and T. W. Kenny, Ultrahigh-density atomic force microscopy data storage with erase capability, *Appl. Phys. Lett.*, 74 (1999) 1329-1331.
- [28] B. Gotsmann, U. Duerig, J. Frommer and C. J. Hawker, Exploiting chemical switching in a Diels-Alder polymer for nanoscale probe lithography and data storage, *Adv. Func. Mat.*, 16 (2006) 1499-1505.
- [29] B. A. Nelson and W. P. King, Measuring material softening with nanoscale spatial resolution using heated silicon probes, *Rev. Sci. Inst.*, (2006 - accepted)
- [30] B. Gotsmann and U. Durig, Thermally activated nanowear modes of a polymer surface induced by a heated tip, *Langmuir*, 20 (2004) 1495-1500.
- [31] B. Gotsmann and U. Durig, Experimental observation of attractive and repulsive thermal forces on microcantilevers, *Appl. Phys. Lett.*, 87 (2005) 194102.
- [32] J.-H. Lee and Y. B. Gianchandani, High-resolution scanning thermal probe with servocontrolled interface circuit for microcalorimetry and other applications, *Rev. Sci. Inst.*, 75 (2004) 1222-1227.
- [33] D. S. Fryer, P. F. Nealey and J. J. de Pablo, Thermal probe measurements of the glass transition temperature for ultrathin polymer films as a function of thickness, *Macromolecules*, 33 (2000) 6439-6447.
- [34] W. P. King, T. W. Kenny, K. E. Goodson, G. L. W. Cross, M. Despont, U. T. Durig, H. Rothuizen, G. Binnig and P. Vettiger, Design of atomic force microscope cantilevers for combined thermomechanical writing and thermal reading in array operation, *J. Microelectromech. Syst.*, 11 (2002) 765-774.
- [35] B. W. Chui, M. Asheghi, Y. S. Ju, K. E. Goodson, T. W. Kenny and H. J. Mamin, Intrinsic-carrier thermal runaway in silicon microcantilevers, *Microscale Thermophysical Engineering*, 3 (1999) 217-228.
- [36] U. Durig, Fundamentals of micromechanical thermoelectric sensors, *J. Appl. Phys.*, 98 (2005)

- [37] M. A. Lantz, B. Gotsmann, U. T. Durig, P. Vettiger, Y. Nakayama, T. Shimizu and H. Tokumoto, Carbon nanotube tips for thermomechanical data storage, *Appl. Phys. Lett.*, 83 (2003) 1266-1268.
- [38] Z. M. Zhang, Surface temperature measurements using optical techniques, *Annual Review of Heat Transfer*, 11 (2000) 351-411.
- [39] J. Kolzer, E. Oesterschulze and G. Deboy, Thermal imaging and measurement techniques for electronic materials and devices, *Microelectron. Eng.*, 31 (1996) 251-270.
- [40] J. R. Serrano, L. M. Phinney and S. P. Kearney, Micro-Raman thermometry of thermal flexure actuators, *Journal of Micromechanics and Microengineering*, 16 (2006) 1128-1134.
- [41] B. McCarthy, Y. M. Zhao, R. Grover and D. Sarid, Enhanced Raman scattering for temperature measurement of a laser-heated atomic force microscope tip, *Appl. Phys. Lett.*, 86 (2005)
- [42] M. R. Abel, T. L. Wright, E. O. Sunden, S. Graham, W. P. King and M. J. Lance, *Thermal metrology of silicon microstructures using Raman spectroscopy*, *Twenty First Annual IEEE Semiconductor Thermal Measurement and Management Symposium, San Jose, CA, 2005*, pp. 235-242.
- [43] M. Ivanda, Raman-Scattering Measurements and Fracton Interpretation of Vibrational Properties of Amorphous-Silicon, *Physical Review B*, 46 (1992) 14893-14896.
- [44] P. K. Bachmann, H. D. Bausen, H. Lade, D. Leers, D. U. Wiechert, N. Herres, R. Kohl and P. Koidl, Raman and X-Ray Studies of Polycrystalline Cvd Diamond Films, *Diamond and Related Materials*, 3 (1994) 1308-1314.
- [45] A. Hammiche, L. Bozec, M. Conroy, H. M. Pollock, G. Mills, J. M. R. Weaver, D. M. Price, M. Reading, D. J. Hourston and M. Song, Highly localized thermal, mechanical, and spectroscopic characterization of polymers using miniaturized thermal probes, *J. Vac. Sci. Technol., B*, 18 (2000) 1322-1332.
- [46] D. W. Oxtoby and N. H. Nachtrieb, *Principles of Modern Chemistry*, Saunders College Publishing, Orlando, FL, 3rd edn., 1996.

- [47] M. Alcoutlabi and G. B. McKenna, Effects of confinement on material behaviour at the nanometre size scale, *Journal of Physics-Condensed Matter*, 17 (2005) R461-R524.
- [48] C. L. Jackson and G. B. McKenna, The Melting Behavior of Organic Materials Confined in Porous Solids, *J. Chem. Phys.*, 93 (1990) 9002-9011.
- [49] P. Buffat and J. P. Borel, Size Effect on Melting Temperature of Gold Particles, *Phys. Rev. A*, 13 (1976) 2287-2298.
- [50] Y. S. Touloukian, *Thermal conductivity: nonmetallic solids*, IFI/Plenum, New York, 1970.
- [51] J. Lee, T. L. Wright, M. R. Abel, E. O. Sunden, A. Marchenkov, S. Graham and W. P. King, Thermal conduction from microcantilever heaters in partial vacuum, *J. Appl. Phys.*, (2006 - in press)
- [52] K. Park, J. Lee, Z. M. Zhang and W. P. King, Frequency-dependent electrical and thermal response of heated atomic force microscope cantilevers, *J. Microelectromech. Syst.*, (2006 - in press)
- [53] F. P. Incropera and D. P. DeWitt, *Fundamentals of Heat and Mass Transfer*, Wiley, New York, 5th edn., 2002.
- [54] Z. Y. Guo and Z. X. Li, Size effect on microscale single-phase flow and heat transfer, *Int. J. Heat Mass Transfer*, 46 (2003) 149-159.
- [55] M. Asheghi, K. Kurabayashi, R. Kasnavi and K. E. Goodson, Thermal conduction in doped single-crystal silicon films, *J. Appl. Phys.*, 91 (2002) 5079-5088.
- [56] W. Liu, K. Etessam-Yazdani, R. Hussin and M. Asheghi, Modeling and data for thermal conductivity of ultrathin single crystal-silicon SOI layers at high temperature, *IEEE Trans. Electron Devices*, 53 (2006) 1868-1876.
- [57] P. J. Timans, Emissivity of Silicon at Elevated-Temperatures, *J. Appl. Phys.*, 74 (1993) 6353-6364.

CHAPTER 4

DIRECT DEPOSITION OF CONTINUOUS METAL NANOSTRUCTURES BY THERMAL DIP-PEN NANOLITHOGRAPHY

This chapter describes the direct deposition of continuous metal nanostructures onto glass and silicon surfaces using a silicon heated atomic force microscope cantilever tip [1]. Much like a nanometer-scale soldering iron, the cantilever tip is coated with indium metal, which can be deposited onto a surface forming continuous lines of width less than 80 nm and height near 1 nm. Deposition is controlled using the internal resistive heater of the cantilever to melt the indium. When the cantilever is unheated, no metal is deposited from the tip, allowing the writing to be registered to existing features on the surface. Depositing a continuous indium electrical connection between two metal electrodes separated by a submicron gap demonstrates the potential for direct-write circuit repair using the heated cantilevers.

4.1 Introduction

Dip-pen nanolithography (DPN) is a scanning-probe based nanolithography technique that uses the probe tip like an inked pen, transferring a chemical “ink” coating from the probe tip to a surface through direct contact between the tip and surface [2]. Chemical inks deposited by DPN include thiols, biomolecules, sols, silanes, and nanoparticles [3]. DPN offers great promise because of its ease of use and resolution of

15 nm or better. However, conventional DPN requires inks that are mobile under ambient conditions, thereby incurring two significant limitations. First, the ink deposition rate from a given probe can only be affected by heating the substrate or by changing the ambient humidity or temperature [4, 5], making dynamic control of deposition difficult. Second, the inability to ‘turn off’ deposition induces contamination or smearing if the inked probe performs post-deposition metrology. Thermal DPN (tDPN), shown in Figure 4.1, overcomes these limitations by using a cantilever with an integrated heater to perform DPN with an ink that is solid at room temperature and flows only when melted at higher temperatures [6]. Deposition may be turned on and off by modulating heating power and, because the ink is solid at room temperature, an inked cantilever can image a surface or a deposit without contaminating the surface with additional ink.

The requirement for inks to be mobile at room temperature in conventional DPN has led to an emphasis on organic self-assembled monolayer and biomolecular inks, with only a few efforts to write the electrically conducting nanostructures that would be required for nanoelectronics. Conducting polymers have been patterned electrochemically [7-9] and in a sol-like process [10], and DPN of sols has generated magnetic and semiconductor nanostructures [11, 12]. In forming metallic nanostructures, DPN has been used to deposit clusters of metal nanoparticles [13, 14], form etch resists on top of thin metallic films [15-17], and act as a source of metal salt for electrochemical or electroless surface reduction [18-20]. Many applications, including nanometer-scale circuit fabrication and mask writing, require nanoscale deposition of continuous metal films. However, to our knowledge, current DPN metallic deposition techniques have not

demonstrated the single-step formation of a continuous metal layer on an arbitrary substrate.

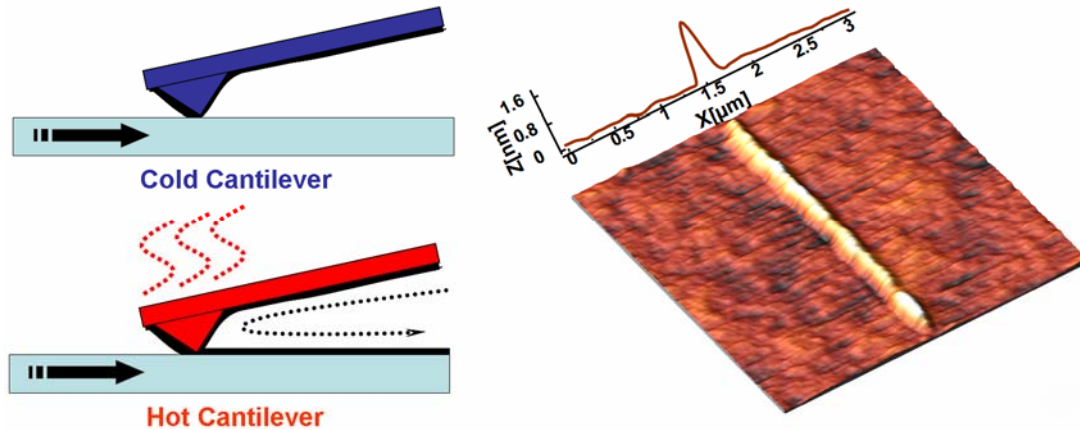


Figure 4.1. Left: Schematic of the operation of tDPN, which uses a heated AFM cantilever with a tip coated with a solid “ink.” When the tip is hot enough to melt the ink, it flows onto the substrate. No deposition occurs when the tip is cold, allowing imaging without unintended deposition. Right: A topographic AFM image of a continuous nanostructure deposited from an In-coated tip onto a borosilicate glass substrate.

In this chapter, tDPN is used to perform nanoscale deposition of indium metal, using the heated AFM probe tip much like a nanometer-scale soldering iron. The cantilever registered the written deposit to previously-fabricated structures and performed post-deposition metrology without contamination. Electrical measurements and Auger nanoprobe spectroscopy confirmed the electrical continuity and composition of the deposit. The direct deposition of metal demonstrates the feasibility of using tDPN for both structural and electrical deposition applications. The results presented within this chapter represent to our knowledge the first demonstration of electrical transport through a DPN-deposited material without further processing.

4.2 Experimental Results and Analysis

The described experiments used heatable silicon AFM cantilevers, similar to those described in Chapter 2 and shown in Figure 1.2, that were fabricated at GeorgiaTech using a standard silicon-on-insulator process [21]. Similar cantilevers have been developed for data storage [22]. The cantilever tip was fabricated on a microscale heater embedded in the cantilever, and had a radius of curvature of ~ 20 nm estimated from scanning electron microscopy. The cantilevers have a thermal time constant in the range of 1-10 μ s and a temperature-sensitive resistance that allows temperature calibration [23]. The room temperature electrical resistance of the cantilevers was ~ 2 k Ω , with a peak resistance close to 7 k Ω when heated to 550 $^{\circ}$ C.

Indium was chosen as the deposition metal because of its relatively low melting temperature of 156.6 $^{\circ}$ C and its high wettability on many surfaces, including ceramics, glass, silicon, and metal oxides [24]. Indium was loaded onto the cantilever tip by bringing a clean tip into contact with a layer of In with a force of ~ 20 nN at room temperature, and then heating the cantilever. The cantilever temperature required to melt the indium near the cantilever tip depended strongly on the contact force. At contact forces of ~ 20 nN, the cantilever temperature required to induce melting was over 1000 $^{\circ}$ C, while increasing the contact force to 1000 nN enabled melting the indium with the cantilever temperature at 500 $^{\circ}$ C. The thermal contact resistance between the cantilever and indium substrate was larger than the thermal resistance within the thermally conductive indium in contact with the tip, and thus the strong contact force-dependence of the cantilever temperature required to melt the indium substrate may be caused by the contact force-dependence of the contact area between the tip and substrate [25].

Although increasing the tip-substrate contact force yielded improved thermal contact, high contact forces caused tip wear, which reduced the imaging and deposition resolution. Contact forces were therefore kept as low as possible while still preventing the cantilever from having to be heated above 1000 °C. After melting was induced, the tip penetrated into the indium and the thermal resistance between the tip and substrate was reduced, causing the cantilever temperature to decrease to roughly half of its value before melting. Despite the decreased cantilever temperature, the In substrate beneath the tip remained melted after tip penetration. Successful loading of indium onto the cantilever occurred by scanning the tip on an In substrate with a contact force of 500 nN at 6 $\mu\text{m/s}$ while heating the cantilever at 13.4 mW, or ~ 1030 °C. After loading, the tip was pulled out of contact with the indium and the cantilever heat was turned off.

The indium-coated cantilever could redeposit indium onto another surface by simply reheating the cantilever while the tip was in contact with the second surface. Scanning the tip while heating produced continuous lines of deposited indium, an example of which is shown in Figure 4.1. The dimensions of the deposited line depended on the tip loading, deposition temperature, deposition speed, and the number of repetitions along the deposition line. Continuous lines have been deposited over a wide range of conditions, from cantilever temperatures of 250 to 800 °C, tip speeds of 0.01 to 18 $\mu\text{m/s}$, 32 to 128 raster scans, and on substrates of borosilicate glass, silicon with a native oxide, and 1 μm thick thermally-grown silicon oxide. Deposited lines ranged from 50 to 300 nm in width and from 3 to 12 nm in height. The thickness to width ratio never exceeded unity. Repeated imaging with a cool indium-coated tip had no effect on the

deposited lines, and contamination, spreading, or loosening of the deposited indium was never observed.

To test the electrical continuity and transport properties of the deposited indium, a substrate with gold electrodes separated by a 500 nm gap was fabricated by e-beam lithography onto a 100 nm thick silicon oxide film on a silicon substrate. Before heating the cantilever, the indium-coated tip was used to image the electrode and locate the gap. To deposit indium across the gap, the tip was heated with 5.34mW to ~ 425 °C, and the tip scanned along a 2 μm line spanning the gap at 4 $\mu\text{m/s}$. After scanning the line continuously for 32 seconds, the resulting deposit was 5 nm tall and had a width varying from 100-200 nm.

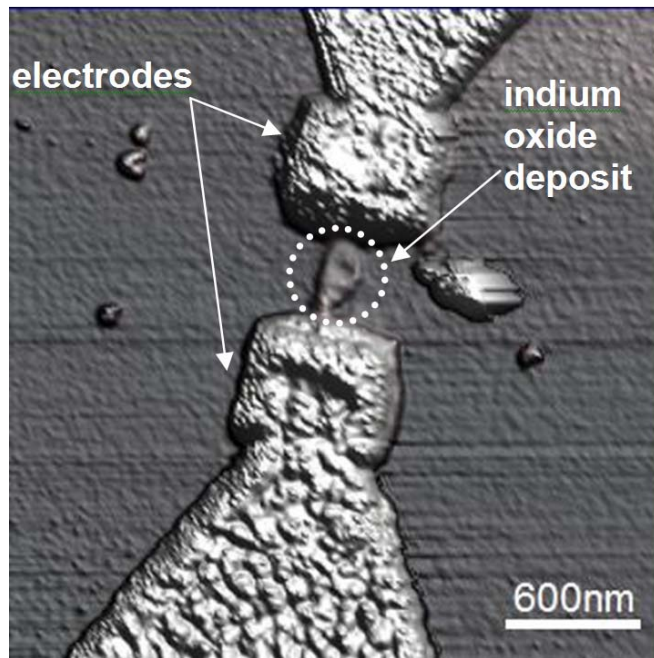


Figure 4.2. Topographical AFM image of a continuous structure deposited with In across a 500 nm-wide gap (circled) between pre-fabricated gold electrodes.

Chemical and electrical analyses of the nanostructures were performed in a unique ultrahigh vacuum (UHV) instrument combining a scanning electron microscope (SEM), a scanning Auger nanoprobe, and a four-tip nanoprobe capable of making *in situ*

transport measurements across structures $<1 \mu\text{m}$ long. As shown in Figure 4.3, Auger electron spectroscopy performed directly on the nanostructure demonstrates that the deposit was pure indium oxide. Because the height of the deposit was less than the ~ 10 nm thickness of the native oxide of indium, the deposited indium likely oxidized completely before electrical measurements could be performed. Although not as conductive as indium, indium oxide is a conductor and has applications in molecular electronics and sensing [26]. Current-voltage (IV) measurements were made by contacting Pt probe tips to the Au contacts near the junction. The linearity of the IV measurement shown in Figure 4.4 demonstrated that the deposit was continuous and ohmic, with a resistivity of $2.5 \times 10^4 \Omega\text{-cm}$. No electrical conduction was observed between electrodes without indium deposits.

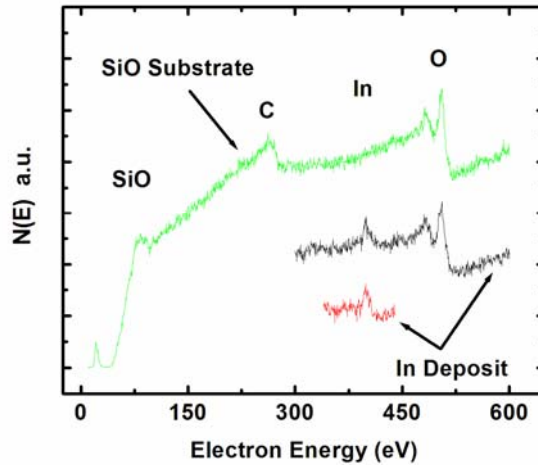


Figure 4.3. Auger electron nanoprobe spectra collected at two different locations on the nanostructure and on the adjacent silicon oxide substrate demonstrating that the structure is indium oxide. Note that the spectra are displayed as total electron count, $N(E)$, not dN/dE .

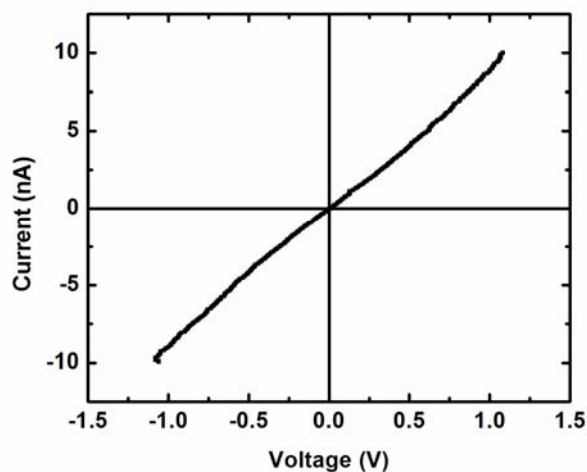


Figure 4.4. Electrical transport through the nanowire structure shown in Figure 4.2, demonstrating that the formed structure is continuous and ohmic.

The electrical resistivity of indium oxide depends strongly on the deposition conditions, with reported values ranging from 10^{-4} to 10^8 Ω -cm, making the measured resistivity within the reported range [27, 28]. Amorphous indium oxide films have shown higher resistivity than polycrystalline films [27], and poor crystallinity has resulted from indium oxide film deposition at low temperatures [27, 28]. Since the substrate was not independently heated during our experiment, the deposited liquid indium would have been rapidly quenched as it flowed from the hot tip to the cool substrate. Rapid quenching would lead to a more disorganized film, which is consistent with the high measured resistivity. Possible means of preserving the highly conductive metallic indium include depositing thicker wires that would not completely oxidize and performing the deposition in UHV (another notable capability of tDPN). Furthermore, a deep understanding of the interplay between the tip, ink, and the temperature field within the substrate will allow thermal engineering of the substrate and therefore provide greater deposition control.

4.3 Conclusions

The direct writing of electrically continuous nanowires significantly expands the capabilities of DPN. This nanosoldering requires the combined metrology and lithography capabilities of tDPN and could not be performed with conventional DPN. The ability to deposit locally a solid metal could enable the direct prototyping of nanoelectronics or the photomasks used in optical lithography. Moreover, deposition could be coupled with AFM surface metrology to perform *in-situ* inspection and repair of nanoelectronics. Finally, this technique could be performed in parallel using the extensive cantilever arrays already demonstrated [22], which could be pre-coated with In or other materials during fabrication.

4.4 References

- [1] B. A. Nelson, W. P. King, A. R. Laracuate, P. E. Sheehan and L. J. Whitman, Direct deposition of continuous metal nanostructures by thermal dip-pen nanolithography, *Applied Physics Letters*, 88 (2006) 033104.
- [2] R. D. Piner, J. Zhu, F. Xu, S. Hong and C. A. Mirkin, "Dip-Pen" Nanolithography, *Science*, 283 (1999) 661-663.
- [3] D. S. Ginger, H. Zhang and C. A. Mirkin, The evolution of dip-pen nanolithography, *Angewandte Chemie, International Edition in English*, 43 (2004) 30-45.
- [4] E. J. Peterson, B. L. Weeks, J. J. De Yoreo and P. V. Schwartz, Effect of environmental conditions on Dip Pen Nanolithography of mercaptohexadecanoic acid, *Journal of Physical Chemistry B*, 108 (2004) 15206-15210.
- [5] P. E. Sheehan and L. J. Whitman, Thiol diffusion and the role of humidity in "Dip-Pen Nanolithography", *Physical Review Letters*, 88 (2002) 156104/1-156104/4.

- [6] P. E. Sheehan, L. J. Whitman, W. P. King and B. A. Nelson, Nanoscale deposition of solid inks via thermal dip pen nanolithography, *Applied Physics Letters*, 85 (2004) 1589-1591.
- [7] J. H. Lim and C. A. Mirkin, Electrostatically driven dip-pen nanolithography of conducting polymers, *Advanced Materials*, 14 (2002) 1474-+.
- [8] B. W. Maynor, S. F. Filocamo, M. W. Grinstaff and J. Liu, Direct-writing of polymer nanostructures: Poly(thiophene) nanowires on semiconducting and insulating surfaces, *Journal of the American Chemical Society*, 124 (2002) 522-523.
- [9] A. Noy, A. E. Miller, J. E. Klare, B. L. Weeks, B. W. Woods and J. J. DeYoreo, Fabrication of luminescent nanostructures and polymer nanowires using dip-pen nanolithography, *Nano Letters*, 2 (2002) 109-112.
- [10] M. Su, M. Aslam, L. Fu, N. Q. Wu and V. P. Dravid, Dip-pen nanopatterning of photosensitive conducting polymer using a monomer ink, *Applied Physics Letters*, 84 (2004) 4200-4202.
- [11] L. Fu, X. G. Liu, Y. Zhang, V. P. Dravid and C. A. Mirkin, Nanopatterning of "hard" magnetic nanostructures via dip-pen nanolithography and a sol-based ink, *Nano Letters*, 3 (2003) 757-760.
- [12] M. Su, X. G. Liu, S. Y. Li, V. P. Dravid and C. A. Mirkin, Moving beyond molecules: Patterning solid-state features via dip-pen nanolithography with sol-based inks, *Journal of the American Chemical Society*, 124 (2002) 1560-1561.
- [13] M. Ben Ali, T. Ondarcuhu, M. Brust and C. Joachim, Atomic force microscope tip nanoprinting of gold nanoclusters, *Langmuir*, 18 (2002) 872-876.
- [14] J. C. Garno, Y. Y. Yang, N. A. Amro, S. Cruchon-Dupeyrat, S. W. Chen and G. Y. Liu, Precise positioning of nanoparticles on surfaces using scanning probe lithography, *Nano Letters*, 3 (2003) 389-395.
- [15] K. S. Salaita, S. W. Lee, D. S. Ginger and C. A. Mirkin, DPN-generated nanostructures as positive resists for preparing lithographic masters or hole arrays, *Nano Letters*, 6 (2006) 2493-2498.

- [16] H. Zhang, R. C. Jin and C. A. Mirkin, Synthesis of open-ended, cylindrical Au-Ag alloy nanostructures on a Si/SiO_x surface, *Nano Letters*, 4 (2004) 1493-1495.
- [17] H. Zhang and C. A. Mirkin, DPN-generated nanostructures made of gold, silver, and palladium, *Chemistry of Materials*, 16 (2004) 1480-1484.
- [18] Y. Li, B. W. Maynor and J. Liu, Electrochemical AFM "dip-pen" nanolithography, *Journal of the American Chemical Society*, 123 (2001) 2105-2106.
- [19] B. W. Maynor, Y. Li and J. Liu, Au "ink" for AFM "dip-pen" nanolithography, *Langmuir*, 17 (2001) 2575-2578.
- [20] L. A. Porter, H. C. Choi, J. M. Schmeltzer, A. E. Ribbe, L. C. C. Elliott and J. M. Buriak, Electroless nanoparticle film deposition compatible with photolithography, microcontact printing, and dip-pen nanolithography patterning technologies, *Nano Letters*, 2 (2002) 1369-1372.
- [21] B. W. Chui, T. D. Stowe, Y. S. Ju, K. E. Goodson, T. W. Kenny, H. J. Mamin, B. D. Terris and R. P. Ried, Low-stiffness silicon cantilever with integrated heaters and piezoresistive sensors for high-density data storage, *Journal of Microelectromechanical Systems*, 7 (1998) 69-78.
- [22] P. Vettiger, G. Cross, M. Despont, U. Drechsler, U. Durig, B. Gotsman, W. Haberle, M. Lantz, H. Rothuizen, R. Stutz and G. Binnig, The "millipede" - nanotechnology entering data storage, *IEEE Transactions on Nanotechnology*, 1 (2002) 39-55.
- [23] W. P. King, T. W. Kenny, K. E. Goodson, G. L. W. Cross, M. Despont, U. T. Durig, H. Rothuizen, G. Binnig and P. Vettiger, Design of atomic force microscope cantilevers for combined thermomechanical writing and thermal reading in array operation, *Journal of Microelectromechanical Systems*, 11 (2002) 765-774.
- [24] M. T. Ludwick, *Indium; discovery, occurrence, development, physical and chemical characteristics, and a bibliography of indium (annotated) 1863-1958 inclusive.*, Indium Corporation of America, Utica, N.Y., 1959.
- [25] W. P. King and K. E. Goodson, *Resolution limits of nanoscale thermal processing with the atomic force microscope*, ASME IMECE 2002 Symposium on Thermal Issues in Nanomaterials and Nanofabrication, New Orleans, LA, 2002, pp. Paper No. IMECE2002-33854.

[26] V. Golovanov, M. A. Maki-Jaskari, T. T. Rantala, G. Korotcenkov, V. Brinzari, A. Cornet and J. Morante, Experimental and theoretical studies of indium oxide gas sensors fabricated by spray pyrolysis, *Sensors and Actuators B - Chemical*, 106 (2005) 563-571.

[27] B. R. Krishna, T. K. Subramanyam, B. S. Naidu and S. Uthanna, Effect of substrate temperature on the electrical and optical properties of dc reactive magnetron sputtered indium oxide films, *Optical Materials*, 15 (2000) 217-224.

[28] S. Kasiviswanathan and G. Rangarajan, Direct-Current Magnetron-Sputtered In₂O₃ Films As Tunnel Barriers, *Journal of Applied Physics*, 75 (1994) 2572-2577.

CHAPTER 5

MEASURING MATERIAL SOFTENING WITH NANOSCALE SPATIAL RESOLUTION USING HEATED SILICON AFM PROBES

This chapter describes the use of heated silicon AFM probes to perform local thermal analysis (LTA) of a thin film of polystyrene [1]. The experiments measure film softening behavior with 100 nm spatial resolution, whereas previous research on LTA used probes that had a resolution near 10 μm , which was too large to investigate some types of features. This chapter demonstrates four methods by which heated silicon probes can perform thermal analysis with nanoscale spatial resolution. The polystyrene softening temperature measured from nanoscale LTA techniques is 120 $^{\circ}\text{C}$, compared to 100 $^{\circ}\text{C}$ measured with bulk ellipsometry. The discrepancy is attributed to the thermal contact resistance at the end of the silicon probe tip, on the order of 10^8 K/W, which modulates heat flow between the tip and sample and governs the fundamental limits of this technique. The use of a silicon probe for LTA enables bulk fabrication, parallelization for high throughput analysis, and fabrication of a sharp tip capable of nanoscale spatial resolution.

5.1 Introduction

Many techniques exist for measuring the temperature-dependence of material properties. A common technique for measuring chemical and thermodynamic properties is differential scanning calorimetry (DSC). DSC measures phase transitions in a material

of interest through observed discontinuities in the material heat capacity. DSC has two drawbacks that limit its application to systems at and below the micron scale. First, DSC measures phase transitions for lumped samples, making DSC insensitive to the variation in phase transition temperature that can occur at surfaces and interfaces in heterogeneous materials. Second, since DSC heats the entire sample mass, it can be destructive and thus not applicable for *in situ* characterization. If the sample is part of a larger system, the system could be compromised as it is heated through the glass transition, melting, or decomposition temperatures of its components. Local thermal analysis (LTA), described in section 2.4.1.3, overcomes these drawbacks by sampling specific regions using a local thermal probe.

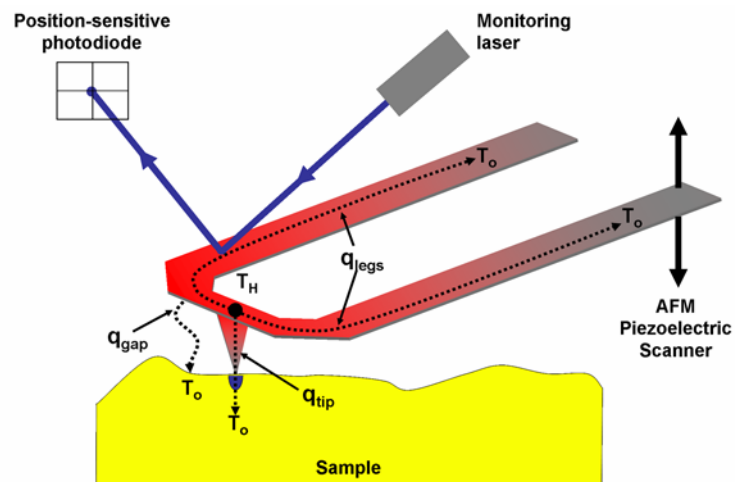


Figure 5.1 Principle of Local Thermal Analysis. A heated probe is in contact with the sample to be characterized. Heat is generated at the bridge of the probe, marked by the hot temperature T_H , and flows down the legs of the probe, across the air gap, and through the tip to the ambient temperature T_o . Phase transitions in the sample cause the tip to sink into the softened sample and change the thermal resistance between the probe and sample. The onset of phase transition can be detected electronically due to the coupling between the thermal and electrical properties of the probe or optically by using a reflected laser to monitor the vertical position of the probe.

A thermally-active probe used in atomic force microscopy (AFM) allows the imaging capabilities of AFM to be integrated with local heat delivery for LTA [2]. Figure 5.1 illustrates the principle of AFM-based LTA, where heat generated by the

probe flows through the probe tip into the substrate. In past LTA efforts, the thermally-active probe used was the Wollaston wire probe described in section 2.1.1, which had a lateral topographic resolution on the order of 1 μm . The probe could generate topographic and thermal contrast images to identify regions of interest using standard AFM imaging techniques and then serve as a localized heat source for thermal analysis [3, 4]. Because the substrate was locally heated, the sampled material was confined to the contact region between the hot probe tip and the substrate, allowing specific micron scale heterogeneities, interphase regions, and surface phases to be probed while leaving the remainder of the bulk unperturbed.

LTA has been used in a variety of applications, with lateral sampling resolution typically in the range of tens of microns [5]. One study used LTA to investigate the effects of confinement on thin polymer films by measuring the glass transition temperature (T_g) of polystyrene (PS) thin films as a function of film thickness [6]. Mapping the microscale spatial variation of glass transition temperatures in heterogeneous materials using LTA allowed *in situ* characterization of polymer composite interfaces [7, 8], determination of thermal history [9], and measurement of photooxidation depth [10]. In pharmaceuticals, LTA determined drug polymorphs on the surface of pharmaceutical tablets *in situ*, which was significant because the surface morphology of active chemicals can play a key role in dissolution within the body [11]. Several studies have compared LTA to conventional DSC and have shown good agreement [12-14].

Although LTA using the Wollaston probe was effective for measuring phase transitions, the resulting melted crater was no smaller than 1 μm by 500 nm for 100 nm

thick polymer films [6], and exhibited a width on the order of tens of microns for bulk samples [11]. At this resolution, investigating near-surface effects and composite interphase regions, for which the region of interest may be on the order of 100 nm [10, 11, 15], is not possible. The resolution limits of the Wollaston probe also prevent examination of three-dimensional nanoscale confinement effects on phase transition temperatures which typically occur below 50 nm for crystalline materials [16, 17]. It is therefore desirable to perform thermal analysis with probes having tips sharp enough to achieve nanoscale spatial resolution. Additionally, high-throughput screening can be achieved by performing LTA with multiple probes operating in parallel, which is not practical with the individually fabricated Wollaston probes [18]. The present chapter describes nanoscale thermal analysis (nanoTA) using batch-fabricated silicon probes with integrated heaters and oxide-sharpened tips with radius of curvature less than 20 nm. The technique can achieve a spatial resolution of about 100 nm.

5.2 Instrumentation

The silicon probes described in this article were fabricated by our group using a standard silicon-on-insulator process and are similar to heated probes originally designed for data storage [19-21] and shown in Figure 1.2. The silicon probe is batch-fabricated, which enables parallelization [22], low cost, and oxide-sharpening to achieve tip sharpness equivalent to the current state of the art. The radius of curvature at the end of the tip was routinely less than 20 nm. The probes had a tip height of $\sim 1 \mu\text{m}$, resonant frequency of 50-150 kHz, and spring constant near 1 N/m, which was calibrated using the thermal noise method [23]. The electrical resistance of the probes was temperature-

dependent, varying from $\sim 500 \Omega$ at room temperature to $\sim 1 \text{ k}\Omega$ at $\sim 850 \text{ }^\circ\text{C}$, which allowed using the resistance to determine the temperature of the probe. The probe heater temperature, T_H , was calibrated by using Raman spectroscopy to measure the temperature-dependent shift in the Stokes peak in the Raman spectrum of the heater [24], as described in Chapter 3.

The silicon probes can sensitively measure surface topography through the thermal coupling of the probe to the substrate, as described in section 2.3.2, which eliminates the need for optical instrumentation [25-27]. It would be difficult to operate a large array of probes if each probe in the array required a laser-based deflection measurement to measure surface topography. Thus the thermal topography reading critically enables large scale parallelization.

In order to detect phase transitions, LTA requires either the probe displacement to be monitored as it penetrates into a softened substrate, or the simultaneous measurement of temperature and power in order to detect changes to the thermal impedance between the probe and its environment. As a sample undergoes a phase transition, there is a change in the amount of energy required to raise the sample temperature. LTA measures this through changes to the thermal contact between the probe and the substrate [6, 14]. When a small amplitude temperature oscillation is superimposed onto the normal LTA temperature ramp, changes to the thermal contact yield similar discontinuities in AC measurements of thermal impedance [4].

The instrumentation developed for LTA with Wollaston probes is generally not appropriate for performing nanoTA with silicon probes because the heat transfer from the silicon probes is much different than from the Wollaston probes. New instrumentation

for nanoTA with a silicon probe should also be compatible with parallel probe operation, since the silicon probe can be parallelized for increased throughput. Optical detection was the most commonly used method to identify substrate softening with Wollaston probes, but it is poorly suited to large scale parallelization. Also, because optical detection measures the physical position of the probe, it can have errors due to the various mechanisms that can cause vertical probe motion in the AFM. Common causes of vertical probe motion include creep of the piezoelectric AFM scanner, thermal expansion of the substrate, and thermal stress-induced bending of the probe.

The sharp tips of the silicon probes constrict heat flow at the end of the tip, making it difficult to determine and control the temperature at the tip-substrate interface (T_{int}). Figure 5.2 shows the thermal resistance network for heat flow through and around the tip of the silicon probe in contact with a substrate. Due to the sharpness of the tip, the thermal contact resistance (R_{contact}) at the end of the tip represents a significant part of the thermal resistance network, which was not the case for the blunter Wollaston probe. The thermal resistance within the tip (R_{tip}) is on the order of 10^6 K/W, and for a polymer substrate R_{contact} and the spreading thermal resistance (R_{spread}) are estimated to be on the order of 10^7 K/W and 10^8 K/W, respectively. The thermal resistance of the ambient medium (R_{gap}) operates in parallel to R_{tip} , R_{contact} , and R_{spread} , and for a given T_H has a minimal effect on T_{int} . R_{tip} can be neglected because it is small compared to R_{contact} and R_{spread} for our probes. A significant implication of R_{contact} is that it can cause T_{int} to be lower than the calibrated T_H [28].

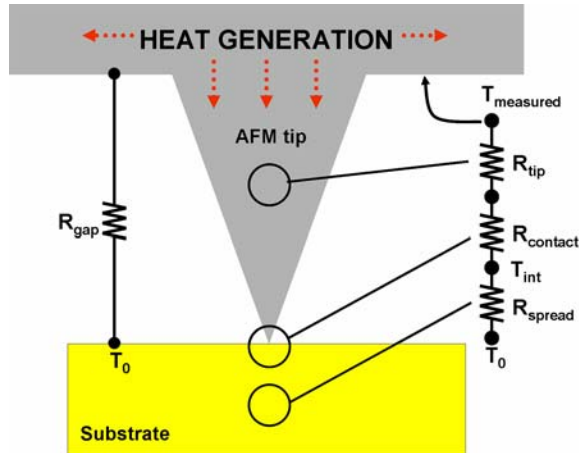


Figure 5.2 Thermal circuit for heat flow through the tip of a heated AFM probe. The relative sizes of the thermal resistances of the tip, R_{tip} , interface, $R_{contact}$, and substrate, R_{spread} , determine the temperature at the interface between tip and substrate. The dominant mode of heat transfer from probe to substrate is through the air gap, which has a thermal resistance R_{gap} . The calibrated temperature of the probe corresponds to the temperature of the heater region above the tip.

$R_{contact}$ is sensitive to the contact area between the tip and the substrate, so T_{int} can depend on the contact force. Precise and repeatable LTA requires the tip-sample contact force to be carefully monitored. In general AFM use, vertical position feedback maintains constant contact force between the tip and substrate. With heated silicon probes, maintaining constant force is challenging even with feedback because the silicon probes have temperature-dependant mechanical stiffness [21] and can exhibit thermally-induced bending. For the silicon probes used here, experiments showed that force was best held constant with vertical position feedback, so feedback was used for all the results shown in this chapter. In contrast, LTA with Wollaston probes was generally performed without feedback in order to avoid driving the tip into the sample after it softened [5]. This practice minimized the size of the crater left in the substrate and maximized spatial resolution. However, the lack of feedback resulted in a variable contact force due to thermal expansion of the sample and creep in the AFM scanner. Since $R_{contact}$ was negligible for the Wollaston probe, the changing contact area had little effect on T_{int} .

Only a small portion of the total heat generated in the silicon probe flows through the tip. Figure 5.1 shows the three heat flow paths from the heater region of the probe: from the heater to the base of the probe through the legs (q_{legs}), from the heater and legs to the substrate through the ambient medium (q_{gap}), and from the heater to the substrate through the tip (q_{tip}). About 85% of the power dissipated in the heater flows from the heater to the substrate, of which q_{tip} accounts for only about 0.1% [28]. Changes to the thermal interaction at the tip are thus difficult to detect even though the probe temperature depends upon R_{gap} , which is sensitive to the separation distance between the heater and substrate. In order to stop an experiment at the minimum possible temperature and maximize sampling density, changes to R_{gap} must be detectable at the immediate onset of softening. To capitalize on the potential of heated silicon probes for nanoscale spatial resolution, new methods of performing thermal analysis must overcome the weak thermal coupling between the silicon probe tip and the substrate.

5.3 Experiment and Results

This section describes four techniques for performing thermal analysis that capitalize on the nanoscale resolution of heated silicon probes and are compatible with parallel operation. For each of the techniques, the sample used was a 44k molecular weight PS film spun 170 nm thick on a silicon substrate and having a T_g of 100 °C. For each method described, the contact force between the probe tip and the PS substrate was 300 nN. A sourcemeter supplied voltage to the probe and simultaneously measured

current. The cantilever was mounted in a commercial AFM system, which provided force feedback, positioning, and topographical imaging.

5.3.1 Method 1: Indentation Depth

The first method of LTA with silicon probes consisted of holding the probe in contact with the substrate for a specified time, temperature and contact force, and then moving to new locations and repeating at higher temperatures. After the maximum desired temperature was applied, the probe then measured the resultant topography of the substrate. This technique is similar to studies of thresholds for bit formation in thermomechanical data storage [19, 29], but differs in two ways. First, in this method, the variation of indentation depth was measured as a function of temperature in order to determine the onset of softening for the substrate. In addition, for thermomechanical data storage the primary concern was in determining the threshold for forming data bits in the substrate, whereas in this method the primary concern is characterizing the substrate itself.

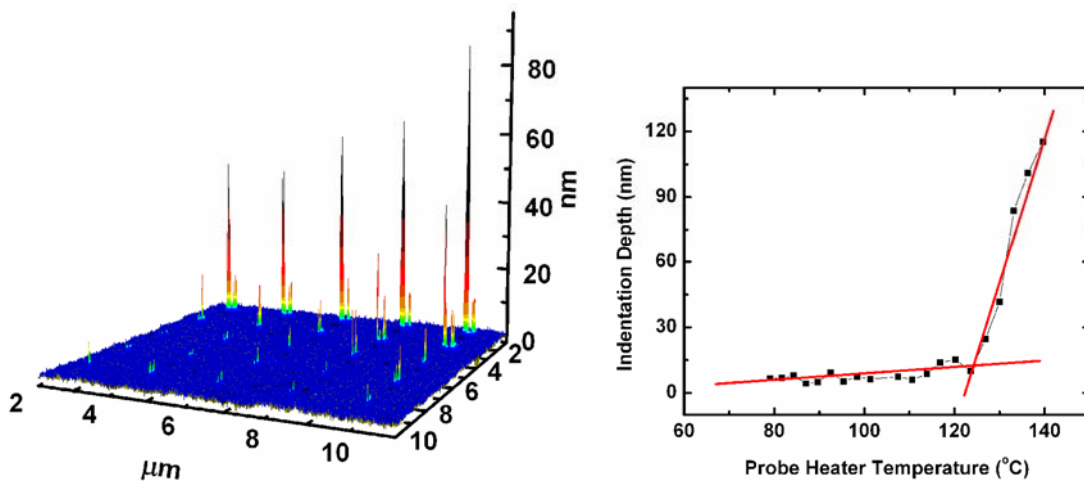


Figure 5.3 Inverted topography (left) and measured depth (right) of indentations made with a heated probe held at various temperatures for 10 seconds each at 300 nN. Above T_g the indent depth increases rapidly with temperature. The scan size of the topographical image was $10 \times 10 \mu\text{m}^2$.

Figure 5.3 shows the inverted topography and the measured penetration depth as a function of T_H for 10 second hold times on the PS film. The temperature was increased from 80-140 °C in steps of ~3 °C. Below 120 °C, very little tip penetration into the substrate occurred, whereas above 120 °C the PS substrate was raised above its T_g , increasing the mechanical compliance of the polymer and causing the tip penetration depth to increase roughly linearly with temperature. This method of performing LTA is time intensive, but it yields a clear and reliable transition in compliance behavior and with proper spacing could have a spatial resolution on the order of 1 μm , which is an order of magnitude improvement over the Wollaston probe. Furthermore, since the silicon probes can measure substrate topography thermally, the method is parallelizable.

5.3.2 Method 2: Shear Modulation to Measure Tip Penetration

Another way to mechanically measure tip penetration into the substrate is through shear modulation [30, 31]. In this technique, the tip was stationary while a small in-plane oscillation was applied to the substrate, perpendicular to the cantilever legs of the probe. The lateral motion of the substrate applied a frictional force to the end of the probe tip, which exerted a torque on the cantilever and induced lateral motion of the reflected laser on the AFM photodetector. A lock-in amplifier measured the amplitude of the lateral motion of the reflected laser, which was related to the torque on the probe. This technique has previously been demonstrated both with heat supplied to the entire substrate [30], and with heat locally supplied by the probe [31], as in this article.

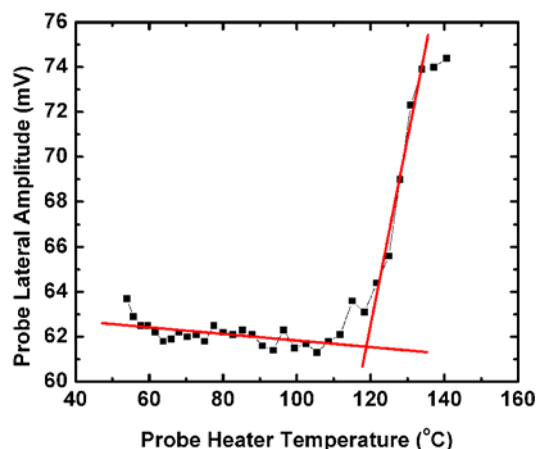


Figure 5.4 Amplitude of lateral tip motion as a function of probe temperature with the probe tip in contact with a PS substrate that is subjected to 3 nm of lateral oscillation. Above the glass transition, the tip sinks into the PS, which increases the torque on the cantilever and increases the lateral tip motion of the probe.

To demonstrate Method 2, the PS substrate was oscillated at 7 kHz with a 3 nm amplitude while the probe temperature was raised from 50 to 140 °C in increments of ~3 °C. Figure 5.4 shows the resultant amplitude of the lateral motion of the reflected laser as a function of T_H . A discontinuity in the lateral amplitude occurs near 120 °C due to tip penetration into the softened PS substrate. The torque on the probe increased as the tip penetrated, increasing the torsion experienced by the probe and increasing the lateral motion of the reflected laser. Because of the small lateral motion of the substrate and relatively high contact force, slip at the tip-substrate interface was unlikely to occur.

With this technique, nanoTA is achieved because the phase transition was sampled in a single sample location rather than over an array of locations as in Method 1. The method also gives clear indication of substrate softening without requiring post-processing, thereby enabling immediate phase transition detection. However, the method requires optical detection of cantilever motion, which is poorly-suited to parallelization.

5.3.3 Method 3: Differential Measurements of Thermal Impedance

To maintain capability for parallelization, LTA should be performed without using optical detection of cantilever motion. This can be achieved by measuring the probe temperature and dissipated power to monitor changes in the DC thermal impedance from the probe. By superimposing a small amplitude temperature oscillation onto a slower temperature ramp and measuring the phase and amplitude response of the probe with a lock-in amplifier, AC measurements of thermal impedance can also be made. Figure 5.5 shows the experimental configuration, which is similar to Modulated-Temperature DSC (MT-DSC). In MT-DSC, thermodynamic and kinetic information about phase transitions is determined from the difference in total power, thermal phase, and thermal amplitude between the sample of interest and a reference sample, and similar differential measurements can be applied to LTA.

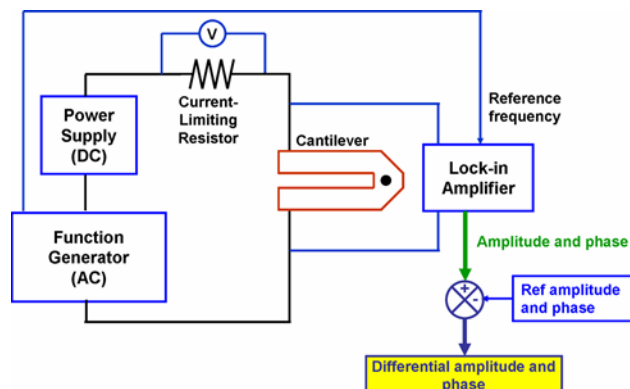


Figure 5.5 Experimental setup for performing thermal analysis with Method 3. A small AC temperature dither is connected in series with a slow temperature ramp. A lock-in amplifier measures the AC phase and amplitude response of the probe, and the reference power, amplitude, and phase are subtracted out numerically.

The reference signal used for differential measurements in this method came from recording the power, AC amplitude, and AC phase as a function of T_H with the silicon probe in contact with a glass substrate instead of the polymer sample to be analyzed. The reference data was subtracted from the polymer sample data numerically. This reference

signal differs from that used with Wollaston probes, for which the reference signal was taken from a second probe held away from the substrate and subjected to the same temperature ramp as the probe in contact [4]. Using a separate out-of-contact probe for a reference signal neglected variation in electrical and thermal behavior between probes and also neglected the differences between the thermal environments in which the probes were placed. Despite these differences in probe characteristics and thermal environment, the differential signals still gave clear indication of substrate phase transitions when used with the Wollaston probe. This reference signal could not be used with silicon probes because the differential signal was dominated by the thermal and electrical differences between probes rather than by changes to the probe-substrate thermal contact.

To demonstrate Method 3, the probe temperature was increased from 55 – 135 °C at a rate of ~30 °C/min while a temperature oscillation was superimposed at a frequency of 20 kHz and amplitude of ~10 °C. Figure 5.6 shows the total dissipated power and the differential power, AC phase, and AC amplitude as a function of T_H after subtracting the glass substrate reference data. The differential power exhibited a clear discontinuity at ~120 °C as the PS softened and the tip began to penetrate. The discontinuity was only visible in the differential signal, and could not be seen in the total dissipated power.

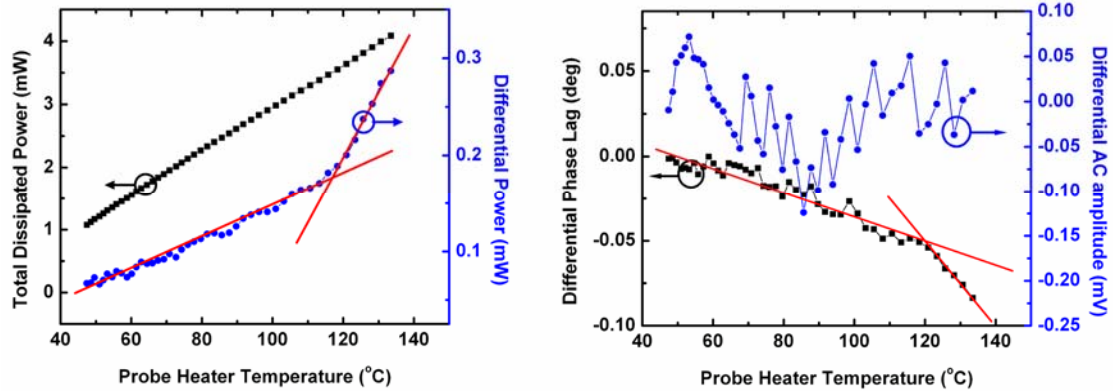


Figure 5.6 Total and differential dissipated power (left) and differential AC Phase and amplitude (right) of the probe during a temperature ramp on polystyrene. The differential power exhibits a clear change in slope as the substrate softens, while no transition is visible in the total dissipated power. The differential phase gives a weak indication and the differential amplitude gives no indication of softening. The reference signal for the differential data is taken from a temperature ramp with the probe in contact with a glass substrate.

The discontinuity in the differential power in Figure 5.6 occurred because the thermal impedance between the silicon probe and its environment was primarily dependent on the separation distance between the probe and substrate rather than the thermal properties of the substrate. The total thermal impedance was not sensitive to the thermal properties of the substrate since the thermal impedance of the substrate was small compared to the thermal impedance of the air gap, and so most of the substrate surface beneath the probe was close to ambient temperature. Until the tip began to penetrate into the PS substrate, the separation distance between the probe and substrate was determined by the tip height, causing the reference signals of the probe on a glass substrate to be very close to the signals on the polymer substrate. Once the tip began to penetrate into the substrate and the separation distance between the heater and the substrate started to decrease, the thermal impedance between the probe and substrate became smaller for the softened polymer than for the glass.

In the AC differential measurements of thermal impedance shown in Figure 5.6, a slight discontinuity at the softening point of the substrate may have occurred in the phase

lag at ~ 120 °C, but no transition was apparent in the amplitude. With the Wollaston probe, the differential AC phase and amplitude typically gave clear indication of phase transitions [4, 32]. In either case, measuring phase and amplitude adds experimental complexity over simply measuring differential power, yet gives no additional information. Unlike MT-DSC, quantitative thermodynamic and kinetic information cannot be determined from the differential signals because the signals indicate changes in thermal contact rather than changes in the heat capacity of the sample. Differential power, however, achieves nanoTA with clear phase transition detection but is still not ideal due to the requirement of post-processing to identify phase transitions.

5.3.4 Method 4: Thermally-measured Tip Penetration

To enable immediate phase transition detection with the silicon probes without external optics, methods of performing thermal analysis need to sense variations in the thermal environment of the probe with enough sensitivity to eliminate the need for post-processing. Immediate phase transition detection was accomplished by performing a stepped temperature ramp and recording the change in probe resistance (ΔR) at each step. The stepped temperature ramp was achieved by stepping the voltage applied to the probe, increasing the probe voltage from .8 to 1.38 V in steps of .2 V. This voltage ramp resulted in a temperature increase from 65 to 145 °C at a rate of ~ 30 °C/min in steps of ~ 3 °C. Each voltage was held for 4 seconds while the tip was held in continuous contact with the PS substrate.

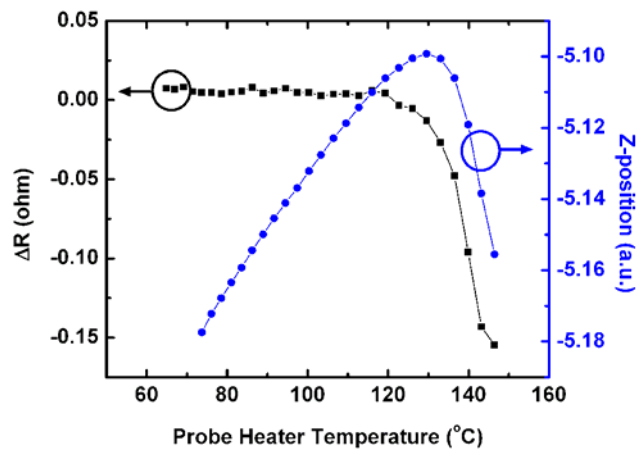


Figure 5.7 ΔR and deflection as a function of probe temperature while in contact with a PS film using Method 4. The optical deflection signal shows significant convolution from vertical deflection mechanisms while ΔR exhibits a clear drop as the tip begins penetrating into the film.

Figure 5.7 shows ΔR as a function of T_H for this experiment. At the onset of softening, ΔR changed from a small positive value below the substrate transition temperature to an increasingly negative value above the transition temperature, yielding a sudden decrease in ΔR due to the changing thermal impedance as the tip penetrated into the softened substrate. When the probe was in contact with the PS substrate and T_{int} was below the softening temperature of the PS, the probe temperature and resistance increased slightly with time as the substrate and air gap came into thermal equilibrium with the heater, causing ΔR to be small and positive. When the heater became hot enough to soften the PS, the tip began to penetrate, decreasing the thermal impedance between the probe and the substrate and causing T_H and the probe resistance to decrease, resulting in an increasingly negative value for ΔR . The abrupt drop in ΔR above 120 °C in Figure 5.7 was a typical result. Similar results also occurred for shorter voltage hold times.

Figure 5.7 shows that measuring ΔR yielded a sharper transition at the softening point of the substrate than optical detection of tip penetration. Because the deflection signal was a measurement of the vertical position of the probe, it was affected by all the mechanisms that move the probe vertically, described in section 5.2. In contrast, ΔR depended only on changes to the thermal impedance between the probe and the substrate, which was primarily determined by the tip penetration, tip height, and the separation between the legs and the substrate.

In this implementation of Method 4, the change in T_H during penetration was small at about .35 °C. The sensitivity to changes in thermal impedance could be improved by instead holding either the dissipated power or probe temperature constant at each interval while monitoring either ΔR or the change in power (ΔP), respectively. Whether holding voltage, resistance, or power constant, all three approaches measure changes to the thermal impedance between probe and substrate, but when voltage is held constant, the effect of the changing thermal impedance is divided between ΔR and ΔP . Although more complex than simply stepping the voltage applied to the probe, instrumentation could be used to maintain constant probe temperature or dissipated power [32-34].

Method 4 can be combined with Method 1 to thermally measure tip penetration by measuring ΔR_{indent} as each independent indentation in the indentation array is being formed during Method 1. Figure 5.8 shows ΔR_{indent} as a function of T_H for the array of indentations shown in Figure 5.3. The traditionally-measured topographical depth is shown as a function of T_H in Figure 5.3, and comparing Figure 5.3 and Figure 5.8 shows that indentation depth measured from ΔR_{indent} resulted in less noise and a smoother

transition than the topographical depth measurement of Method 1. Measuring indentation depth from ΔR_{indent} also eliminated the need for post-processing, resulting in immediate detection of substrate softening.

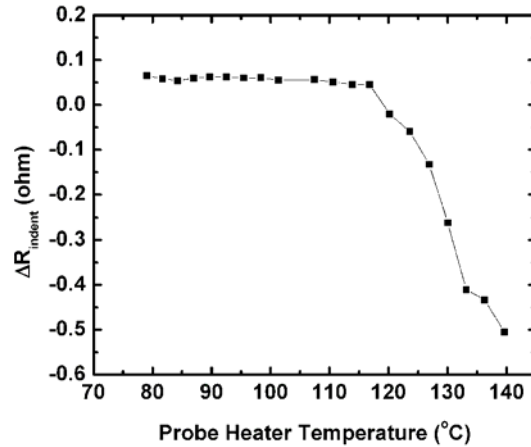


Figure 5.8 ΔR_{indent} as a function of indentation temperature for indentations formed using Method 1. The data shown were taken during the same experiment as that shown in Figure 5.3. Measuring indentation depth from ΔR_{indent} gives a clearer indication of substrate softening than topographical measurement and also eliminates the need for data post-processing.

Figure 5.9 shows a typical nanoTA tip crater left behind after a temperature ramp with a silicon probe, outlined by the approximate size of the ideal LTA crater that would be left by a Wollaston probe. The crater left by the silicon probe is ~200 nm in diameter at its widest point, which is an improvement of two orders of magnitude in sampling resolution and at least 4 orders of magnitude in sampling volume over the Wollaston probe. The ability to clearly detect softening transitions without external hardware using batch fabricated probes with nanoscale imaging and sampling resolution may be important for performing high-throughput, non-destructive LTA.

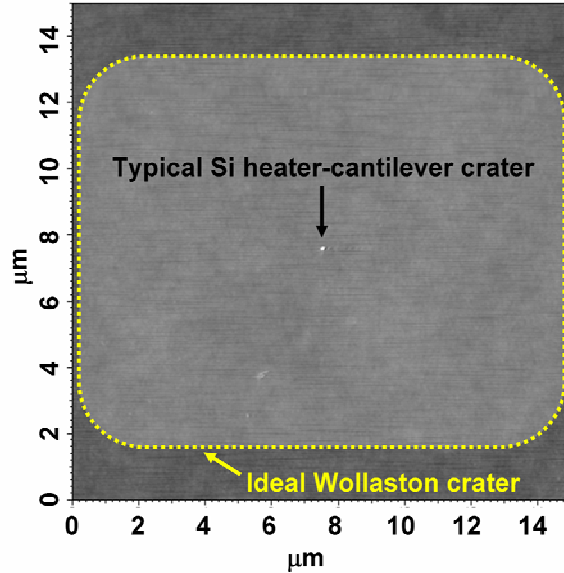


Figure 5.9 Typical tip crater left behind in the PS substrate by a heated silicon probe after performing a temperature ramp. An ideal crater size for a Wollaston probe is shown for reference and is two orders of magnitude larger in linear dimension.

5.4 Discussion

Although the sharp silicon probe tips enable nanoscale spatial resolution, the nanoscale confinement of heat flow also results in difficulties in analyzing experimental results. The PS film had a glass transition temperature of 100 °C, measured by ellipsometry and isothermal uniaxial compression tests, while the measured softening temperatures in Figure 5.3, Figure 5.4, Figure 5.6, Figure 5.7, and Figure 5.8 are close to 120°C. The likely cause of the difference between expected and measured transition temperatures is the thermal contact resistance between the probe and the polymer sample, $R_{contact}$. The temperatures within the tip-substrate thermal circuit shown in Figure 5.2 depend on the relative sizes of $R_{contact}$, R_{tip} , and R_{spread} , since the resistances are in series with one another. To cause a temperature drop of 20 °C at the interface, $R_{contact}$ would have to be 4 times smaller than R_{spread} , neglecting R_{tip} . Assuming that the PS film is think

enough to be treated as a semi-infinite medium, R_{spread} is estimated to be $\sim 4 \times 10^8$ K/W, thus $R_{contact}$ is measured to be $\sim 1 \times 10^8$ K/W. The measured value for $R_{contact}$ is larger than the rough value of $\sim 10^7$ K/W estimated for $R_{contact}$ by assuming diffuse phonon scattering from the crystalline silicon tip into the disordered polymer substrate [28, 35], but is consistent with other estimates [36, 37]. The variation in contact resistances is reasonable given the uncertainties inherent to assuming a macroscale R_{spread} , a simplified phonon scattering model [28], and a Boussinesq contact model [38]. Additionally, just assuming a 17% uncertainty in the spring constant calibration [39] and 10 nm uncertainty in the estimate of the tip radius of curvature can change the ratio of R_{spread} to $R_{contact}$ by a factor of over 4.

The difference between the measured and expected glass transition temperatures could also be due to several other factors. One possibility is a temperature calibration error for the probe. Although temperature calibration errors may contribute in part, the 20 °C temperature difference is larger than would be expected from the ~ 10 °C uncertainty of the Raman spectroscopy technique used in the calibration, described in Chapter 3 and elsewhere [24]. Additionally, the measurement of a transition temperature 20-30 °C higher than the 100 °C bulk transition temperature was verified by several different individually calibrated probes. A calibration error should have a random shift on the apparent transition since the calibration uncertainty is due to drift and uncertain residual stresses, neither of which should result in a systematic bias. Another possible cause of the difference between the measured and expected glass transition temperatures is the high hydrostatic pressure beneath the probe tip, which was on the order of 1 GPa. Such a pressure could elevate T_g over 250 °C [40]. However, such an elevation would

cause a T_g much larger than what was measured by the techniques described in this article. Additionally, the variation in the measured T_g for contact forces ranging from 50-500 nN was within the experimental uncertainty of the measurement. This can be understood by recognizing that the softening must occur in the PS in areas well outside the contact region of the tip before polymer flow would allow the tip to penetrate. The strains in the material should decay rapidly outside the contact region, and thus should exhibit bulk behavior [30]. Confinement effects due to the small thickness of the film are an unlikely cause of the difference between measured and expected transition temperatures because a 170 nm thick PS film should deviate from bulk by less than 1 °C [6, 41].

The offset between T_{int} and T_H could be compensated for when making relative measurements between positions on a sample or between samples with similar thermal conductivity since the effect of $R_{contact}$ should be constant for a given contact force and sample thermal conductivity. However, when comparing LTA on substrates with different thermal resistances or with different contact forces, the degree of offset between T_{int} and T_H can vary. Such variations would make it difficult to measure the spatial variation of phase transitions in the vicinity of composite structures with inhomogeneous thermal properties. In order to understand the accuracy and resolution limits of using silicon probes for thermal analysis, especially in the vicinity of heterogeneities, thermal modeling is required to better understand the mechanisms of heat transfer and their sensitivity to experimental parameters, such as the substrate properties or contact force. Also, although the experiments in this article were performed on flat homogenous samples, modeling efforts are necessary to help determine the effect of heterogeneous

structures and surface topography variation on the accuracy and precision of softening temperature measurements. The modeling can be used to optimize the probe geometry and the ambient medium in which thermal analysis is performed in order to enhance sensitivity to changes in thermal impedance. Such improved understanding is a necessary step towards reliable and quantitative LTA measurements with silicon probes.

The sampling density of nanoTA can be determined from the size of the melted crater left on the substrate after performing thermal analysis. This size is determined by the shape of the tip, the thickness of the sample being tested, and the heating time. The minimum crater size for the experiments performed in this article was about 125 nm, but distinct indentations have been formed in 40 nm thick PMMA films at a pitch of 40 nm with similar probes [26]. Attaching carbon nanotubes at the end of the tip to increase its aspect ratio could further reduce crater size and increase nanoTA sampling density [42]. Even with a crater size of 125 nm for the probes used in this article, results of NanoTA performed with the same probe on a granular organic material suggested that individual grains could be independently sampled, implying that the actual area sampled by the tip was less than $50 \times 50 \text{ nm}^2$ [43]. Heated silicon probes are also a potential tool for characterizing nanoscale confinement effects on melting temperature in crystalline materials. In addition to the PS samples described in this article, NanoTA has also been applied to various organic crystals, and the results have shown a significant depression in melting temperature [17, 43].

5.5 Conclusions

This chapter describes the use of batch-fabricated heated silicon probes to achieve nanoTA. Four parallelizable techniques of performing nanoTA are demonstrated with spatial resolutions between 100 nm and 1 μm , which is 1-2 orders of magnitude improvement over past techniques. Phase transitions are optimally identified from measuring changes to the thermal impedance between the probe and substrate as the tip penetrates into the softened substrate. The development of parallelizable techniques could be used with probe arrays that have previously been operated with similar probes, which could enable high-throughput analysis [22]. The ability to sample with nanoscale spatial resolution and precision enables using nanoTA for characterization of pharmaceuticals, composites, near-surface phenomena, and nanoscale confinement effects over length scales too small to be analyzed by other techniques. A thermal contact resistance exists between the probe tip and the substrate, necessitating further modeling to characterize the uncertainties pertaining to absolute measurements of transition temperatures.

5.6 References

- [1] B. A. Nelson and W. P. King, Measuring material softening with nanoscale spatial resolution using heated silicon probes, *Review of Scientific Instruments*, 78 (2007) 023702.
- [2] R. J. Pylkki, P. J. Moyer and P. E. West, Scanning near-field optical microscopy and scanning thermal microscopy, *Jap. J. Appl. Phys*, 33 (1994) 3785-3790.
- [3] A. Hammiche, L. Bozec, M. Conroy, H. M. Pollock, G. Mills, J. M. R. Weaver, D. M. Price, M. Reading, D. J. Hourston and M. Song, Highly localized thermal,

mechanical, and spectroscopic characterization of polymers using miniaturized thermal probes, *J. Vac. Sci. Technol., B*, 18 (2000) 1322-1332.

[4] A. Hammiche, M. Reading, H. M. Pollock, M. Song and D. J. Hourston, Localized thermal analysis using a miniaturized resistive probe, *Rev. Sci. Instrum.*, 67 (1996) 4268-4273.

[5] H. M. Pollock and A. Hammiche, Micro-thermal analysis: techniques and applications, *J. Phys. D: Appl. Phys.*, 34 (2001) R23-R53.

[6] D. S. Fryer, P. F. Nealey and J. J. de Pablo, Thermal probe measurements of the glass transition temperature for ultrathin polymer films as a function of thickness, *Macromolecules*, 33 (2000) 6439-6447.

[7] R. Hassler and E. zur Muhlen, An introduction to mu TA (TM) and its application to the study of interfaces, *Thermochim. Acta*, 361 (2000) 113-120.

[8] M. S. Tillman, B. S. Hayes and J. C. Seferis, Examination of interphase thermal property variance in glass fiber composites, *Thermochim. Acta*, 392 (2002) 299-302.

[9] C. Blanco, S. Lu, S. P. Appleyard and B. Rand, The stabilisation of carbon fibres studied by micro-thermal analysis, *Carbon*, 41 (2003) 165-171.

[10] T. Grossetete, L. Gonon and V. Verney, Submicrometric characterization of the heterogeneous photooxidation of polypropylene by microthermal analysis, *Polym. Degrad. Stab.*, 78 (2002) 203-210.

[11] D. Q. M. Craig, V. L. Kett, C. S. Andrews and P. G. Royall, Pharmaceutical applications of micro-thermal analysis, *J. Pharm. Sci.*, 91 (2002) 1201-1213.

[12] P. G. Royall, V. L. Kett, C. S. Andrews and D. Q. M. Craig, Identification of crystalline and amorphous regions in low molecular weight materials using microthermal analysis, *J. Phys. Chem. B*, 105 (2001) 7021-7026.

[13] L. Bond, S. Allen, M. C. Davies, C. J. Roberts, A. P. Shivji, S. J. B. Tendler, P. M. Williams and J. X. Zhang, Differential scanning calorimetry and scanning thermal microscopy analysis of pharmaceutical materials, *Int. J. Pharm.*, 243 (2002) 71-82.

- [14] V. V. Tsukruk, V. V. Gorbunov and N. Fuchigami, Microthermal analysis of polymeric materials, *Thermochim. Acta*, 395 (2003) 151-158.
- [15] T. T. Moore and W. J. Koros, Non-ideal effects in organic-inorganic materials for gas separation membranes, *J. Mol. Struct.*, 739 (2005) 87-98.
- [16] M. Alcoutlabi and G. B. McKenna, Effects of confinement on material behaviour at the nanometre size scale, *J. Phys.: Condens. Matter*, 17 (2005) R461-R524.
- [17] W. P. King, S. Saxena, B. A. Nelson, R. Pitchimani and B. L. Weeks, Nanoscale Thermal Analysis of an Energetic Material, *Nano Lett.*, 6 (2006) 2145-2149.
- [18] R. A. Potyrailo, Sensors in combinatorial polymer research, *Macromolecular Rapid Communications*, 25 (2004) 78-94.
- [19] P. Vettiger, G. Cross, M. Despont, U. Drechsler, U. Durig, B. Gotsman, W. Haberle, M. Lantz, H. Rothuizen, R. Stutz and G. Binnig, The "millipede" - nanotechnology entering data storage, *IEEE Trans. Nanotechnology*, 1 (2002) 39-55.
- [20] B. W. Chui, T. D. Stowe, Y. S. Ju, K. E. Goodson, T. W. Kenny, H. J. Mamin, B. D. Terris, R. P. Ried and D. Rugar, Low-stiffness silicon cantilevers with integrated heaters and piezoresistive sensors for high-density AFM thermomechanical data storage, *J. Microelectromech. Syst.*, 7 (1998) 69-78.
- [21] J. Lee, T. Beechem, T. L. Wright, B. A. Nelson, S. Graham and W. P. King, Electrical, Thermal, and Mechanical Characterization of Silicon Microcantilever-Heaters, *J. Microelectromech. Syst.*, 15 (2006) 1644-1655.
- [22] M. Lutwyche, C. Andreoli, G. Binnig, J. Brugger, U. Drechsler, W. Haberle, H. Rohrer, H. Rothuizen, P. Vettiger, G. Yaralioglu and C. Quate, 5X5 2D AFM cantilever arrays a first step towards a Terabit storage device, *Sens. Actuators, A*, 73 (1999) 89-94.
- [23] J. Hutter and J. Bechhoefer, Calibration of atomic-force microscope tips, *Rev. Sci. Instrum.*, 64 (1993) 1868-1873.
- [24] M. R. Abel, T. L. Wright, E. O. Sunden, S. Graham, W. P. King and M. J. Lance, Thermal metrology of silicon microstructures using Raman spectroscopy, *Twenty First Annual IEEE Semiconductor Thermal Measurement and Management Symposium* (2005) 235-242.

- [25] W. P. King, T. W. Kenny and K. E. Goodson, Comparison of thermal and piezoresistive sensing approaches for atomic force microscopy topography measurements, *Appl. Phys. Lett.*, 85 (2004) 2086-2088.
- [26] G. Binnig, M. Despont, U. Drechsler, W. Haberle, M. Lutwyche, P. Vettiger, H. J. Mamin, B. W. Chui and T. W. Kenny, Ultrahigh-density atomic force microscopy data storage with erase capability, *Applied Physics Letters*, 74 (1999) 1329-1331.
- [27] W. P. King, T. W. Kenny, K. E. Goodson, G. Cross, M. Despont, U. Durig, H. Rothuizen, G. K. Binnig and P. Vettiger, Atomic force microscope cantilevers for combined thermomechanical data writing and reading, *Appl. Phys. Lett.*, 78 (2001) 1300-1302.
- [28] W. P. King, *Thermomechanical formation of polymer nanostructures*, Ph.D. thesis, Stanford University, 2002.
- [29] B. Gotsmann and U. Durig, Thermally activated nanowear modes of a polymer surface induced by a heated tip, *Langmuir*, 20 (2004) 1495-1500.
- [30] S. Ge, Y. Pu, W. Zhang, M. Rafailovich, J. Sokolov, C. Buenviaje, R. Buckmaster and R. M. Overney, Shear modulation force microscopy study of near surface glass transition temperatures, *Phys. Rev. Lett.*, 85 (2000) 2340-2343.
- [31] T. Gray, J. Killgore, J. Luo, A. K. Y. Jen and R. M. Overney, Molecular mobility and transitions in complex organic systems studied by shear force microscopy, *Nanotechnology*, 18 (2007) 044009.
- [32] A. Hammiche, D. J. Hourston, H. M. Pollock, M. Reading and M. Song, Scanning thermal microscopy: subsurface imaging, thermal mapping of polymer blends, and localized calorimetry, *J. Vac. Sci. Technol., B*, 14 (1996) 1486-1491.
- [33] J. Lee and Y. B. Gianchandani, A temperature-dithering closed-loop interface circuit for a scanning thermal microscopy system, *J. Microelectromech. Syst.*, 14 (2005) 44-53.
- [34] J.-H. Lee and Y. B. Gianchandani, High-resolution scanning thermal probe with servocontrolled interface circuit for microcalorimetry and other applications, *Rev. Sci. Instrum.*, 75 (2004) 1222-1227.

- [35] E. T. Swartz and R. O. Pohl, Thermal-Boundary Resistance, *Reviews of Modern Physics*, 61 (1989) 605-668.
- [36] D. G. Cahill, W. K. Ford, K. E. Goodson, G. D. Mahan, A. Majumdar, H. J. Maris, R. Merlin and S. R. Phillpot, Nanoscale thermal transport, *J. Appl. Phys.*, 93 (2003) 793-818.
- [37] R. Prasher, Predicting the thermal resistance of nanosized constrictions, *Nano Lett.*, 5 (2005) 2155-2159.
- [38] I. N. Sneddon, The relation between load and penetration in the axisymmetric boussinesq problem for a punch of arbitrary profile, *Int. J. Eng. Sci.*, 3 (1965) 47-57.
- [39] N. Burnham, X. Chen, C. Hodges, G. Matei, E. Thoreson, C. Roberts, M. Davies and S. Tendler, Comparison of calibration methods for atomic-force microscopy cantilevers, *Nanotechnology*, 14 (2003) 1-6.
- [40] J. R. Stevens, R. W. Coakley, K. W. Chau and J. L. Hunt, The Pressure Variation of the Glass-Transition Temperature in Atactic Polystyrene, *J. Chem. Phys.*, 84 (1986) 1006-1014.
- [41] L. Singh, P. J. Ludovice and C. L. Henderson, Influence of molecular weight and film thickness on the glass transition temperature and coefficient of thermal expansion of supported ultrathin polymer films, *Thin Solid Films*, 449 (2004) 231-241.
- [42] M. A. Lantz, B. Gotsmann, U. T. Durig, P. Vettiger, Y. Nakayama, T. Shimizu and H. Tokumoto, Carbon nanotube tips for thermomechanical data storage, *Appl. Phys. Lett.*, 83 (2003) 1266-1268.
- [43] B. A. Nelson and W. P. King, (unpublished)

CHAPTER 6

MODELING AND SIMULATION OF THE INTERFACE TEMPERATURE BETWEEN A HEATED SILICON CANTILEVER TIP AND A SUBSTRATE

This chapter presents an analytical model for the interface temperature between an atomic force microscope (AFM) tip and a substrate. The model closely matches finite difference simulations and includes thermal resistances for the tip, interfacial contact between the tip and substrate, and spreading into the substrate, using an adjusted substrate thermal conductivity for thin film substrates. The thermal and geometrical characteristics of the tip closest to the apex are shown to govern heat transport through the entire tip, necessitating the use of a boundary-constricted thermal conductivity in the analytical model and a separate thermal resistance to treat the geometry at the tip apex. The dependence of the interface temperature on the contact impedance, contact force, and ambient environment thermal conductivity is shown for parameters relevant for silicon AFM tips. The results show that for silicon AFM tips, the substrate and contact thermal resistances dominate the heat transfer. The model identifies dimensionless parameters that govern the interface temperature, which can inform cantilever design and application development, and the model provides a framework that remains capable of incorporating more rigorous estimates of sub-continuum phenomena.

6.1 Introduction

Heated silicon atomic force microscope (AFM) cantilevers, which were shown in Figure 1.2, were originally developed for thermomechanical data storage [1, 2], but have since been used in a number of other applications, including nanolithography [3-7], materials characterization [8-10] and thermophysical property measurement [11, 12]. The temperature rise of the cantilever heater (θ_H) can be calibrated by various methods [2, 13, 14], but in applications where the cantilever tip is in contact with a substrate, the temperature rise at the tip-substrate interface (θ_{int}) is the important parameter. θ_{int} is not generally the same as θ_H [7, 10, 15-17] and cannot be directly calibrated. The difference between θ_H and θ_{int} depends on the relative sizes of the thermal resistances within the tip-substrate system, shown in Figure 6.1. The tip-substrate system includes thermal resistances for the tip, tip-substrate interface, and the substrate itself. A thermal resistance also exists for conduction directly from the cantilever heater to the substrate through the ambient medium (R_{gap}), but the temperature rise in the substrate due to heat transfer from the heater through the gap is small [14, 15].

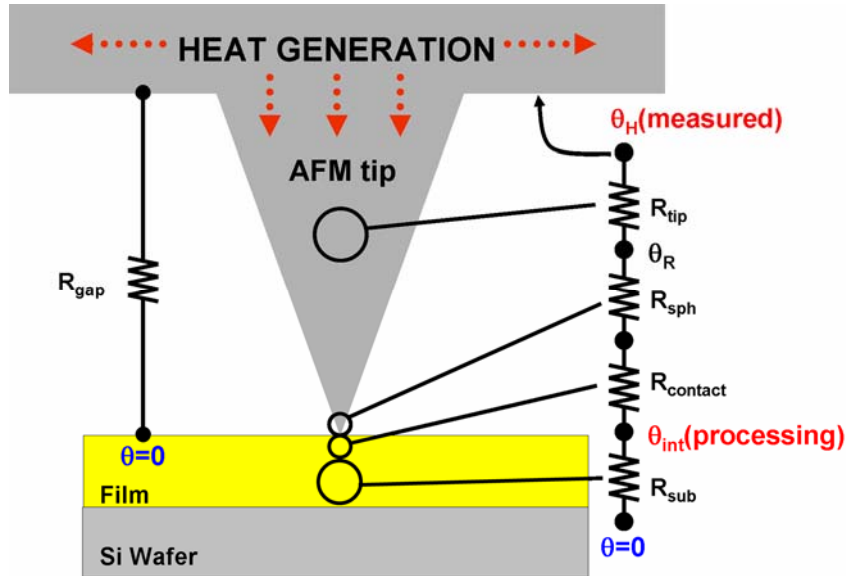


Figure 6.1 Thermal circuit for heat flow through the tip of a heated AFM probe. The temperature rise of the heater platform (θ_H) is the calibrated value, while the temperature rise at the tip-substrate interface (θ_{int}) is the substrate processing temperature. The relative sizes of the thermal resistances of the tip, R_{tip} , tip apex, R_{sph} , interface, $R_{contact}$, and substrate, R_{sub} , determine the relative difference between θ_H and θ_{int} . Heat transfer from the heater to the substrate through the air gap, which has a thermal resistance of R_{gap} , dominates over the heat transfer through the tip, but the primary temperature rise in the substrate occurs under the tip.

Previous work in estimating θ_{int} for heated silicon cantilevers focused on specific tip geometries and substrates. In thermomechanical data storage, θ_{int} was estimated experimentally from the time, temperature, and force thresholds for data bit formation and tip indentation on a polymer substrate [2, 16]. Transient and steady-state numerical simulations studied the data bit formation process and the variation of θ_{int} with loading force, heating time, heater temperature, and tip radius of curvature [15]. Numerical simulations performed for a SiO_2 -based thermocouple AFM probe included thermal transport through a water meniscus around the tip apex and estimates of the solid-solid contact conductance at the tip-substrate interface [18]. Monte Carlo simulations of the rarefied gas conduction from a heated AFM tip implied that substrate thermal processing

could be achieved at small separation without tip-substrate contact [19]. Also, analytical models have been developed for the thermal constriction of contact geometries similar to AFM tips, but the models treat the tip as semi-infinite or isothermal [20, 21].

The experimental results and simulations for heated silicon AFM tips were specific to the cantilever tip geometry and polymer substrate used in the experiments, but other applications of heated AFM cantilevers could have different conditions than that for data storage. The tip geometry can change due to tip wear and process variation across the wafer during fabrication [22, 23]; the tip or tip coatings could be made out of materials other than silicon [3, 17, 24]; biological applications might require liquid environments [25]; contact force and tip wear could change the tip-substrate contact area [10]; and thermal processing could involve substrate materials of various thermal conductivity or thickness [3, 9, 10]. Determining the accuracy of temperature-dependent measurements in heterogeneous environments requires an improved understanding of how θ_{int} varies with the physical parameters of the tip-substrate system. Furthermore, determining the relative sensitivity of θ_{int} to the physical conditions surrounding the tip can enable better experiments by identifying the most relevant parameters affecting θ_{int} .

This paper develops analytical solutions for θ_{int} and the temperature distribution along the cantilever tip. Relevant dimensionless parameters that govern the heat flow through the tip are identified, and the analytical solution is compared to finite-difference simulations.

6.2 Theory and Analytical Model

The tip was modeled as a conical pin with a hemispherical cap at the apex, with radius equal to the radius of curvature of the tip. To generate the solution for θ_{int} , the tip-substrate system was broken up into four parts: conduction thermal resistances for the conical portion of the tip (R_{tip}) and the hemispherical cap at the tip apex (R_{sph}), an interfacial contact resistance ($R_{contact}$), and a thermal spreading resistance into the substrate (R_{sub}). R_{sub} and $R_{contact}$ were identical in the finite difference and analytical models.

6.2.1 Heat Transfer Through the Tip

Heat flow through the tip is constricted by two effects near the end of the tip: reduction of the thermal conductivity due to the small tip diameter, and reduction of the cross-sectional area through which the heat is transferred as the tip tapers towards the apex. In semiconductors and insulators, phonons are the dominant heat carrier and the thermal conductivity is given by

$$k = \frac{1}{3} C v (\Lambda_o^{-1} + d^{-1})^{-1} \quad (6.1)$$

where k is the thermal conductivity of the material, C is the volumetric heat capacity, v is the average phonon speed, Λ_o is the temperature-dependent phonon mean free path in bulk material, d is the diameter of the structure, and the effective phonon mean free path was estimated using Matthiessen's rule [26, 27]. Cv is $\sim 1.8 \times 10^9$ W/m²K and Λ_o is ~ 260 nm for bulk silicon at room temperature [28, 29]. Estimating the thermal

conductivity of silicon nanowires using Eq. (6.1) overpredicts experimental measurements by $\sim 10\%$ [30], while more rigorous estimates based on solutions to the Boltzmann Transport Equation underpredict the experimental measurements by $\sim 10\%$ [30, 31]. Since both methods yield similar estimates of the thermal conductivity, Eq. (6.1) was used here for simplicity. The presence of dopants can also decrease the phonon mean free path, but the effect is negligible for the doping concentration in the tip of $1 \times 10^{17} \text{ cm}^{-3}$ [32, 33].

To better understand the constriction of heat flow through the tip due to the reduction in cross-sectional area, the relative thermal conduction resistance of the conical portion of the tip can be calculated as a function of the tip height through

$$R_{tip}^* = \frac{\int_{2rL/D}^z \frac{dz}{k(z)A(z)}}{\int_{2rL/D}^L \frac{dz}{k(z)A(z)}} = \frac{\frac{3}{2Cvr^2} - \frac{6}{CvD^2z^{*2}} + \frac{2}{k_{tip,o}r} - \frac{4}{k_{tip,o}Dz^*}}{\frac{3}{Cvr^2} \left(\frac{1}{2} - \frac{2r^2}{D^2} \right) + \frac{2}{k_{tip,o}r} \left(1 - \frac{4r}{D} \right)} \quad (6.2a)$$

where z^* is the normalized height along the tip, D is the base diameter of the tip, r is the end radius of a flat-ended conical tip, $k_{tip,o}$ is the temperature-dependent bulk thermal conductivity of the tip, $k(z)$ is the geometry-dependent thermal conductivity, $A(z)$ is the cross-sectional area, and Eq. (6.1) is used to estimate boundary effects on the thermal conductivity. For a tip where boundary scattering has a negligible effect on Λ_{eff} ,

$$R_{tip}^* = \frac{\frac{D}{2r} - \frac{1}{z^*}}{\frac{D}{2r} - 1} \quad (6.2b)$$

Equation (6.2b) would be valid for wide tips or those made from amorphous materials such as polymers or vapor-deposited silicon oxide and nitride. The assumption of one-dimensional heat flow along the axis of the tip in Eqs. (6.2a)-(6.2b) is valid because the thermal resistance to conduction across the tip cross-section is much smaller than the thermal resistance to conduction out the side of the tip to the ambient medium. Figure 6.2 shows R_{tip}^* as a function of z^* with and without boundary scattering for the typical parameters of a silicon AFM tip at room temperature. Over 90% of the total thermal conduction resistance occurs within the first 10% of the tip length, while for a tip with negligible boundary scattering, 80% of the total resistance occurs within the first 20% of the tip length. The thermal properties and geometry near the end of the tip govern heat transport through the entire tip.

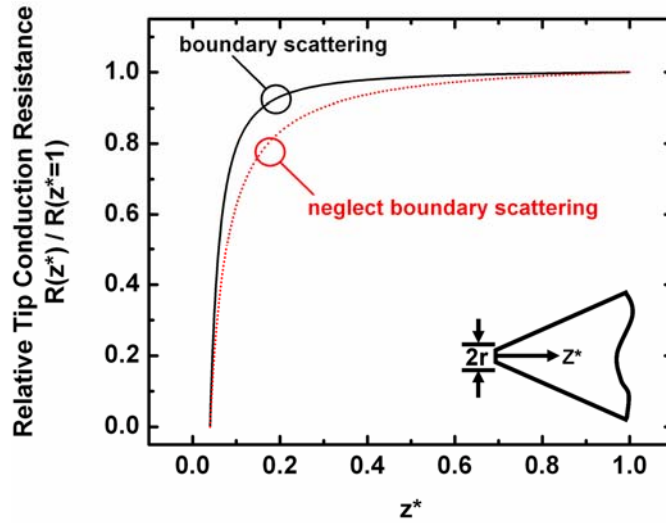


Figure 6.2 Relative conduction thermal resistance of a conical pin as a function of the normalized distance from a flattened apex. The dotted line represents a tip without boundary scattering effects, while the solid line incorporates boundary scattering using Matthiessen's rule for a silicon tip with dimensions similar to our heated AFM cantilevers. The majority of the conduction resistance is localized close to the apex.

The dominance of the thermal properties and geometry at the end of the tip in determining the tip thermal resistance has two implications. First, a separate thermal

resistance is needed to account for the geometry of the hemispherical cap at the end of the tip, and second, the thermal conductivity used in estimating the tip thermal resistance should be the thermal conductivity of the tip material when constricted to the dimensions of the end of the tip, $k_{tip,r}$. The value for $k_{tip,r}$ can be estimated from Eq. (6.1). At the transition from conical to hemispherical profile, the tip diameter is $2r$, which is a size at which the phonon mean free path is dominated by boundary scattering for typical silicon AFM tip parameters. R_{tip} and $k_{tip,r}$ are therefore independent of temperature for typical tip dimensions.

Although Eq. (6.2) indicates that the tip characteristics near the apex dominate the tip thermal conduction resistance, it does not account for conduction from the sides of the tip through the surrounding medium. Including conduction to the ambient yields the general solution for the temperature distribution in the tip

$$\theta(z^*) = \frac{u_1}{u_1 z^*} \left[C_1 I_1(u_1 z^{*1/2}) + C_2 K_1(u_1 z^{*1/2}) \right] \quad (6.3a)$$

where I_1 and K_1 are the first order modified Bessel functions of the first and second kinds, respectively, and u_1 is given by

$$u_1 = \sqrt{\frac{4h_{eff}L^2}{k_{tip,r}D}} \quad (6.3b)$$

where h_{eff} is the effective heat transfer coefficient to the ambient medium and L is the tip height. Using an equivalent thermal resistance to conduction through the ambient medium estimates $h_{eff} \approx \frac{2k_{gap}}{L}$, where k_{gap} is the thermal conductivity of the

ambient medium. The analytical model does not account for rarefaction of the ambient medium, which approaches ballistic transport as the separation distance between the tip sidewall and the substrate is reduced. In the finite difference model, the effective gap thermal conductivity is estimated as [34]

$$\frac{k_{gap,eff}}{k_{gap}} = \left[1 + Kn \frac{2 - \alpha_T}{\alpha_T} \frac{9\gamma - 5}{\gamma + 1} \right]^{-1} \quad (6.4)$$

where $Kn = \frac{\Lambda_{gap}}{z}$ is the Knudsen number, Λ_{gap} is the mean free path of the molecules in the ambient medium, z is the height of the tip sidewall above the substrate, γ is the specific heat ratio of the ambient medium, and α_T is the thermal accommodation coefficient, which was set to 0.9 [18, 35]. Equation (6.4) reduces to fully diffusive transport in the limit of low Kn , and reduces to fully ballistic transport in the case of high Kn . For liquid ambient environments, $k_{gap,eff} = k_{gap}$. The estimate of h_{eff} could incorporate heat transfer due to radiation, but even blackbody radiation is less than 1% of the conduction through the ambient medium for tip surface temperatures below the melting temperature of silicon, 1400 °C. Radiation does not reach 10% of the heat transfer through the ambient medium until the tip surface temperature reaches about 3500 °C.

The boundary conditions for Eq. (6.3) required to satisfy the tip-substrate system are

$$\theta(z^* = 1) = \theta_H \quad (6.5a)$$

and

$$\frac{k_{tip,r}\pi r^2}{L} \frac{d\theta}{dz^*} \Big|_{z^*=\frac{2r}{D}} = \frac{\theta\left(z^* = \frac{2r}{D}\right)}{R_{sub} + R_{contact} + R_{sph}} \quad (6.5b)$$

Equation (6.5b) treats the tip end as having an end diameter equal to twice the radius of curvature of the tip apex to match with the hemispherical cap at the apex. Solution of Eqs. (6.3)-(6.5) yields

$$C_1 = \theta_H \left(\frac{HK_2(u_r) - K_1(u_r)}{HI_1(u_1)K_2(u_r) - I_1(u_1)K_1(u_r) + K_1(u_1)[HI_2(u_r) - I_1(u_r)]} \right) \quad (6.6a)$$

$$C_2 = \theta_H \left(\frac{HI_2(u_r) - I_1(u_r)}{HI_1(u_1)K_2(u_r) - I_1(u_1)K_1(u_r) + K_1(u_1)[HI_2(u_r) - I_1(u_r)]} \right) \quad (6.6b)$$

where

$$H = \left(\frac{R_{sub}}{R_a} + \frac{R_{contact}}{R_a} + \frac{R_{sph}}{R_a} \right) \frac{u_1^2}{2u_r} \quad (6.6c)$$

$$u_r = u_1 \left(\frac{2r}{D} \right)^{1/2} \quad (6.6d)$$

$$R_a = \frac{L}{\pi r^2 k_{tip,r}} \quad (6.6e)$$

R_{tip} can then be defined as

$$R_{tip} = \frac{\theta_H - \theta_R}{q_{tip,out}} = \frac{2R_a u_r^2}{u_1^3 \left[\frac{C_1}{\theta_H} I_2(u_r) - \frac{C_2}{\theta_H} K_2(u_r) \right]} - (R_{sub} + R_{contact} + R_{sph}) \quad (6.7)$$

Comparing Eqs. (6.6a), (6.6b), and (6.7), it is evident that R_{tip} does not depend on θ_H and acts as the thermal resistance within the thermal circuit shown in Figure 6.1. The first term on the right hand side of Eq. (6.7) is R_{total} , the total thermal resistance of the tip-substrate system.

6.2.2 Heat Transfer Through the Tip Apex

As discussed above, a separate thermal resistance was required for the hemispherical cap at the apex of the tip to account for the hemispherical geometry. In the finite difference model, the curved tip apex was merged smoothly with the conical tip profile by matching the derivatives of the sidewall profiles of the cone and hemisphere, so the apex of the tip was smaller than a full hemisphere. The analytical model capped the conical profile of the tip with a full hemispherical apex, treating heat conduction in the hemisphere as one-dimensional in Cartesian coordinates and neglecting the gradual transition to radial heat flow as the tip diameter narrowed. The model also neglected conduction to the ambient medium from the tip surface. For the described conditions, R_{sph} is equal to

$$R_{sph} = \frac{1}{k_{sph}\pi r} \tanh^{-1}\left(1 - \frac{b}{r}\right) \quad (6.8)$$

where k_{sph} is the thermal conductivity of the hemispherical cap and is not necessarily the same as $k_{tip,r}$, and b is the penetration depth of the tip into a soft substrate, which can be determined from [36]

$$\frac{b}{r} = \frac{1}{2}c \ln\left(\frac{1+c}{1-c}\right) \quad (6.9a)$$

where c is determined from

$$F = \frac{G_{sub} r}{1 - \eta} \left[(c^2 + 1) \cdot \ln \left(\frac{1 + c}{1 - c} \right) - c \right] \quad (6.9b)$$

where F is the contact force, G_{sub} is the shear modulus of the substrate, and η is Poisson's ratio for the substrate. For hard substrates with negligible penetration depth, $\frac{b}{r}$

in Eq. (6.8) should be replaced by $\left[1 - \sqrt{1 - \left(\frac{a}{2r} \right)^2} \right]$, where a is the contact diameter

between the tip and substrate and can be estimated from relevant contact mechanics models [37]. Equation 6.8 neglects the thermal conduction resistance within the submerged part of the penetrated tip, which was negligible compared to $R_{contact}$ and R_{sub} for a typical AFM contact. For AFM tips that are flattened by wear or incomplete oxide sharpening, R_{sph} is no longer relevant and can be excluded from the thermal circuit of

Figure 6.1. Equation (6.6d) would then become $u_r = u_1 \left(\frac{a}{D} \right)^{1/2}$, where the contact diameter a is set equal to the diameter of the flattened end of the tip.

6.2.3 Heat Transfer Through the Interface

An interfacial contact thermal resistance occurs at the tip-substrate interface due to the acoustic property mismatch between the materials [20, 38-40]. The interfacial resistance can be estimated as

$$R_{contact} = \frac{4R_b}{\pi a^2} \quad (6.10)$$

where R_b is the thermal boundary resistance and has the same units as the bulk thermal contact resistance [41]. Models for predicting R_b have limited accuracy above cryogenic temperatures [42], but experimental measurements of R_b for solid-solid contacts near room temperature do not vary significantly with the contacting materials and typically range from 5×10^{-9} - 5×10^{-8} m²K/W [10, 39, 43]. For tip penetration into a soft substrate, the effective contact diameter can be estimated as

$$a = \sqrt{8rb} \quad (6.11)$$

where b is determined from Eq. (6.9). Validity of Eq. (6.11) requires that $b \ll t_{sub}$.

6.2.4 Heat Transfer Through the Substrate

The contact of the spherical apex of the heated AFM tip onto a flat substrate can be approximated as a circular heat source in contact with a flat, homogeneous semi-infinite substrate, which has a thermal resistance given by [41]

$$R_{sub,o} = \frac{1}{2k_{sub,o}a} \quad (6.12)$$

where $k_{sub,o}$ is the bulk substrate thermal conductivity. Equation (6.12) is valid for semi-infinite substrates but not for the thin film substrates often used in conjunction with heated AFM tips [2, 10]. Film thickness can be accounted for using a full analytical solution for the thermal resistance of a rectangular heat source on a flat substrate of finite thickness with an ambient temperature boundary condition on the bottom side [44]. The boundary conditions of the solution closely approximate the geometry for a heated AFM

tip because the ambient temperature boundary condition is approximately true for a low thermal conductivity thin film on a silicon substrate [2, 10, 18], and the thermal resistances for square and circular contacts on semi-infinite substrates are nearly equal for area-equivalent dimensions. The ratio of the thermal resistance of a substrate of finite thickness (R_{sub}) to that in Eq. (6.12) is given by

$$\frac{R_{sub}}{R_{sub,o}} = \frac{4}{\pi^{5/2}} \int_0^{\infty} \int_0^{\infty} \frac{\sin \alpha \sin \beta \tanh\left(\frac{t_{sub}}{a} \frac{2}{\sqrt{\pi}} \sqrt{\alpha^2 + \beta^2}\right) d\alpha d\beta}{\sqrt{\alpha^2 + \beta^2}} \quad (6.13)$$

where t_{sub} is the substrate film thickness. An effective thermal conductivity can then replace $k_{sub,o}$ in Eq. (6.12) and is defined as

$$k_{sub} = k_{sub,o} \left[\frac{R_{sub}}{R_{sub,o}} \right]^{-1} \quad (6.14)$$

Figure 6.3 shows the results of Eq. (6.13) as a function of the dimensionless ratio $\frac{t_{sub}}{a}$. When $\frac{t_{sub}}{a} > 10$, the bulk and thin film thermal resistances are nearly equivalent and $k_{sub} = k_{sub,o}$.

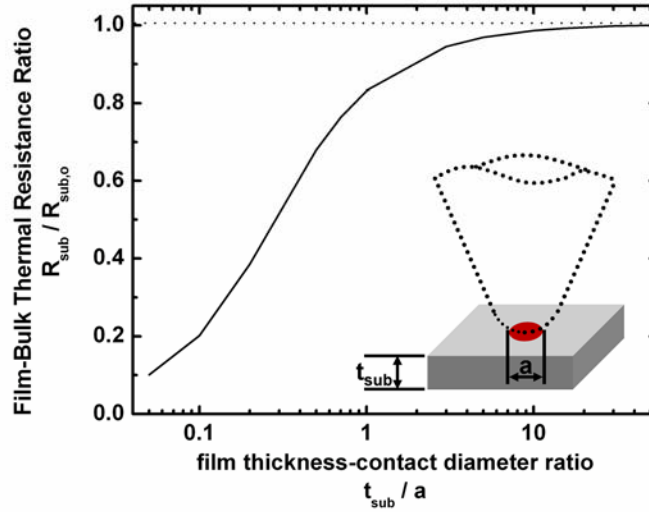


Figure 6.3 Thin film-bulk substrate thermal resistance ratio as a function of the film thickness to contact diameter ratio. Above a ratio of ~ 10 , film thickness has a negligible effect on the thermal resistance.

6.2.5 Summary of Relevant Dimensionless Numbers

Using the thermal circuit in Figure 6.1, a dimensionless interface temperature can be defined as

$$\theta_{int}^* = \frac{\theta_{int}}{\theta_H} = \frac{R_{sub}}{R_{total}} = \frac{R_{sub}}{R_a} f\left(u_1, u_r, \frac{R_{sph}}{R_a}, \frac{R_{contact}}{R_a}, \frac{R_{sub}}{R_a}\right) \quad (6.15)$$

where the functional form of f is given by Eqs. (6.6)-(6.7). Substituting geometrical and thermal properties from the previous equations, θ_{int}^* is governed by the set of dimensionless parameters

$$\theta_{int}^* = \theta_{int}^* \left(\frac{k_{sub}}{k_{tip,r}}, \frac{R_b k_{tip,r}}{r}, \frac{k_{gap}}{k_{tip,r}}, \frac{D}{r}, \frac{b}{r}, \frac{L}{r} \right) \quad (6.16)$$

For hard substrates with negligible tip penetration, $\frac{a}{r}$ replaces $\frac{b}{r}$.

6.3 Results and Discussion

The analytical predictions of θ_{int}^* given by Eq. (6.15) were compared to finite difference simulations of heat transport through the tip, which have shown reasonable agreement with experimental measurements for heated silicon AFM tips [15]. Unless otherwise noted, all simulations were performed using the parameters listed in Table 6.1, which correspond to values typical for a silicon AFM tip in contact with a polymer substrate. In the simulations, all dimensionless parameters in Eq. (6.16) were held constant except for those explicitly varied. Results of the finite difference solutions were verified to be governed by the dimensionless ratios identified in Eq. (6.16) rather than the values of the individual physical and geometrical properties of the tip and substrate. The finite difference model was validated by balancing energy, checking against analytical solutions, and refining the discretization mesh without changes in the solution.

Table 6.1. Standard values used for non-dimensional parameters, unless otherwise noted.

Name	Label	Std. Value
tip base diameter	D	1×10^{-6} m
tip height	L	1.5×10^{-6} m
tip radius of curvature	r	20×10^{-9} m
Penetration depth	b	from Eq. (6.9a)-(6.9b)
Interfacial impedance	R_b	1×10^{-8} m ² *K/W
contact force	F	300 nN
tip thermal conductivity at width r	$k_{tip,r}$	from Eq. (6.1)
Substrate thermal conductivity	k_{sub}	0.1 W/m*K

6.3.1 Contact Impedance Effect on Interface Temperature

R_b can only be estimated with limited certainty, so the variation of θ_{int}^* with different estimates of R_b needed to be examined. Figure 6.4 shows analytical and finite difference predictions of θ_{int}^* as a function of $\frac{k_{sub}}{k_{tip,r}}$ for varying $\frac{R_b k_{tip,r}}{r}$. The listed values of R_b assume a typical silicon AFM tip and correspond to the bounds of reported and estimated values [15, 39, 40, 43]. The analytical model closely matches the finite difference simulations.

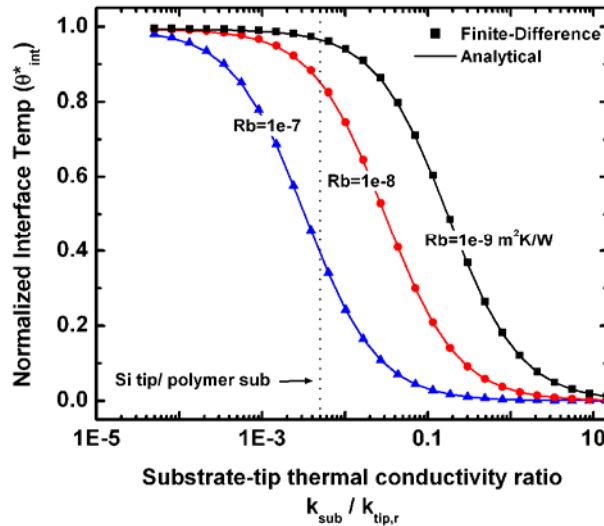


Figure 6.4 Normalized interface temperature as a function of the ratio between the tip and substrate thermal conductivities for different values of $\frac{R_b k_{tip,r}}{r}$. The labels represent the corresponding values of R_b for a typical silicon AFM tip. The analytical model agrees with the simulation data points within $\sim 2\%$. θ_{int}^* depends strongly on the assumed value for R_b within the range of reported interface resistance values.

The sum of R_{tip} , R_{sph} , and $R_{contact}$ dominates R_{total} for $\frac{k_{sub}}{k_{tip,r}} > 1$ and minimal temperature rise occurs on the substrate surface. θ_{int}^* starts to rise as R_{sub} becomes

significant, which occurs at $\frac{k_{sub}}{k_{tip,r}} < .005$ for typical values of $\frac{R_b k_{tip,r}}{r}$. Directly comparing the analytical model to experimental data was difficult due to uncertainty in estimating R_b , but comparison of Figure 6.4 with experimental measurements of the softening temperature of polystyrene estimates $R_b \approx 1 \times 10^{-8} \text{ m}^2\text{K/W}$, which is consistent with previously reported values [10, 18, 39, 40, 43]. Although $R_{contact}$ and R_{sub} dominate R_{total} for values of $\frac{R_b k_{tip,r}}{r}$ typical of AFM tips, the analytical model was verified to match the finite difference results for unphysically low values of $\frac{R_b k_{tip,r}}{r}$ in which R_{tip} and R_{sph} contributed more significantly to R_{total} .

6.3.2 Contact Force Effect on Interface Temperature

Contact force can be difficult to control when heating silicon cantilevers due to thermally-induced bending and temperature-dependent stiffness in the cantilever legs [10, 13, 45], so understanding the dependence of θ_{int}^* on the contact force is important. For soft substrates, where the elastic modulus of the tip is much larger than the elastic modulus of the substrate, the contact force affects θ_{int}^* through the penetration depth while for hard substrates, where the elastic moduli of the tip and substrate are similar, the contact force affects θ_{int}^* through the contact diameter. Figure 6.5 shows the dependence of θ_{int}^* on $\frac{k_{sub}}{k_{tip,r}}$ for varying $\frac{b}{r}$ and $\frac{a}{r}$ for soft and hard substrates, respectively. The plotted values of $\frac{b}{r}$ and $\frac{a}{r}$ correspond to the penetration depths and contact diameters

typical for a silicon AFM tip on polymer and silicon substrates, respectively, at the specified contact forces. As the contact force increases, $R_{contact}$ decreases relative to R_{sub} and θ_{int}^* increases. Figure 6.5 shows that θ_{int}^* depends strongly on contact force below 500 nN for polymer substrates and was insensitive to contact force on hard substrates. The sensitivity to contact force on soft substrates is in contrast to previously reported results for thermal characterization of polymer substrates, for which the AFM-measured softening temperature of polystyrene was insensitive to the contact force [10]. The discrepancy may be due to the requirement for heat to diffuse through the polymer surrounding the tip before tip motion into the substrate was detectable [15]. However, the results imply that temperature-dependent measurements on soft substrates require careful control of the contact force [10]. Since θ_{int}^* was insensitive to the contact force on hard substrates, increasing the contact force cannot compensate for the low values of θ_{int}^* on high thermal conductivity substrates, which suggests that heated cantilevers cannot perform thermal processing on hard substrates for $\frac{k_{sub}}{k_{tip,r}} > .05$. Silicon cantilevers therefore require very high temperatures and contact forces when used with silicon and metal substrates, which is consistent with previous experimental results [3].

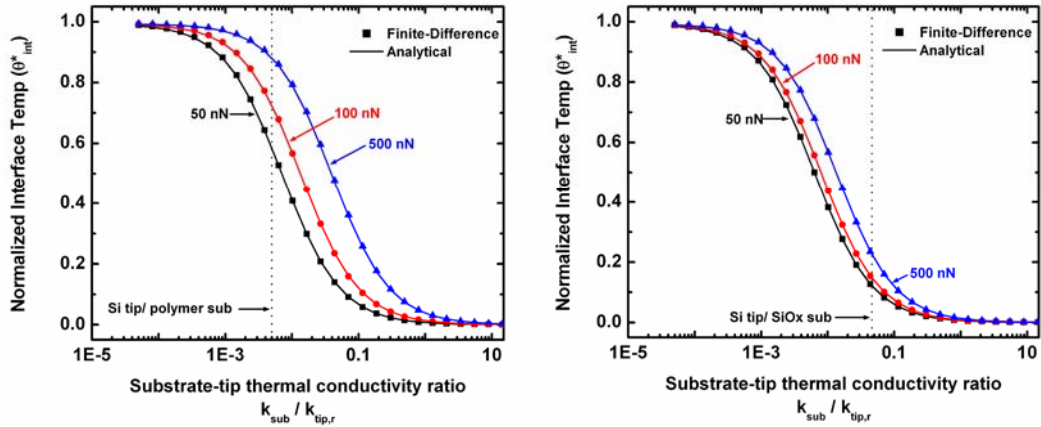


Figure 6.5 Normalized interface temperature as a function of the ratio between the tip and substrate thermal conductivities for a soft polymer substrate with different values of b/r (top) and for a hard silicon substrate with different values of a/r assuming Hertzian contact (bottom). The labels represent the corresponding values of F for a silicon tip on the given substrate with typical AFM tip dimensions. The analytical model agrees with the simulation data points within $\sim 2\%$. θ_{int}^* depends more strongly on F for soft substrates and contact forces below 500 nN, but has a weak dependence on F for hard substrates.

6.3.3 Ambient Environment Effect on Interface Temperature

Although all reported uses of heated silicon cantilevers have been in either air or vacuum [11], other applications of the cantilevers could utilize other gas environments to prevent oxidation of working materials [3] or aqueous environments to enable biological measurements [25]. The validity of the analytical model of Eq. (6.15) was evaluated for

different ambient environments by setting $\frac{k_{gap}}{k_{tip,r}}$ equal to the values for air, helium and

water with a silicon tip, and Figure 6.6 shows the results. The finite difference simulations for air and helium are nearly identical, implying that conduction to gaseous media has a negligible effect on θ_{int}^* , although conduction to the ambient becomes significant for a water ambient environment.

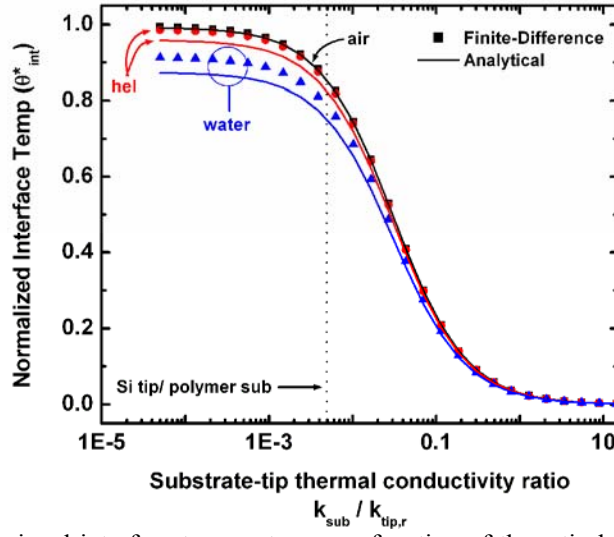


Figure 6.6 Nondimensional interface temperature as a function of the ratio between the tip and substrate thermal conductivities for different values of $\frac{k_{gap}}{k_{tip,r}}$. The lines correspond to the analytical predictions while the data points correspond to finite difference simulation results. The analytical model loses accuracy for values of $\frac{k_{gap}}{k_{tip,r}}$ above ~ 0.01 , but remains within $\sim 5\%$ of finite difference simulations. Conduction to the ambient has a negligible effect on θ_{int}^* unless the ambient is a liquid.

The analytical model loses some accuracy as $\frac{k_{gap}}{k_{tip,r}}$ increases above ~ 0.01 . The loss in accuracy was caused by two factors: neglecting conduction to the ambient in deriving Eq. (6.8) which underestimates R_{sph} , and the crude approximation for h_{eff} in Eq. (6.3b) which overestimates R_{tip} . Since Figure 6.6 shows that the analytical model underpredicts the finite difference simulations for θ_{int}^* , the overprediction of h_{eff} is the primary cause of inaccuracy in the analytical model for $\frac{k_{sub}}{k_{tip,r}} < 0.005$, which corresponds to a silicon AFM tip on a polymer substrate. For $\frac{k_{sub}}{k_{tip,r}} > 0.005$, the overprediction of R_{tip}

nearly compensates for the underprediction of R_{sph} and the analytical predictions of θ_{int}^* remain close to the finite difference simulations. Despite the loss in accuracy for higher values of $\frac{k_{gap}}{k_{tip,r}}$, the analytical model provides a reasonable approximation of θ_{int}^* and remains within 5% of the finite difference simulations even for a water environment.

6.3.4 Additional Comments

Significant uncertainty exists surrounding estimates of the properties in the analytical model affected by sub-continuum phenomena, such as $k_{gap,eff}$, $k_{tip,r}$, and R_b , but the model allows direct incorporation of more rigorous estimates of these properties. Additionally, for applications such as nanothermal analysis [10], the values of $k_{gap,eff}$, $k_{tip,r}$, and R_b are only important in how they affect the sensitivity of θ_{int}^* to variations in substrate and geometrical properties and thus reasonable estimates of their magnitudes are sufficient. Estimates of R_b could potentially be improved by using the heated silicon cantilever to measure R_b on various substrates above room temperature, for which minimal data exists [40].

6.4 Conclusions

This paper describes an analytical model to determine the temperature at the interface between a heated AFM tip and a substrate and compares the results to finite difference simulations. The model incorporates arbitrary materials, tip sharpness, film thickness, and ambient environments and identifies a number of dimensionless ratios that

modulate the interface temperature. The thermal and geometrical characteristics at the apex of the heated AFM tip dominate the total heat transfer through the tip, and analytical predictions incorporating the constricted thermal conductivity near the end of the tip closely match the finite difference simulations. Some loss of accuracy in the analytical model results for ambient environments with high thermal conductivity but remains within 5% of the finite difference simulations. Although the analytical model described in this paper utilized rough approximations for sub-continuum phenomena, more rigorous estimates of these effects could be directly incorporated into the parameters of the model. Additionally, the solution for the thermal resistance of the tip could be coupled with electrical sensitivity measurements to estimate the fundamental detection limits of heat flow through the tip, which could be important in calorimetric applications.

6.5 References

- [1] G. Binnig, M. Despont, U. Drechsler, W. Haberle, M. Lutwyche, P. Vettiger, H. J. Mamin, B. W. Chui and T. W. Kenny, Ultrahigh-density atomic force microscopy data storage with erase capability, *Applied Physics Letters*, 74 (1999) 1329-1331.

- [2] P. Vettiger, G. Cross, M. Despont, U. Drechsler, U. Durig, B. Gotsman, W. Haberle, M. Lantz, H. Rothuizen, R. Stutz and G. Binnig, The "millipede" - nanotechnology entering data storage, *IEEE Transactions on Nanotechnology*, 1 (2002) 39-55.

- [3] B. A. Nelson, W. P. King, A. R. Laracuenta, P. E. Sheehan and L. J. Whitman, Direct deposition of continuous metal nanostructures by thermal dip-pen nanolithography, *Applied Physics Letters*, 88 (2006) 033104.

- [4] P. E. Sheehan, L. J. Whitman, W. P. King and B. A. Nelson, Nanoscale deposition of solid inks via thermal dip pen nanolithography, *Applied Physics Letters*, 85 (2004) 1589-1591.

- [5] M. Yang, P. E. Sheehan, W. P. King and L. J. Whitman, Direct writing of a conducting polymer with molecular-level control of physical dimensions and orientation, *Journal of the American Chemical Society*, 128 (2006) 6774-6775.
- [6] S. Bakbak, P. J. Leech, B. E. Carson, S. Saxena, W. P. King and U. H. F. Bunz, 1,3-dipolar cycloaddition for the generation of nanostructured semiconductors by heated probe tips, *Macromolecules*, 39 (2006) 6793-6795.
- [7] B. Gotsmann, U. Duerig, J. Frommer and C. J. Hawker, Exploiting chemical switching in a Diels-Alder polymer for nanoscale probe lithography and data storage, *Advanced Functional Materials*, 16 (2006) 1499-1505.
- [8] W. Haeberle, M. Pantea and J. K. H. Hoerber, Nanometer-scale heat-conductivity measurements on biological samples, *Ultramicroscopy*, 106 (2006) 678-686.
- [9] W. P. King, S. Saxena, B. A. Nelson, R. Pitchimani and B. L. Weeks, Nanoscale Thermal Analysis of an Energetic Material, *Nano Letters*, 6 (2006) 2145-2149.
- [10] B. A. Nelson and W. P. King, Measuring material softening with nanoscale spatial resolution using heated silicon probes, *Review of Scientific Instruments*, 78 (2007) 023702.
- [11] J. Lee, T. L. Wright, M. R. Abel, E. O. Sunden, A. Marchenkov, S. Graham and W. P. King, Thermal conduction from microcantilever heaters in partial vacuum, *Journal of Applied Physics*, 101 (2007) 014906.
- [12] B. Gotsmann and U. Durig, Experimental observation of attractive and repulsive thermal forces on microcantilevers, *Applied Physics Letters*, 87 (2005) 194102.
- [13] J. Lee, T. Beechem, T. L. Wright, B. A. Nelson, S. Graham and W. P. King, Electrical, Thermal, and Mechanical Characterization of Silicon Microcantilever-Heaters, *Journal of Microelectromechanical Systems*, 15 (2006) 1644-1655.
- [14] B. A. Nelson and W. P. King, Temperature Calibration of Heated Silicon Atomic Force Microscope Cantilevers, *Sensors and Actuators, A: Physical*, (2007-submitted)
- [15] W. P. King and K. E. Goodson, Thermomechanical formation of nanoscale polymer indents with a heated silicon tip, *Journal of Heat Transfer*, (2007-in press)

- [16] B. Gotsmann and U. Durig, Thermally activated nanowear modes of a polymer surface induced by a heated tip, *Langmuir*, 20 (2004) 1495-1500.
- [17] M. A. Lantz, B. Gotsmann, U. T. Durig, P. Vettiger, Y. Nakayama, T. Shimizu and H. Tokumoto, Carbon nanotube tips for thermomechanical data storage, *Applied Physics Letters*, 83 (2003) 1266-1268.
- [18] L. Shi and A. Majumdar, Thermal transport mechanisms at nanoscale point contacts, *Journal of Heat Transfer-Transactions of the Asme*, 124 (2002) 329-337.
- [19] P. O. Chapuis, J. J. Greffet, K. Joulain and S. Volz, Heat transfer between a nanotip and a surface, *Nanotechnology*, 17 (2006) 2978-2981.
- [20] R. Prasher, Predicting the thermal resistance of nanosized constrictions, *Nano Letters*, 5 (2005) 2155-2159.
- [21] V. Bahadur, J. Xu, Y. Liu and T. S. Fisher, Thermal resistance of nanowire-plane interfaces, *Journal of Heat Transfer-Transactions of the Asme*, 127 (2005) 664-668.
- [22] H. J. Mamin, R. P. Ried, B. D. Terris and D. Rugar, High-density data storage based on the atomic force microscope, *Proceedings of the IEEE*, 87 (1999) 1014-1027.
- [23] B. D. Terris, S. A. Rishton, H. J. Mamin, R. P. Ried and D. Rugar, Atomic force microscope-based data storage: track servo and wear study, *Applied Physics a-Materials Science & Processing*, 66 (1998) S809-S813.
- [24] J. H. Bae, T. Ono and M. Esashi, Scanning probe with an integrated diamond heater element for nanolithography, *Applied Physics Letters*, 82 (2003) 814.
- [25] M.-H. Li and Y. B. Gianchandani, Applications of a low contact force polyimide shank bolometer probe for chemical and biological diagnostics, *Sensors and Actuators A*, 104 (2003) 236-245.
- [26] H. B. G. Casimir, Note on the conduction of heat in crystals, *Physica*, 5 (1938) 495-500.
- [27] N. W. Ashcroft and N. D. Mermin, *Solid State Physics*, Harcourt College Publishers, Orlando, FL, 1976.

- [28] Y. S. Ju, Phonon heat transport in silicon nanostructures, *Applied Physics Letters*, 87 (2005) 153106.
- [29] G. Chen, Thermal conductivity and ballistic-phonon transport in the cross-plane direction of superlattices, *Physical Review B*, 57 (1998) 14958-14973.
- [30] D. Y. Li, Y. Y. Wu, P. Kim, L. Shi, P. D. Yang and A. Majumdar, Thermal conductivity of individual silicon nanowires, *Applied Physics Letters*, 83 (2003) 2934-2936.
- [31] W. J. Liu and M. Asheghi, Thermal conductivity measurements of ultra-thin single crystal silicon layers, *Journal of Heat Transfer-Transactions of the Asme*, 128 (2006) 75-83.
- [32] M. Asheghi, K. Kurabayashi, R. Kasnavi and K. E. Goodson, Thermal conduction in doped single-crystal silicon films, *Journal of Applied Physics*, 91 (2002) 5079-5088.
- [33] W. J. Liu and M. Asheghi, Thermal conduction in ultrathin pure and doped single-crystal silicon layers at high temperatures, *Journal of Applied Physics*, 98 (2005) 123523.
- [34] Z. M. Zhang, *Nano/Microscale Heat Transfer*, McGraw Hill, New York, 1997-in press.
- [35] Z. M. Zhang, *Nano/Microscale Heat Transfer*, McGraw Hill, New York, 2007.
- [36] I. N. Sneddon, The relation between load and penetration in the axisymmetric boussinesq problem for a punch of arbitrary profile, *International Journal of Engineering Science*, 3 (1965) 47-57.
- [37] K. L. Johnson, *Contact mechanics*, Cambridge University Press, Cambridge [Cambridgeshire] ; New York, 1987.
- [38] E. T. Swartz and R. O. Pohl, Thermal-Boundary Resistance, *Reviews of Modern Physics*, 61 (1989) 605-668.
- [39] R. J. Stoner and H. J. Maris, Kapitza Conductance and Heat-Flow between Solids at Temperatures from 50 to 300 K, *Physical Review B*, 48 (1993) 16373-16387.

- [40] D. G. Cahill, W. K. Ford, K. E. Goodson, G. D. Mahan, A. Majumdar, H. J. Maris, R. Merlin and S. R. Phillpot, Nanoscale thermal transport, *Journal of Applied Physics*, 93 (2003) 793-818.
- [41] F. P. Incropera and D. P. DeWitt, *Fundamentals of Heat and Mass Transfer*, Wiley, New York, 5th edn., 2002.
- [42] D. G. Cahill, Heat transport in dielectric thin films and at solid-solid interfaces, *Microscale Thermophysical Engineering*, 1 (1997) 85-109.
- [43] T. Beechem, S. Graham, P. Hopkins and P. Norris, Role of Interface Disorder on Thermal Boundary Conductance Using a Virtual Crystal Approach, *Applied Physics Letters*, 90 (2007) 054104.
- [44] A. L. Palisoc and C. C. Lee, Thermal-Properties of the Multilayer Infinite-Plate Structure, *Journal of Applied Physics*, 64 (1988) 410-415.
- [45] U. Gysin, S. Rast, P. Ruff, E. Meyer, D. W. Lee, P. Vettiger and C. Gerber, Temperature dependence of the force sensitivity of silicon cantilevers, *Physical Review B*, 69 (2004)

CHAPTER 7

SUMMARY AND RECOMMENDATIONS

7.1 Summary

This work presented two thrusts of research to advance the current state of use of silicon heated AFM cantilevers. The first thrust improved the potential accuracy and precision of temperature-dependent measurements by developing and optimizing experimental and theoretical characterization tools for the cantilever behavior. The second thrust developed new applications for the cantilevers that capitalized on their advantages over other heated AFM probes in cost, lateral resolution, and parallelizability.

The first step in improving the accuracy of temperature-dependent measurements using heated silicon cantilevers was analyzing and optimizing their electrical and thermal calibration. Accuracy limits for each of the thermal calibration techniques were identified and a full calibration methodology for precision use of the cantilevers was proposed and verified through measurements of calibration stability and finite difference heat transfer simulations. Thermal calibrations were shown to be stable with time and cantilever usage, and Raman spectroscopy was identified as the most accurate calibration technique. In another step to improve the accuracy of temperature-dependent measurements, an analytical model was developed for heat transfer through the cantilever tip. The model could incorporate arbitrary tip and substrate materials and geometries and identified the dimensionless ratios and key properties that govern heat transport through the tip and control the tip-substrate interface temperature. The tip characteristics closest

to the apex were shown to dominate the thermal resistance of the entire tip. The results showed that heated silicon cantilevers require extreme temperatures and contact forces to significantly raise the surface temperature of metal and silicon substrates.

Two new applications utilizing heated silicon cantilevers were also demonstrated. In the first application, controllable and localized deposition of metal from the AFM tip was demonstrated. Thermal modulation of the deposition process allowed the cantilever tip to maintain its full functionality for topographical imaging. The electrical continuity of the deposited metal structure was measured, which was the first electrical test of an AFM-deposited structure. In the second application, characterizing substrate softening temperatures with nanoscale spatial resolution was demonstrated by using the heated AFM tip to induce softening. Several detection techniques were described, all of which were parallelizable and could thus be utilized with cantilever arrays. Several orders of magnitude of improvement in sampling resolution over previous results with metallic heater cantilevers was achieved by using silicon cantilevers.

7.2 Recommendations and Future Research

This plan for future research continues to work toward capitalizing on the capabilities of heated silicon cantilevers as an industrial and research tool. Research is suggested both in refining the experimental and theoretical characterization for the cantilevers, and also in continuing to develop applications for the cantilevers. Developing applications includes both the introduction of new applications, and also the advancement of the applications described within this work into their end goals. Characterization and application development are inter-related, for as further applications

arise, new or more stringent characterization requirements will arise as well. Figure 7.1 overviews the proposed research.

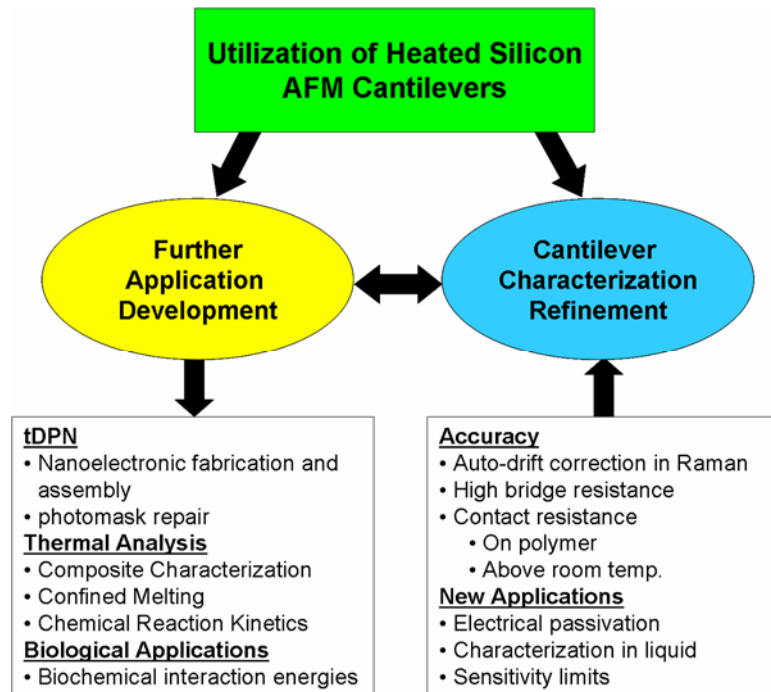


Figure 7.1 Overview of future research directions.

7.2.1 Application Development

The applications for heated silicon cantilevers described in this work represent the initial development of techniques that have applications beyond what has been described already. Thermal dip-pen nanolithography (tDPN) could be used for fabricating entire nanoelectronic circuits, where polymeric or self-assembled monolayer glues anchor nanoelectronics components onto a substrate [1], metallic deposition creates electrical connections between electrodes and components [2], and semiconducting polymers and nanostructures could be integrated to create active devices [3]. tDPN could also be used to locate and repair defects in lithographic photomasks [2, 4].

Techniques were shown for detecting tip penetration during nano-thermal analysis (NanoTA), but the ultimate goal of NanoTA is measuring and distinguishing between

softening temperatures with high spatial localization. Such measurements enable fundamental investigations of material interactions within composites and other heterogeneous structures [5, 6]. The techniques also allow using the heated AFM tip to measure the thermodynamics of melting within confined geometries [7, 8]. The development of an analytical model for the thermal resistance of the tip also could enable true calorimetry beneath the tip, enabling measurements of chemical reaction thermodynamics and kinetics [8].

In biology, the heated silicon tip could measure the temperature-dependence of biomolecular interactions, enabling new methods of measuring interaction energies [9]. The tip can also act as an interrogation tool for individual organelles and other cellular structures, where the effects of heat can be examined on localized cell functions such as enzyme activity, protein synthesis, genetic transcription, cell metabolism, and active transport [10].

7.2.2 Cantilever Characterization Refinement

Refinement of the cantilever characterization techniques described in this work would lead to greater accuracy when using heated silicon cantilevers, and is also necessary for enabling new types of applications for the cantilevers.

7.2.2.1 Accuracy Improvement

The first step for improving the accuracy of using heated silicon cantilevers is increasing the accuracy of the initial characterization of the cantilever heater temperature. Integration of automatic drift correction algorithms into a Raman microscope would eliminate most of the calibration uncertainty at temperatures below ~ 150 °C for

calibration from the Stokes peak position, and would also make calibration from the Stokes peak width practically feasible by enabling automation of spectra acquisition. Alternately, fabricating probes with a larger portion of the cantilever resistance concentration in the low-doped portion would eliminate the need for Raman microscopy by eliminating most of the error associated with isothermal temperature calibrations. Although increasing the relative resistance of the low-doped region adversely affects the utility of the cantilevers for high-speed or array operation, many potential applications utilizing the cantilevers as a measurement device are limited more by temperature accuracy than cantilever heating time or power requirements.

Accuracy would also be improved by refining estimates of the tip-substrate interface temperature, which would elucidate interpretation of experimental results. Estimates of the processing temperature at the tip-substrate interface are heavily influenced by the interfacial contact impedance, R_b . Little experimental data exists for contact impedance between solids above room temperature [11], and there are few reports of experimental measurements of the contact resistance into disordered structures such as polymers at and above room temperature [12-14]. Although experimental data do not currently exist, heated silicon cantilevers could be used as a tool for experimentally measuring contact conductance on various substrates at elevated temperatures [15].

7.2.2.2 New Applications

The advancement and development of applications listed above will require new characterization methods. Biological applications will likely require operating the cantilever in a liquid environment, necessitating characterization of a passivated cantilever as well as measurements of transient cantilever behavior in liquids.

Additionally, estimating the minimum calorimetric sensitivity of the cantilever requires measurement of electronic detection limits of the cantilever resistance.

7.3 Long-Range Implications

Although there is some doubt over the commercial utility of AFM-based technologies, heated silicon cantilevers offer exciting possibilities at the very least as a research tool. The spatial localization capable with the sharp tip enables fundamental investigations of thermal phenomena in all scientific fields, the applications and implications of which will only become fully apparent as use of the cantilevers becomes more common.

7.4 References

- [1] M. E. Anderson, C. Srinivasan, J. N. Hohman, E. M. Carter, M. W. Horn and P. S. Weiss, Combining conventional lithography with molecular self-assembly for chemical patterning, *Advanced Materials*, 18 (2006) 3258.
- [2] B. A. Nelson, W. P. King, A. R. Laracuate, P. E. Sheehan and L. J. Whitman, Direct deposition of continuous metal nanostructures by thermal dip-pen nanolithography, *Applied Physics Letters*, 88 (2006) 033104.
- [3] M. Yang, P. E. Sheehan, W. P. King and L. J. Whitman, Direct writing of a conducting polymer with molecular-level control of physical dimensions and orientation, *Journal of the American Chemical Society*, 128 (2006) 6774-6775.
- [4] J. Haaheim, R. Eby, M. Nelson, J. Fragala, B. Rosner, H. Zhang and G. Athas, Dip Pen Nanolithography (DPN): process and instrument performance with NanoInk's NSCRIPTOR system, *Ultramicroscopy*, 103 (2005) 117-132.
- [5] T. T. Moore and W. J. Koros, Non-ideal effects in organic-inorganic materials for gas separation membranes, *Journal of Molecular Structure*, 739 (2005) 87-98.

- [6] T. Grossetete, L. Gonon and V. Verney, Submicrometric characterization of the heterogeneous photooxidation of polypropylene by microthermal analysis, *Polymer Degradation and Stability*, 78 (2002) 203-210.
- [7] M. Alcoutlabi and G. B. McKenna, Effects of confinement on material behaviour at the nanometre size scale, *Journal of Physics-Condensed Matter*, 17 (2005) R461-R524.
- [8] W. P. King, S. Saxena, B. A. Nelson, R. Pitchimani and B. L. Weeks, Nanoscale Thermal Analysis of an Energetic Material, *Nano Letters*, 6 (2006) 2145-2149.
- [9] T. A. Sulchek, R. W. Friddle, K. Langry, E. Y. Lau, H. Albrecht, T. V. Ratto, S. J. DeNardo, M. E. Colvin and A. Noy, Dynamic force spectroscopy of parallel individual Mucin1-antibody bonds, *Proceedings of the National Academy of Sciences of the United States of America*, 102 (2005) 16638-16643.
- [10] B. Alberts, A. Johnson, J. Lewis, M. Raff, K. Roberts and P. Walter, *Molecular Biology of the Cell*, Garland Science, New York, 2002.
- [11] D. G. Cahill, W. K. Ford, K. E. Goodson, G. D. Mahan, A. Majumdar, H. J. Maris, R. Merlin and S. R. Phillpot, Nanoscale thermal transport, *Journal of Applied Physics*, 93 (2003) 793-818.
- [12] D. S. Matsumoto, C. L. Reynolds and A. C. Anderson, Thermal Boundary Resistance at Metal-Epoxy Interfaces, *Physical Review B*, 16 (1977) 3303-3307.
- [13] T. Beechem, S. Graham, P. Hopkins and P. Norris, Role of Interface Disorder on Thermal Boundary Conductance Using a Virtual Crystal Approach, *Appl. Phys. Lett.*, 90 (2007) 054104.
- [14] E. T. Swartz and R. O. Pohl, Thermal-Boundary Resistance, *Reviews of Modern Physics*, 61 (1989) 605-668.
- [15] L. Shi and A. Majumdar, Thermal transport mechanisms at nanoscale point contacts, *Journal of Heat Transfer-Transactions of the Asme*, 124 (2002) 329-337.

APPENDIX A

PRACTICALITIES OF USING HEATED SILICON ATOMIC FORCE MISROSCOPE CANTILEVERS

Heated silicon cantilevers are expensive, especially in regards to the time invested by the person who fabricated them. The cantilevers are also delicate, sensitive, and easy to destroy. For these reasons, this appendix gives practical advice on safe handling of the cantilevers.

A.1 Starting Out

The most important step for minimizing cantilever breakage is to become comfortable with a pair of tweezers. The tweezers should come to a relatively sharp point to enable surety in gripping the sides of the cantilever chip. Before handling functional cantilevers, practice manipulating broken cantilevers – insert and remove them from cantilever holders, make and test electrical connections, and be sure that you can do these things regularly and repeatedly without dropping the cantilever. You should set aside your own set of tweezers and keep them with you or stowed away in your own drawer to ensure that you never have to compromise and use non-ideal tweezers to manipulate a cantilever.

A.2 Storage

Heated cantilevers should be stored on something very sticky. If using a Gel-Pak, use the special paks with a level '8' stickiness, which can be identified by the number written on the sticker on the lid of the pak. If concerned about the cleanliness of the tip surface, the cantilever should not be stored on a Gel-Pak since the adhesive can outgas. Instead, the cantilever should be stored on double-sided tape after weakening the tape adhesive by touching a latex glove to the tape. Adsorbed contaminants can also be removed by heating the cantilever above ~ 450 °C. The stickiness of the storage surface is a double-edged sword since the cantilever chips can become difficult to remove from sticky substrates even with tweezers, which is part of why becoming proficient with tweezers is important.

I am fairly certain that one of the statements of the second law of thermodynamics is “if you leave anything valuable out in the lab, it will break or disappear.” Thus cantilevers should be stored somewhere that no one except you will be putting things – such as your office or your own drawer or cabinet. That said, you *should* leave a cantilever in an apparatus that you are using, such as an AFM or other test setup, if you have the opportunity to do so and are reasonably confident that the cantilever itself is not in an exposed position. Minimizing the number of times that you have to take a cantilever into or out of a cantilever holder minimizes the opportunities for you to drop or break the cantilever.

A.3 Characterization

The first thing to do after receiving a new cantilever is to characterize it electrically and thermally. This should be done before performing any experiments because another statement of the second law of thermodynamics is “if you perform experiments first and then go to calibrate a device afterwards, the device will break before you finish the characterization and your experimental results will become worthless.”

A.3.1 Electrical Characterization

Electrical characterization should be done first since it allows you to determine the required range of voltages and heating powers to get the cantilever close to its intrinsic temperature, which as a general rule is $\sim 600\text{-}800\text{ }^{\circ}\text{C}$ for current design processes. Before characterizing, measure the room-temperature resistance of the cantilever and then connect the cantilever in series with a current-limiting resistor with a resistance value a factor of $\sim 5\text{x}$ larger than the room-temperature resistance of the cantilever. Then ramp the voltage applied to the circuit, and gradually increase the voltage until you see the intrinsic peak in the cantilever resistance. Ramp the voltage a few more times, and if there is significant variation in the cantilever resistance between the runs, continue ramping the voltage until the resistance stabilizes. You should note the applied current and heating power at the intrinsic resistance, as these will be important for the thermal characterization. Note that the applied voltage has virtually no meaning. The voltage is a means for producing heating, and as such the *heating power* is important and is the

parameter that should be noted in your lab notebook when performing experiments and characterization.

I should also add a note on the use of a resistor in series with the cantilever. The primary purpose of the resistor is to act as a current-limiter to prevent thermal runaway in the cantilever. Since a sourcemeter measures both current and voltage, the resistor is not needed for sensing purposes. I rarely used such a resistor. In reality, the thermal runaway problem only occurs when a constant voltage is applied to the cantilever and the cantilever is above its intrinsic resistance. Below the intrinsic resistance, as the cantilever heats up, the resistance also increases, which reduces the heating power for a constant voltage, which cools the cantilever. The heating is thus self-stabilizing. The heating is destabilizing for a constant voltage above the intrinsic resistance, and this is the source of the thermal runaway effect. The situation reverses when a constant current is applied to the cantilever. Above the intrinsic resistance, as the cantilever heats up the resistance decreases, which decreases the heating power for a constant current, which cools the cantilever. Thus for constant current, heating is destabilizing below the intrinsic resistance, but self-stabilizing above the intrinsic resistance.

In practice, thermal runaway can be prevented by sourcing a constant voltage onto a cantilever while setting a current limit on the sourcemeter. If the current limit is set to a value below the current at the intrinsic point, then the cantilever will not exhibit the runaway effect. The cantilevers can be operated above their intrinsic temperature, and when doing so you should have the sourcemeter source constant current rather than constant voltage to maintain a stable heating power and cantilever temperature. Operation above the intrinsic temperature will cause some changes to the electrical

characteristics of the cantilever, and the changes will get larger as the temperature or the heating time is increased. Since the cantilevers are usually operated below their intrinsic temperature, you should in general source constant voltage while being sure to properly set a current limit to prevent cantilever damage.

A.3.2 Thermal Characterization

At the time of this dissertation, the best method for thermal calibration of the cantilevers comes from measuring the Stokes peak position using Raman spectroscopy. When I calibrate a cantilever, I only calibrate for 5-6 relatively evenly-spaced heating powers below the power at the intrinsic point. Above the intrinsic point, the Raman laser starts to have large effects on the cantilever resistance. Calibration goes much faster if you do NOT use a current-limiting resistor in series and instead protect the cantilever by setting the current limit on the sourcemeter below the intrinsic current, as described above. This enables immediately reading the applied power and cantilever resistance directly off of the sourcemeter, and will give you a much more intuitive sense of how the cantilever temperature is changing.

Here are several more practical notes on Raman thermal calibration:

- 1) Taking repeated temperature measurements at a given heating power gives little to no improvement in the accuracy of the measurement of the Stokes peak position, so one point per temperature should suffice.
- 2) A second-order fit between temperature and power matches the data well.
- 3) The position of the Raman laser along the cantilever heater does not matter very much, but should be relatively close to the tip. Placing the

laser on the tip can yield strange scattering spectra. It is important to make sure that the laser is positioned in the same place during the room temperature baseline measurement as it is during subsequent measurements.

- 4) The drift in the Raman microscope gets much smaller after an hour, but does not go entirely away.
- 5) The Raman laser can affect the power dissipated on the cantilever due to excitation of electrical carriers. As such, the power that you should record during the calibration is the power dissipated on the cantilever while the laser is on and the Raman spectrum is being recorded.
- 6) You should choose the lowest laser power that enables you to record a spectrum with a well-resolved Stokes peak within ~1 minute. On the microscope I used, this corresponded to shuttering the laser to 5%.

A.4 Miscellaneous Notes

- 1) Develop a useful naming system for your cantilevers so you can keep characterizations separate. My naming system consisted of WaferNumber-CantileverShape-Index. For example 'FB1' meant the cantilever came from wafer F, had shape B, and was the first FB cantilever I had used. The wafer number is important because cantilever behavior can vary significantly between wafers, especially if processing conditions change between the wafers. The shape is

important because it is an easy distinguishing characteristic between cantilevers.

- 2) Never rush, especially in clean up. Many times when I broke a cantilever it happened at the end of the experiment when I was rushing to get home, or to class, etc. Take special care to not rush when packing up, especially if it is late at night.
- 3) There is (at this time) a nano volt meter in the lab. Do not use it in conjunction with heated cantilevers. It will sporadically and unpredictably inject current into the cantilever and cause it to burn out. On a more general note, ensure that the electronics you use with the cantilever will not damage it before destroying a dozen cantilevers.
- 4) Test out new substrates and holding apparatus' before using them with a good cantilever. I saved cantilevers that had broken tips or unreliable electrical characteristics and used them as guinea pigs. Some substrates have adhesion that is strong enough to break off a cantilever, and sometimes a new apparatus for holding a cantilever is not well-made or has current leaks somewhere that can result in cantilever burn out or breakage. Better to find these things out with an unusable cantilever than one that is well-characterized and reliable.
- 5) Keep a written record of how your cantilevers are breaking, and take steps to address the actions that most commonly break the cantilevers.
- 6) On the Asylum AFM, you have to be careful to place the cantilever holder into the AFM head levelly. If the pins on the underside of the

holder contact the grounded metal ring that surrounds the tipholder, you will burn out a resistor on the main circuit board of the controller. You can tell when this happens because there will be a stray voltage of $\sim 1.7V$ on the spring clip of the cantilever holder when it is in the AFM.

- 7) Occasionally cantilevers will have residual films of photoresist stuck to them. When this happens, place the cantilever in a furnace at ~ 500 °C for several minutes to burn off the photoresist.
- 8) Veeco Instruments has an SPM user e-mail digest. It is an excellent resource for information and help from AFM experts.

APPENDIX B

A METHOD FOR CALIBRATING THE SPRING CONSTANT OF HEATED SILICON CANTILEVERS AT ELEVATED TEMPERATURES

In AFM operation, measuring and controlling the interaction between the cantilever tip and the underlying substrate is of great importance and requires accurate knowledge of the cantilever spring constant.

B.1 Stress Integral-Averaged Temperature

The most common technique for calibrating the spring constant is the thermal noise method, which exploits the equipartition theorem and relates thermal energy to the elastic potential energy of the cantilever [1]. In this technique, the spring constant is given by

$$k = \frac{k_B T}{\langle x^2 \rangle} \quad (\text{B.1})$$

where k is the cantilever spring constant, k_B is Boltzmann's constant, T is the cantilever temperature, and $\langle x^2 \rangle$ is the mean square deflection of the cantilever. The mean square deflection of the cantilever can be determined by integrating a simple harmonic oscillator fit of the fundamental resonant mode of the power spectrum of the cantilever thermal

vibrations, which Figure B.1 shows for a typical silicon heated cantilever at room temperature.

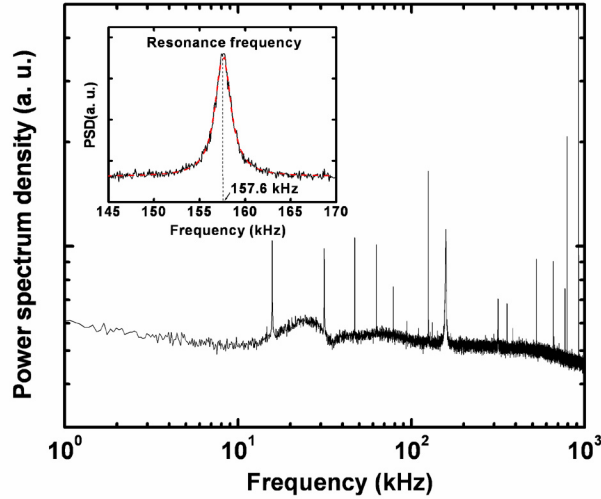


Figure B.1. Thermal noise of the cantilever is measured and Fourier transformed to obtain a power spectrum. The measured resonant frequency was 157.6 kHz at room temperature.

Figure B.2 shows measured values for $\langle x^2 \rangle$ during cantilever heating, which increase with the cantilever temperature due to the increase in the thermal energy and the decrease in the elastic modulus [2]. However, Eq. ((B.1) could not be used to estimate the cantilever spring constant from the measurements of $\langle x^2 \rangle$ because the temperature distribution along the cantilever legs was non-uniform and thus the temperature T could not be defined.

Figure B.3 shows calculations of the cantilever spring constant using various estimates of the thermal energy $k_B T$ in Eq. ((B.1). The spring constant should decrease as the elastic modulus decreases at increasing temperature, and Figure B.3 shows that thermal energy estimates close to ambient were the only estimates that resulted in the expected reduction of the spring constant. Therefore the thermal energy in the cantilever

was much closer to that of ambient thermal energy $k_B T_0$ than the thermal energy calculated using the heater temperature $k_B T_H$.

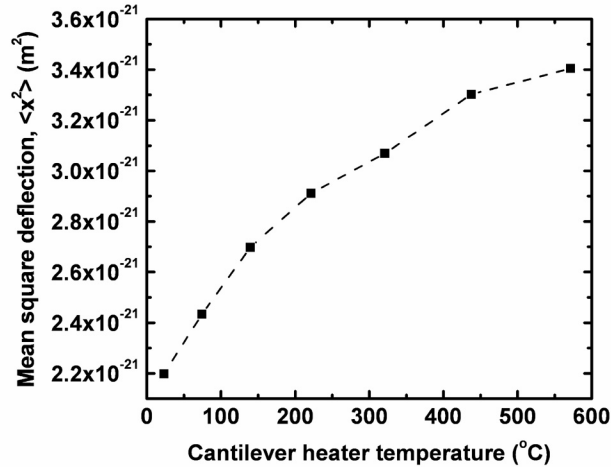


Figure B.2. As the cantilever temperature increases, the average harmonic displacement also increases, in accordance with both increasing thermal energy and decreasing spring constant.

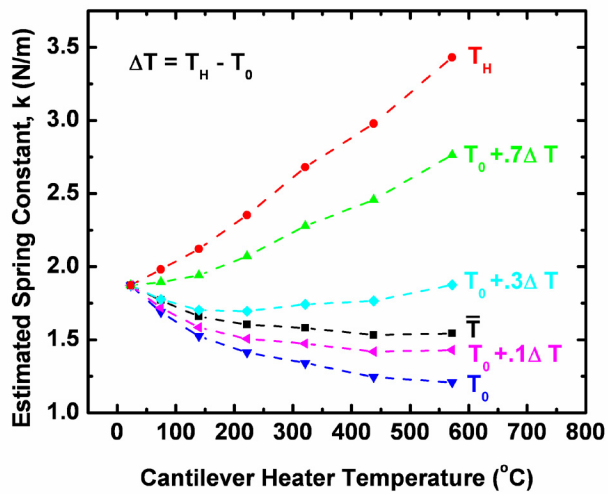


Figure B.3. Spring constant calculated from Eq. ((B.1)) using various estimates for the temperature. The temperatures T_H , T_0 , and \bar{T} correspond to the cantilever heater temperature, the ambient temperature, and the stress integral average temperature defined in Eq. ((B.2)), respectively. The only estimates of the thermal energy of the cantilever that yield the expected reduction in spring constant with increasing temperature are those using a temperature much closer to room temperature than to the heater temperature, including the stress integral average temperature.

This phenomenon can be understood by considering that the mechanical energy in the oscillating cantilever is proportional to the square of the bending stress, and the bending stress was maximal at the base of the cantilever, where the temperature was close to ambient. To improve the estimate for thermal energy, an integral-average temperature based on the bending stress can be defined by

$$\bar{T} = \frac{\int_V T(x)\sigma(x, y)dV}{\int_V \sigma(x, y)dV} = \frac{3}{L^3} \int_0^L T(x)x^2 dx \quad (\text{B.2})$$

where the integration takes place over the volume of the cantilever V , x is measured from the heater end of the cantilever, L is the length of the cantilever, $T(x)$ is the temperature distribution along the legs of the cantilever and was taken from reported data [3], and $\sigma(x, y)$ is the bending stress profile in the cantilever assuming point loading at the end, in accordance with the simple harmonic oscillator behavior assumed in Eq. ((B.1). Figure B.3 shows that when \bar{T} was used for determining the spring constant with Eq. ((B.1), the expected reduction in the cantilever spring constant emerged. Thus, the combination of Eqs. ((B.1)-((B.2) represents a method of estimating the cantilever spring constant during operation at elevated temperature.

B.2 References

- [1] J. L. Hutter and J. Bechhoefer, Calibration of atomic-force microscope tips, *Review of Scientific Instruments*, 64 (1993) 1869-1873.
- [2] U. Gysin, S. Rast, P. Ruff, E. Meyer, D. W. Lee, P. Vettiger and C. Gerber, Temperature dependence of the force sensitivity of silicon cantilevers, *Physical Review B*, 69 (2004)

[3] J. Lee, T. Beechem, T. L. Wright, B. A. Nelson, S. Graham and W. P. King, Electrical, Thermal, and Mechanical Characterization of Silicon Microcantilever-Heaters, *Journal of Microelectromechanical Systems*, 15 (2006) 1644-1655.